Energy Storage and Conversion

https://ojs.acad-pub.com/index.php/esc

2024 VOLUME 2 ISSUE 2
ISSN: 3029-2778 (Online)

2

Editorial Team

Editor-in-Chief

Associate Editor

Editorial Board Members

Muhammad Shahzad Nazir
Huaiyin Institute of Technology
China

Rahim Zahedi
University of Tehran
Iran

Yong Wang
Shanghai University
China

Volume 2 Issue 2 • 2024

Energy Storage and Conversion

ACADEMIC
ACADEMIC PUBLISHING PTE LTD

2024 | Volume 2 | Issue 2

Energy Storage and Conversion

https://ojs.acad-pub.com/index.php/esc

Contents

Articles

Reviews

Energy Storage and Conversion 2024, 2(2), 369.
https://doi.org/10.59400/esc.v2i2.369

Article

Nitrided copper-iron composite oxides derived from layered double hydroxides for enhanced carbon dioxide electroreduction to methane and formic acid

Dian Song[1], Jinqing He[1], Yiping Wang[1,2,*], Xuhui Zhao[1], Fazhi Zhang[1], Xiaodong Lei[1,2,*]

[1] State Key Laboratory of Chemical Resource Engineering, Beijing University of Chemical Technology, Beijing 100029, China
[2] Quzhou Institute for Innovation in Resource Chemical Engineering, Quzhou 324000, Zhejiang Province, China
*** Corresponding authors:** Yiping Wang, wangyiping@buct.edu.cn; Xiaodong Lei, leixd@mail.buct.edu.cn

CITATION

Song D, He J, Wang Y, et al. Nitrided copper-iron composite oxides derived from layered double hydroxides for enhanced carbon dioxide electroreduction to methane and formic acid. Energy Storage and Conversion. 2024; 2(2): 369. https://doi.org/10.59400/esc.v2i2.369

ARTICLE INFO

Received: 27 November 2023
Accepted: 8 January 2024
Available online: 8 May 2024

Abstract: The reduction of carbon dioxide into valuable chemical products is a promising solution to address carbon balance and energy issues. Herein, amorphous nitrided copper-iron oxides are prepared by gas-phase nitriding of CuFe-layered double hydroxide precursors with urea as a nitrogen source. The obtained materials show high activity for CO_2 electroreduction to methane and formic acid, achieving a total Faraday efficiency of 74.7% at −0.7 V vs. RHE and exhibiting continuous 10 h durability in the H-cell. The uniformly distributed Cu+ sites act as active sites by losing electrons to activate CO_2. During the CO_2 electroreduction, CO_2 is converted to *COOH via proton-electron coupling; *COOH combines directly with a proton in solution to produce the HCOOH product; and the other part of *COOH undergoes a protonated dehydration process to form the *CHO intermediate, which dehydrates again to form CH_4. This study provides a new approach for designing CO_2 electroreduction catalysts.

Keywords: CuFe-LDH; nitrided copper-iron oxides; CO_2 electroreduction; electrocatalysis

1. Introduction

Carbon dioxide (CO_2) is a key contributor to the global warming crisis in modern-day society. Excessive emissions of CO_2 have resulted in severe environmental issues, including the greenhouse effect, acidification of water bodies, and climate change. These challenges present a significant threat to the sustainable development of society [1]. The combustion of fossil fuels from anthropogenic sources is the major source of atmospheric CO_2 emissions [2]. The main ways to achieve zero CO_2 emissions are through the decarbonization of raw materials, carbon sequestration and capture, as well as carbon recovery and neutralization [3–5]. The most efficient method for converting CO_2 into valuable chemicals today is electrocatalytic reduction [6,7]. However, the electrocatalytic reduction of CO_2 faces challenges such as the hydrogen evolution reaction (HER) competing with the desired reaction [8]. Additionally, the high thermodynamic stability and kinetic inhibitory effects of CO_2 molecules result in their deactivation [9,10]. Therefore, the top priority in research in electrocatalytic reduction of carbon dioxide is to design catalysts with low overpotential that can suppress the HER and effectively promote the reduction of carbon dioxide. These catalysts should also possess advantages such as low cost, high selectivity, stability, and durability.

Due to limited reserves and high costs of precious metals, transition metals with significant stability and high economic feasibility in alkaline media have attracted considerable attention in the field of electrocatalysis [11]. Therefore, it is necessary to

search for transition metal catalysts with higher catalytic activity [12–14]. Iron-based materials are considered to be very promising catalysts due to their low cost and environmental friendliness [15]. However, iron-based materials continue to face a significant challenge in terms of low conductivity [16], limiting their electrocatalytic performance. The reduction intermediate CO in the carbon dioxide is harmful to iron-based materials because CO can damage the active sites of iron-based catalysts., further limiting their effectiveness in electrocatalysis [17]. Scientists are now extensively overcoming this limitation by coupling iron-based materials with other materials such as metal oxides or organic carbon frameworks [18,19]. Copper-based catalysts have garnered significant research attention due to their high efficiency in converting carbon dioxide into hydrocarbons [20,21]. In recent years, considerable research has been conducted with the aim of designing efficient Cu-based heterogeneous materials as Carbon Dioxide Reduction Reaction (CO_2RR) electrocatalysts. These materials include monometallic Cu, Cu-based oxides, Cu-based bimetallic systems, single/dual Cu atoms, and Cu-based metal-organic frameworks (MOFs) [22]. To improve the CO_2 reduction activity of catalysts, structural adaptations such as modification of active sites, morphology, or size [23,24], introducing other elements [25,26], as well as surface modification and electroplating [27–29] are being investigated. Among these methods, nitrides of transition metals exhibit exceptional electronic [30–32], mechanical and optical properties, making them very suitable for reducing CO_2 to C_1 products [32–35]. Nitrides of transition metals are usually solid compounds with strong metal-nitrogen bonds [36], which gives them a high degree of structural stability. Compared to other catalysts, transition metal nitrides cause less corrosion or structural changes during electrochemical processes. Therefore, it can participate in the reaction stably for a long time [37]. Despite their high electrochemical activity, the limited number of electrochemically active sites in the nitrides of transition metals may affect their catalytic efficiency in practical reactions [38]. Amorphous materials are rich in active defect sites, thus favoring efficient CO_2 electroreduction. Shan et al. synthesized Cu@CuEu nanoparticles with amorphous CuEu alloy shells. Defect sites in the amorphous material, which may interact effectively with CO_2 molecules or their reduction intermediates, optimize the reaction pathway for CO_2 reduction [39]. Yang et al. prepared Bi-based catalysts with amorphous layers. The disordered arrangement of atoms in the amorphous materials provides more CO_2 adsorption sites and may reduce the activation energy of CO_2 molecules by changing the electronic structure of the catalysts. This facilitates the subsequent reduction steps [40].

The structural units of Layered Double Hydroxides (LDHs) primarily exhibit an octahedral geometry, where hydroxyl ions are situated at the vertices of the octahedron and the encapsulated metal ions are positioned at the center. LDHs have a general chemical formula of $[M^{2+}{}_{1-x}M^{3+}{}_x(OH)_2]^{x+}(A^{n-})_{x/n}\cdot yH_2O$, in which M^{2+}, M^{3+}, and A respectively represent divalent cations (e.g., Ni^{2+}, Mg^{2+}, Cu^{2+}, Ca^{2+}), trivalent cations (e.g., Fe^{3+}, Al^{3+}), and anions [41]. By selecting different metals and anionic species, various types of LDHs can be synthesized. The high degree of design flexibility gives LDHs extensive potential applications in various catalytic reactions, such as photocatalysis, thermocatalysis, and electrocatalysis, including CO_2RR [42–44]. Ma et al. have demonstrated that Cd-MgAl-LDHs exhibit exceptional activity in the

electrochemical reduction of CO_2 to CO [45]. Zhang et al. found that $Cu_9Zn_1/Cu_{0.8}Zn_{0.2}Al_2O_4$ generated from CuZnAl-LDH enhanced the adsorption of CO intermediates and promoted C-C coupling, greatly improving the activity of CO_2RR [46].

Our group has previously demonstrated that CuFe-LDH could serve as an outstanding precursor for electrochemical catalysts due to its unique properties [47]. In this study, we successfully synthesized amorphous nitrided copper-iron oxides through the gas-phase nitridation of CuFe-LDH, exploiting the distinctive and highly dispersed metal components present in LDH. To understand the correlation between the material structure and the performance of CO_2RR, the chemical composition and the existence state of surface elements are analyzed, and the formed gas and liquid products of CO_2RR are detected. The reaction mechanism was studied through X-ray photoelectron spectroscopy (XPS), X-ray diffraction (XRD), and in situ attenuated total reflection fourier transform infrared spectroscopy (ATR-FTIR). The dispersion of copper in nanoparticles results in a highly uniform distribution, thereby enhancing its activity in the electroreduction of CO_2.

2. Experimental

2.1. Chemicals and materials

The chemical reagents used in this work include $Cu(NO_3)_2 \cdot 3H_2O$ (≥99.0%, Macklin), $Fe(NO_3)_3 \cdot 9H_2O$ (≥98.5%, Macklin), NaOH (≥96.0%, Tianjin Fuchen Chemical Reagents), $KHCO_3$ (≥99.0%, Aladdin), Na_2CO_3 (≥99.0%, Beijing Chemical Plant), and $CO(NH_2)_2$ (≥99.0%, Macklin). Deionized water was utilized in the experiment. Ar (≥99.999%), CO_2 (≥99.999%), and N_2 (≥99.999%) were purchased from Beijing Shunanqite Gas. All of the chemicals in this study were used without any additional purification.

2.2. Fabrication of nitrided copper-iron composite oxides

The CuFe-LDH precursor was prepared using the co-precipitation process. 0.0075 mol of $Cu(NO_3)_2 \cdot 3H_2O$ and 0.0025 mol of $Fe(NO_3)_3 \cdot 9H_2O$ were dissolved in 60 mL of deionized water. 0.02 mol of NaOH and 0.005 mol of Na_2CO_3 were dissolved in 60 mL of deionized water. The two solutions were added dropwise into a three-necked flask under continuous magnetic stirring, maintaining the pH of the mixed solution at 5 in the above process. After addition, the mixed solution was stirred for one hour and transferred into a hydrothermal reactor for a 5 h reaction at 110 ℃. After the completion of hydrothermal treatment, the obtained CuFe-LDH samples were collected through centrifugation, filtration, and drying.

The nitrided copper-iron composite oxides were prepared by the gas-phase nitridation of CuFe-LDH precursors with urea as a nitrogen source. 0.5 g CuFe-LDH sample and 5 g urea were transferred to a tube furnace, and then the nitridation reaction was conducted at 300 ℃ for 2 h with a heating rate of 1 ℃·min^{-1} in N_2. After the nitridation, the obtained sample was washed with ethanol, centrifuged, and vacuum dried.

2.3. Characterization

XRD patterns were acquired by a Bruker D8A25 instrument with Cu Kα radiation and a scanning step of $10°\cdot min^{-1}$. Scanning electron microscope (SEM) images were captured on a Zeiss SUPRA 55 instrument operated at 10 kV. High-resolution transmission electron microscopy (HRTEM) images were taken using a JEOL JEM-F200 instrument equipped with an energy dispersive X-ray spectrometer (EDS), and the test was conducted at an accelerating voltage of 200 kV. XPS and Cu LMM Auger spectra were acquired through a Thermo VG ESCALAB 250 X-ray photoelectron spectrometer with Al Kα X-rays at approximately 2×10^{-9} Pa. ATR-FTIR was conducted in situ using a Tensor II (Bruker) FTIR spectrometer with an MCT detector. The measurements were performed with a VeeMAX III variable-angle specular reflection accessory (Pike, USA) and a spectroelectrochemical cell, combined with a CHI660E instrument to control the reduction potential. Gas chromatography (GC, Shimadzu, GC2014) at 20 ℃ was utilized to quantify the gaseous product. The concentration of Cu and Fe in the material was determined using inductively coupled plasma mass spectrometry (ICP-MS, iCAP6300 Radial, Thermo, US).

2.4. Electrochemical study of CO2 reduction and product analysis

Electrochemical measurements were performed using a CHI660E electrochemical workstation (Shanghai Chenhua Instruments Co., China) in a three-electrode system within an H-cell. The cathode and anode were separated by a Nafion 115 membrane, which acted as a proton exchange membrane. A 0.5 M $KHCO_3$ electrolyte was utilized for the measurements. The working, counter, and reference electrodes are nitrided copper-iron composite oxide powder, graphite rod, and Ag/AgCl (3 $mol\cdot L^{-1}$ KCl), respectively. The given potential was converted to a reversible hydrogen electrode (RHE) using the Nernst equation. The electrolyte that contained 0.5 M $KHCO_3$ saturated with CO_2 exhibited a pH of 7.12.

During the linear sweep voltammetry (LSV) tests, CO_2 (≥99.999%) or Ar (≥99.999%) with high purity were continuously injected into the H-cell. The electrolyte was saturated with CO_2 at a mass flow rate of 30 $mL\cdot min^{-1}$ for over 20 min, following which the cell was hermetically sealed before executing the measurements. After each measurement that lasted for 1.5 h at various overpotentials, the formed products were analyzed.

3. Results and discussion

3.1. Structure of as-prepared catalysts

The XRD patterns of CuFe-LDH and nitrided copper-iron composite oxides are shown in **Figure 1a**. The spectrum of the CuFe-LDH precursor can observe diffraction peaks at 12.8°, 25.8°, 33.1°, 36.6°, 43.6°, 60.9°, and 62.5°, which are respectively attributed to the (003), (006), (009), (015), (018), (110), and (113) crystal faces of the LDH phase [48]. This indicates the successful synthesis of the hydrotalcite precursor. The XRD pattern of nitrided copper-iron composite oxides shows that there are no additional XRD signal peaks except for the C signal peak at 18° indexed to the standard C (JCPDS No. 48-1449), confirming the amorphous nature of the obtained

material. Amorphous materials are more likely to produce defective vacancies during the reaction process, which can serve as active sites for catalytic reactions [49]. Furthermore, a detailed investigation of this composite was conducted by analyzing XPS spectra. (**Figures 1b** and **1c**). It is visible in the spectrum that peaks of Cu 2p at 932.37 and 952.38 eV correspond to zero-valent Cu (Cu^0); in addition to that, Cu 2p at 932.37 and 953.38 eV peaks correspond to Cu $2p_{3/2}$ and $2p_{1/2}$ (**Figure 1a**), but it cannot confirm that Cu^+ or Cu^0 coexist. They were analyzed in conjunction with the LMM spectrum of Cu (**Figure 1b**). The apparent appearance of a signal for Cu^+ [50]. So the presence of Cu^+ was established. Two peaks of Fe 2p at 709.20 and 714.6 eV are within the scope of the Fe $2p_{3/2}$ binding energy, corresponding to Fe^{2+} and Fe^{3+}, respectively (**Figure A1**), further confirming the existence of Fe^{2+} and Fe^{3+} in the composite. The overlapping of the $2P_{1/2}$ and $2P_{3/2}$ peaks of Fe could be due to the interference of the LMM spectrum of Cu. This suggests that charge rearrangement may have occurred within the material after nitriding, which may have led to increased conductivity of the material and enhanced electrochemical activity.

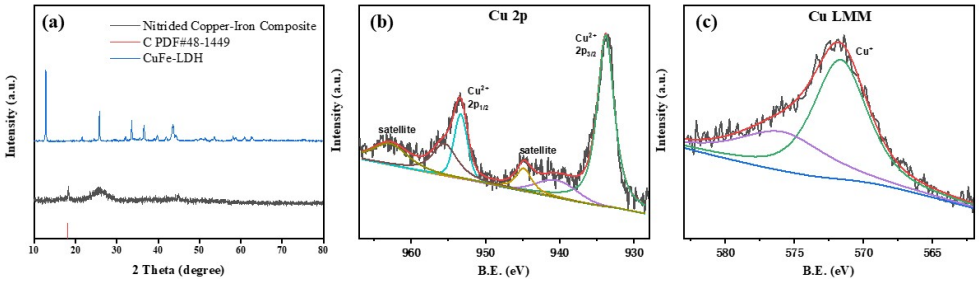

Figure 1. (a) XRD analyses of CuFe-LDH and nitrided copper-iron composite oxides; **(b)** XPS spectra of Cu 2p; **(c)** Cu LMM.

SEM images of CuFe-LDH (**Figure A2**) show that CuFe-LDH has a nanosheet morphology with a smooth surface and approximately 100 nm of thickness. After the nitriding reaction, the catalyst was transformed into nanoparticles with diameters ranging from 50 to 100 nm (as shown in **Figures 2a** and **2b**). The HRTEM image (**Figure 2h**) shows no lattice fringing detected, which was considered a typical characteristic of an amorphous state [51]. This further supports the amorphous nature of nitrided copper-iron composite oxides. In addition, EDS elemental mapping (**Figures 2c–2g**) confirms the homogeneous distribution of Cu, Fe, O, and N atoms on the surface of the catalyst. The EDS results indicate that the elemental contents of Cu, Fe, N, and O are 47.6%, 14.59%, 17.44%, and 20.37%, respectively (**Figure A3**).

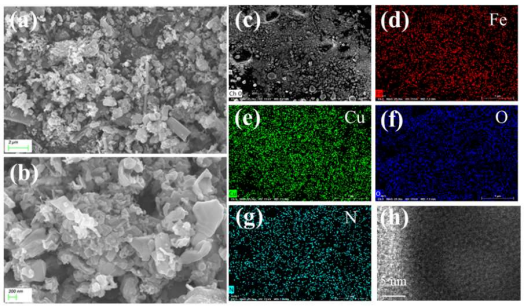

Figure 2. (a–b) SEM images of nitrided copper-iron composite oxides; **(c–g)** EDS mapping results; **(h)** HRTEM.

3.2. CO_2RR performance of as-prepared catalysts

The CO_2 electroreduction performance of nitrided copper-iron composite oxide was investigated in an H-type cell containing 0.5 M $KHCO_3$. **Figures 3a** and **3b** show the stable LSV curves of nitrided copper-iron composite oxide and CuFe-LDH in Ar-saturated (dashed line) and CO_2-saturated (solid line) electrolytes, respectively. The current density of the catalyst is significantly lower than that of the precursor at the same overpotential. As shown in **Figures 3a** and **3b**, the current density remained stable with the increase in overpotential, suggesting that the catalyst did not fall off throughout the reaction process. Moreover, there was no significant fluctuation in the current density during the test (**Figure 3c**), indicating the high stability of the catalyst. In the CO_2 atmosphere, the catalyst exhibits a lower initial potential (−0.1 V vs. RHE). Under Ar-saturated and CO_2-saturated environments, the maximum difference in total current density is 14 mA·cm^{-2} at −0.7 V vs. RHE.

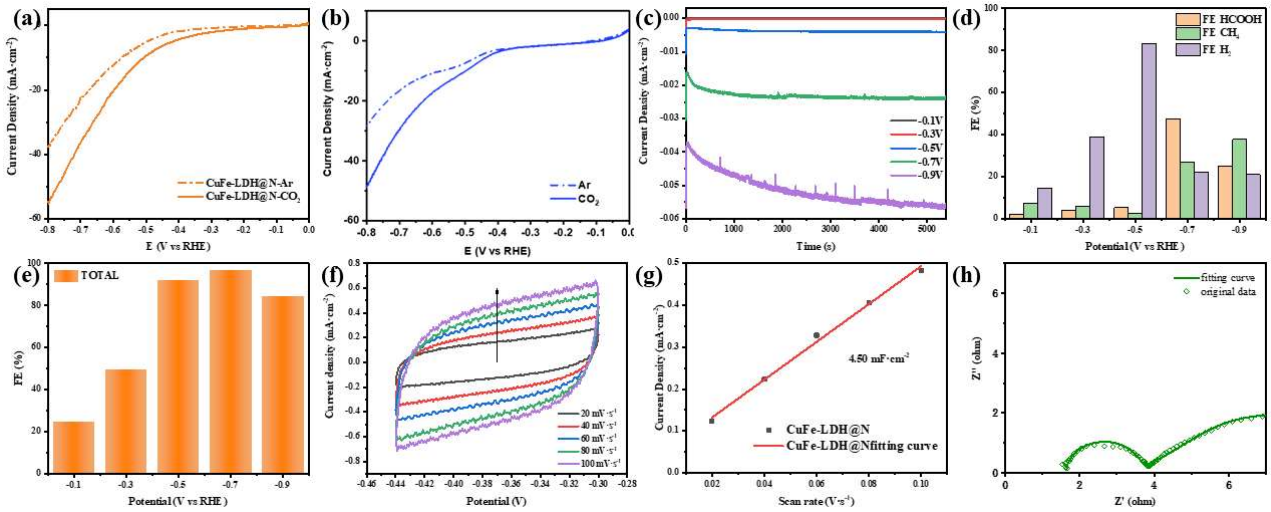

Figure 3. (a) LSV of nitrided copper-iron composite; **(b)** LSV of CuFe-LDH; **(c)** Chronoamperometry test cyclic tests; **(d–e)** the products FE of nitrided copper-iron composite at different test potentials; **(f)** Cyclic voltammograms; **(g)** Linear fit of double layer capacitance current density to scan rate from CV plot; **(g)** The Nyquist plots.

The main product of electrocatalytic CO_2RR over the catalyst is the C_1 product, which includes HCOOH and CH_4. The faradaic efficiency (FE) of HCOOH and CH_4 is 47.55% and 27.13%, respectively, with a maximum FE of 96.77 % at −0.7 V vs. RHE (**Figures 3d** and **3e**). In particular, at −0.7 V, the partial current densities of HCOOH and CH_4 are 17.29 mA cm^{-2} and 9.8 mA cm^{-2}, respectively. However, only a tiny amount of HCOOH is produced due to CO_2 reduction by CuFe-LDH precursor (**Figure A4**). Compared with the literature, it becomes evident that the FE of C_1 products achieved by the catalyst in this study exceeds that of numerous copper-based catalysts (**Table 1**). During the electroreduction of CO_2, the cationic reduction produced by the catalyst consumes part of the charge, resulting in a total FE of the obtained product of less than 100%. To confirm the electrochemical stability of nitrided copper-iron composite oxide, cycling tests were carried out for 10 h at the optimum potential of −0.7 V (**Figure A5**). The results show that the FE of CH_4 decreased slightly, indicating that this catalyst has good electrochemical stability. As revealed in **Figure A6**, the XPS spectra of the catalyst after cycling tests show no

obvious change in the valence state or proportion of surface elements, further confirming the excellent stability of the material.

In addition, the high surface area and fast electron transport kinetics of nitrided copper-iron composite oxide were confirmed by electrochemical active area (ECSA) and electrochemical impedance spectroscopy (EIS). As shown in **Figures 3f** and **3g**, the ECSA value of nitrided copper-iron composite oxide (C_{dl} = 4.50 mF·cm^{-1}) is 3 times that of CuFe-LDH (C_{dl} = 1.53 mF·cm^{-1}) (**Figure A7**). The Nyquist diagram in **Figure 3h** shows that the semicircle diameter (charge transfer resistance, 1.8 Ω) of nitrided copper-iron composite oxide at operating voltage is also smaller than that of CuFe-LDH (2.6 Ω). The above results indicate that the kinetic performance of the obtained catalyst through nitridation surpasses that of its precursor.

Table 1. Comparison of the electrocatalytic activity of catalyst in this work with other catalysts for electrochemical reduction of CO_2.

Catalysts	Concentration of electrolyte	Main products	Potential at FE_{max} (V vs. RHE)	Selectivity FE (%)	*J* (mA·cm^{-2})	References
Cu_3PdxN	0.5M $KHCO_3$	CH_4	−1.25	49.7	8.6	[52]
CuO–P NW	0.1 M KCl	CH_4	−1.1	34	3.5	[53]
Cu-PTI	0.5M $KHCO_3$	CH_4	−0.84	68	236.0	[54]
Cu/Au	0.1M $NaHCO_3$	CH_4	−0.7	16	-	[55]
Cu (II)	1 M KOH	CH_4	−1.0	42	100.0	[56]
ESGDE	0.5M $KHCO_3$	HCOOH	−1.16	73	34.0	[57]
Cu foam	0.1 M $KHCO_3$	HCOOH	−1.3	48	1.0	[58]
Nitrided copper-iron composite	0.5M $KHCO_3$	HCOOH; CH_4	−0.7	47.5; 27.1	17.2; 9.8	This work

3.3. Mechanisms of CH_4 and HCOOH formation

The catalysts underwent chronoamperometric tests at different potentials for 1000 s with the intention of investigating the reaction mechanism and active sites of the catalyst. The SEM images of nitrided copper-iron composite oxide after CO_2 reduction test at −0.10, −0.30, −0.50, −0.70, and −0.90 V are shown in **Figure A8**. The structure of the nitrided catalyst has shown a transition from particles to agglomerates during CO_2 electroreduction.

The existence state of surface elements of the catalyst after chronoamperometric tests at potentials of −0.10, −0.30, −0.50, −0.70, and −0.90 V was analyzed by XPS. (**Figures 4a** and **4b**). The Cu atoms in the catalyst were shown to be mainly Cu^+ and Cu^{2+} during the reaction. In the Cu 2p XPS spectra, peaks at 935.19 eV and 955.01 eV are attributed to Cu^{2+}, and peaks at 932.37 eV and 953.38 eV are attributed to Cu^0 or Cu^+ (**Figure 4a**). The precise state of Cu was further identified by AES (**Figure 4b**); there is a peak assigned to Cu^+ in the Cu LMM spectrum of nitrided copper-iron composite oxide, but no peak attributed to Cu^+ appeared [59,60]. The Cu^+/Cu^{2+} ratio decreases and then increases with increasing potential as the potential increases from −0.1 V vs. RHE to −0.9 V vs. RHE (**Table S1**). This is the same trend as the total FE. This result indicates that Cu^+ is converted to Cu^{2+} during the reaction process. Therefore, it is believed that the reaction process involves the loss of electrons from

Cu^+ as the active site to activate CO_2. Different from Cu, the existence state of Fe remained relatively unchanged, as indicated by the lack of significant differences in the integrated XPS area when compared to the unreacted state (**Figure A9**). The overlapping of the $2P_{1/2}$ and $2P_{3/2}$ peaks of Fe could be due to the interference of the LMM spectrum of Cu. This provides further evidence for the excellent stability of the catalyst.

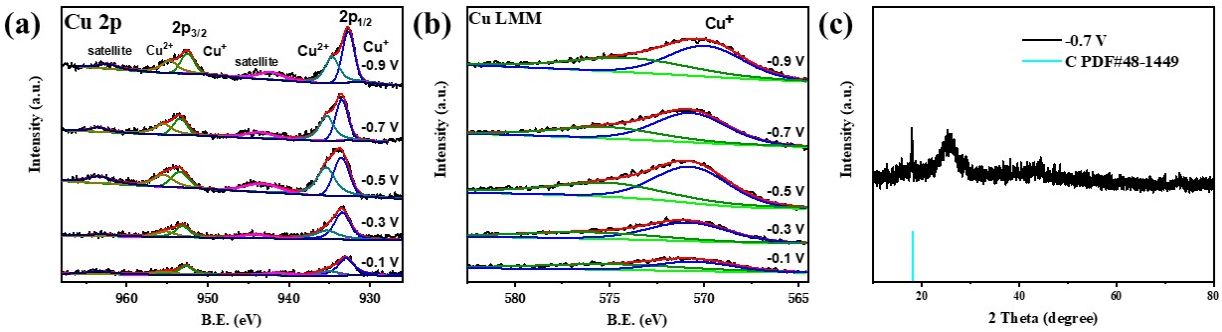

Figure 4. (a) XPS spectra of Cu 2p; **(b)** Cu LMM; **(c)** XRD of material and substrate after the reaction.

To investigate the reaction mechanism in detail, in situ ATR-FTIR was used to detect the intermediate formation during CO_2 electroreduction (**Figure 5**). The peak at about 2400 cm^{-1} belongs to the stretching vibration of Stretching Vibration of CO_2. The peak of the stretching vibration of *COOH appears in the resonant band at around 1490 cm^{-1}. (* represents the adsorption state). The vibrational peaks of desorbed *CO, bridged *CO, and linearly adsorbed *CO should appear at the resonance band of about 2100–2000 cm^{-1}. However, no corresponding signal was detected, possibly due to the high reactivity of *CO during the reaction process. The *CO readily reacts with protons to form *CHO for the following reaction, as indicated by the signals of the *CHO vibrational stretching peaks at 1046 cm^{-1}.

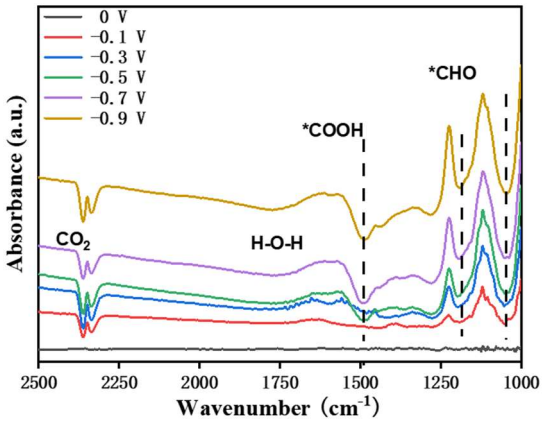

Figure 5. In-situ ATR-FTIR of CO_2 reduction on nitrided copper-iron composite oxides during CO_2 reduction LSV tests with different potentials.

Based on the above analysis, the CO_2 reduction path was proposed as follows (**Figure 6**). During the CO_2 reduction process, amorphous nitrided copper-iron composite oxides adsorb CO_2 first, and then CO_2 is converted into *COOH through proton-electron coupling. The conversion of *COOH has two pathways: Part of *COOH directly combines with protons in the solution, forming the HCOOH product.

The other part of *COOH undergoes the process of proton dehydration addition, forming the *CO intermediate. The unclear *CO signal suggests that it rapidly proceeds to the subsequent reaction step, combining protons in solution to form *CHO. *CHO then combines with protons and undergoes dehydration to form CH_4, which is more challenging to carry out compared to the first step, resulting in a lower FE of CH_4 than HCOOH at different potentials. The e^- during the reaction is supplied by the active site Cu^+.

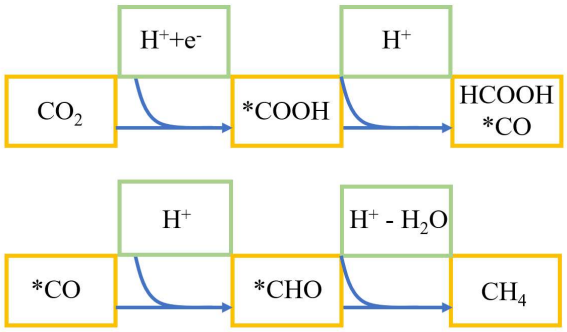

Figure 6. Mechanism of nitrided copper-iron composite oxides electro-catalyze CO_2RR reaction.

4. Conclusion and outlook

The nitrided copper-iron composite nanocomposites were synthesized by urea nitridation of CuFe-LDH precursors at high temperatures. The obtained catalyst has a low production cost and exhibits good electrocatalytic CO_2RR performance. The nitrided copper-iron composite FE was 47.55 % for HCOOH and 27.13 % for CH_4 at −0.7 V, achieving a total FE of 96.77 %. The performance of the catalyst remained stable after 10 h of continuous testing, with the FE of CH_4 product remaining stable above 27% at −0.7 V and the structure also remaining stable. In situ ATR-FTIR studies show that the existence of Cu^+ sites can furnish electrons to *CHO. This study demonstrates the potential of amorphous copper iron oxide nitride as a catalyst for CO_2 electroreduction and provides new ideas for the design of efficient catalysts. But amorphous materials face several major challenges as catalysts in the CO_2RR. Firstly, amorphous materials may have multiple active sites, which may lead to competition for multiple reaction pathways and products, thus reducing the selectivity of the target product. Secondly, amorphous materials are often more complex to prepare than crystalline materials, and their characterization methods are more limited. This may limit an in-depth understanding of the structure and properties of the materials. Amorphous oxide electrocatalysts should be studied more thoroughly using more advanced characterization tools to understand their microstructures (e.g., defects), active sites, and electrocatalytic processes, which will help to design amorphous oxides with desirable electrocatalytic properties.

5. Supporting information

Additional tables and figures for characterization of the synthesized materials' morphology and composition include SEM images of CuFe-LDH, the EDS spectrum of nitrided copper-iron composite nanocomposites, CO_2 electroreduction activity of

CuFe-LDH, stability test results, SEM images of nitrided copper-iron composite oxide after the chronoamperometric i-t tests at different potentials, Nyquist plots of CuFe-LDH and nitrided copper-iron composite oxide, XPS spectra of Fe 2p of nitrided copper-iron composite, and ratios of Cu^{+}, Cu^{2+}, and Cu^{+}/Cu^{2+} calculated by Cu 2p spectra of nitrided copper-iron composite oxide.

Author contributions: Conceptualization, XL; methodology, DS and JH; software, validation, XZ, XL, FZ and YW; formal analysis, DS; investigation, JH; resources, XL; data curation, DS; writing—original draft preparation, DS; writing—review and editing, XL and YW; visualization, supervision, XL and YW; project administration, funding acquisition, XL. All authors have read and agreed to the published version of the manuscript.

Funding: This research was funded by the National Natural Science Foundation of China (Nos.22278020), the Fundamental Research Funds for the Central Universities (Nos. 12060093063 and XK1803-05), and the Program for Changjiang Scholars and Innovative Research Teams in University (No. IRT1205).

Conflict of interest: The authors declare no conflict of interest.

References

1. Birdja YY, Pérez-Gallent E, Figueiredo MC, et al. Advances and challenges in understanding the electrocatalytic conversion of carbon dioxide to fuels. Nature Energy. 2019, 4(9): 732-745. doi: 10.1038/s41560-019-0450-y
2. Zhang Y, Guo SX, Zhang X, et al. Mechanistic understanding of the electrocatalytic CO_2 reduction reaction – New developments based on advanced instrumental techniques. Nano Today. 2020, 31: 100835. doi: 10.1016/j.nantod.2019.100835
3. Chernyak SA, Ivanov AS, Maksimov SV, et al. Fischer-Tropsch synthesis over carbon-encapsulated cobalt and iron nanoparticles embedded in 3D-framework of carbon nanotubes. Journal of Catalysis. 2020, 389: 270-284. doi: 10.1016/j.jcat.2020.06.011
4. Gong W, Ye RP, Ding J, et al. Effect of copper on highly effective Fe-Mn based catalysts during production of light olefins via Fischer-Tropsch process with low CO_2 emission. Applied Catalysis B: Environmental. 2020, 278: 119302. doi: 10.1016/j.apcatb.2020.119302
5. Nitopi S, Bertheussen E, Scott SB, et al. Progress and Perspectives of Electrochemical CO_2 Reduction on Copper in Aqueous Electrolyte. Chemical Reviews. 2019, 119(12): 7610-7672. doi: 10.1021/acs.chemrev.8b00705
6. Ding P, Zhao H, Li T, et al. Metal-based electrocatalytic conversion of CO_2 to formic acid/formate. Journal of Materials Chemistry A. 2020, 8(42), 21947-21960. doi: 10.1039/D0TA08393C.
7. Xu C, Dong Y, Zhao H, et al. CO_2 Conversion Toward Real-World Applications: Electrocatalysis versus CO_2 Batteries. Advanced Functional Materials. 2023, 33(32). doi: 10.1002/adfm.202300926
8. Plankensteiner N, Rondou N, Blom MJW, et al. Competitive enhancement of CO_2 reduction reactions versus hydrogen evolution for high surface area electrodes: A comparative study for Cu and Ag nanomesh. Electrochimica Acta. 2024, 474: 143495. doi: 10.1016/j.electacta.2023.143495
9. Pourebrahimi S, Pirooz M, Ahmadi S, et al. Nanoengineering of metal-based electrocatalysts for carbon dioxide (CO_2) reduction: A critical review. Materials Today Physics. 2023, 38: 101250. doi: 10.1016/j.mtphys.2023.101250
10. Nielsen DU, Hu XM, Daasbjerg K, et al. Chemically and electrochemically catalysed conversion of CO_2 to CO with follow-up utilization to value-added chemicals. Nature Catalysis. 2018, 1(4): 244-254. doi: 10.1038/s41929-018-0051-3
11. Xu F, Wu D, Wang Z, et al. Synergistic effect and high performance of transition metal-anchored boron-doped graphyne electrocatalyst applied in the electroreduction of CO_2 to C_1 products: A DFT study. Applied Surface Science. 2023, 631: 157505. doi: 10.1016/j.apsusc.2023.157505
12. Peterson AA, Abild-Pedersen F, Studt F, et al. How copper catalyzes the electroreduction of carbon dioxide into

hydrocarbon fuels. Energy & Environmental Science. 2010, 3(9): 1311. doi: 10.1039/c0ee00071j
13. Oloman C, Li H. Electrochemical Processing of Carbon Dioxide. ChemSusChem. 2008, 1(5): 385-391. doi: 10.1002/cssc.200800015
14. Hori Y. Electrochemical CO_2 Reduction on Metal Electrodes. In: Vayenas CG, White RE, Gamboa-Aldeco ME (editors). Modern Aspects of Electrochemistry. Springer; 2008. pp. 89-189.
15. Wei L, Meng D, Jiang Q, et al. A review on oxygen evolution electrocatalysts based on the different Ni-Fe matrix composites. Journal of Environmental Chemical Engineering. 2022, 10(6): 108591. doi: 10.1016/j.jece.2022.108591
16. Pan F, Li B, Sarnello E, et al. Pore-Edge Tailoring of Single-Atom Iron–Nitrogen Sites on Graphene for Enhanced CO_2 Reduction. ACS Catalysis. 2020, 10(19): 10803-10811. doi: 10.1021/acscatal.0c02499
17. Su J, Pan D, Dong Y, et al. Ultrafine Fe_2C Iron Carbide Nanoclusters Trapped in Topological Carbon Defects for Efficient Electroreduction of Carbon Dioxide. Advanced Energy Materials. 2023, 13(20). doi: 10.1002/aenm.202204391
18. He J, Hu B, Zhao Y. Superaerophobic Electrode with Metal@Metal-Oxide Powder Catalyst for Oxygen Evolution Reaction. Advanced Functional Materials. 2016, 26(33): 5998-6004. doi: 10.1002/adfm.201602116
19. Wei X, Wei S, Cao S, et al. Cu acting as Fe activity promoter in dual-atom Cu/Fe-NC catalyst in CO_2RR to C_1 products. Applied Surface Science. 2021, 564: 150423. doi: 10.1016/j.apsusc.2021.150423
20. Bagger A, Ju W, Varela AS, et al. Electrochemical CO_2 Reduction: Classifying Cu Facets. ACS Catalysis. 2019, 9(9): 7894-7899. doi: 10.1021/acscatal.9b01899
21. Cometto C, Ugolotti A, Grazietti E, et al. Copper single-atoms embedded in 2D graphitic carbon nitride for the CO_2 reduction. npj 2D Materials and Applications. 2021, 5(1). doi: 10.1038/s41699-021-00243-y
22. Kong Q, An X, Liu Q, et al. Copper-based catalysts for the electrochemical reduction of carbon dioxide: progress and future prospects. Materials Horizons. 2023, 10(3): 698-721. doi: 10.1039/d2mh01218a
23. Yu P, Lv X, Wang Q, et al. Promoting Electrocatalytic CO_2 Reduction to CH_4 by Copper Porphyrin with Donor–Acceptor Structures. Small. 2022, 19(4). doi: 10.1002/smll.202205730
24. Yang YL, Wang YR, Gao GK, et al. Self-assembly of single metal sites embedded covalent organic frameworks into multi-dimensional nanostructures for efficient CO_2 electroreduction. Chinese Chemical Letters. 2022, 33(3): 1439-1444. doi: 10.1016/j.cclet.2021.08.063
25. Liu B, Peng H, Cheng J, et al. Nitrogen-Doped Graphene-Encapsulated Nickel–Copper Alloy Nanoflower for Highly Efficient Electrochemical Hydrogen Evolution Reaction. Small. 2019, 15(48). doi: 10.1002/smll.201901545
26. Portha JF, Parkhomenko K, Kobl K, et al. Kinetics of Methanol Synthesis from Carbon Dioxide Hydrogenation over Copper–Zinc Oxide Catalysts. Industrial & Engineering Chemistry Research. 2017, 56(45): 13133-13145. doi: 10.1021/acs.iecr.7b01323
27. Ma Y, Wang J, Yu J, et al. Surface modification of metal materials for high-performance electrocatalytic carbon dioxide reduction. Matter. 2021, 4(3): 888-926. doi: 10.1016/j.matt.2021.01.007
28. Bui TS, Lovell EC, Daiyan R, et al. Defective Metal Oxides: Lessons from CO_2RR and Applications in NO_XRR. Advanced Materials. 2023, 35(28). doi: 10.1002/adma.202205814
29. De Luna P, Quintero-Bermudez R, Dinh CT, et al. Catalyst electro-redeposition controls morphology and oxidation state for selective carbon dioxide reduction. Nature Catalysis. 2018, 1(2): 103-110. doi: 10.1038/s41929-017-0018-9
30. Anasori B, Lukatskaya MR, Gogotsi Y. 2D metal carbides and nitrides (MXenes) for energy storage. Nature Reviews Materials. 2017, 2(2). doi: 10.1038/natrevmats.2016.98
31. Han M, Maleski K, Shuck CE, et al. Tailoring Electronic and Optical Properties of MXenes through Forming Solid Solutions. Journal of the American Chemical Society. 2020, 142(45): 19110-19118. doi: 10.1021/jacs.0c07395
32. Xiao Y, Zhang W. High throughput screening of M_3C_2 MXenes for efficient CO_2 reduction conversion into hydrocarbon fuels. Nanoscale. 2020, 12(14): 7660-7673. doi: 10.1039/c9nr10598k
33. Li N, Chen X, Ong WJ, et al. Understanding of Electrochemical Mechanisms for CO_2 Capture and Conversion into Hydrocarbon Fuels in Transition-Metal Carbides (MXenes). ACS Nano. 2017, 11(11): 10825-10833. doi: 10.1021/acsnano.7b03738
34. Otgonbayar Z, Oh WC. MXene-based nanocomposite for the photocatalytic CO_2 reduction: Comprehensive review. Molecular Catalysis. 2023, 541: 113085. doi: 10.1016/j.mcat.2023.113085
35. Sreedhar A, Reddy IN, Noh JS. Photocatalytic and electrocatalytic reduction of CO_2 and N_2 by Ti_3C_2 MXene supported composites for a cleaner environment: A review. Journal of Cleaner Production. 2021, 328: 129647. doi:

10.1016/j.jclepro.2021.129647
36. Wang H, Li J, Li K, et al. Transition metal nitrides for electrochemical energy applications. Chemical Society Reviews. 2021, 50(2): 1354-1390. doi: 10.1039/d0cs00415d
37. Hu H, Wang X, Attfield JP, et al. Metal nitrides for seawater electrolysis. Chemical Society Reviews. 2024, 53(1): 163-203. doi: 10.1039/d3cs00717k
38. Gao B, Li X, Ding K, et al. Recent progress in nanostructured transition metal nitrides for advanced electrochemical energy storage. Journal of Materials Chemistry A. 2019, 7(1): 14-37. doi: 10.1039/c8ta05760e
39. Shan J, Sun K, Li H, et al. Composition regulation and defects introduction via amorphous CuEu alloy shell for efficient CO_2 electroreduction toward methane. Journal of CO_2 Utilization. 2020, 41: 101285. doi: 10.1016/j.jcou.2020.101285
40. Yang B, Zeng J, Zhang Z, et al. Kinetic-boosted CO_2 electroreduction to formate via synergistic electric-thermal field on hierarchical bismuth with amorphous layer. Journal of Energy Chemistry. 2024, 90: 233-243. doi: 10.1016/j.jechem.2023.11.022
41. Cao Y, Zheng D, Zhang F, et al. Layered double hydroxide (LDH) for multi-functionalized corrosion protection of metals: A review. Journal of Materials Science & Technology. 2022, 102: 232-263. doi: 10.1016/j.jmst.2021.05.078
42. Zhang J, Liu J, Xi L, et al. Single-Atom Au/NiFe Layered Double Hydroxide Electrocatalyst: Probing the Origin of Activity for Oxygen Evolution Reaction. Journal of the American Chemical Society. 2018, 140(11): 3876-3879. doi: 10.1021/jacs.8b00752
43. Zhang L, Peng J, Yuan Y, et al. Bifunctional heterostructure NiCo-layered double hydroxide nanosheets/NiCoP nanotubes/Ni foam for overall water splitting. Applied Surface Science. 2021, 557: 149831. doi: 10.1016/j.apsusc.2021.149831
44. Iwase K, Hirano T, Honma I. Copper Aluminum Layered Double Hydroxides with Different Compositions and Morphologies as Electrocatalysts for the Carbon Dioxide Reduction Reaction. ChemSusChem. 2021, 15(2). doi: 10.1002/cssc.202102340
45. Ma X, Liu T, Liu E, et al. Preparation and performance of Cd-MgAl-LDHs@RGO in high efficiency electrocatalytic reduction of CO_2 to CO. Molecular Catalysis. 2023, 535: 112876. doi: 10.1016/j.mcat.2022.112876
46. Zhang ZY, Tian H, Bian L, et al. Cu-Zn-based alloy/oxide interfaces for enhanced electroreduction of CO_2 to C^{2+} products. Journal of Energy Chemistry. 2023, 83: 90-97. doi: 10.1016/j.jechem.2023.04.034
47. He J, Dou T, Diao S, et al. Cu/Fe_3O_4 Nanocomposites from Layered Double Hydroxides as Catalysts for Selective Electroreduction of Carbon Dioxide. ACS Applied Nano Materials. 2023, 6(14): 13543-13550. doi: 10.1021/acsanm.3c02193
48. Ma Y, Chen F, Yang Q, et al. Sulfate radical induced degradation of Methyl Violet azo dye with CuFe layered doubled hydroxide as heterogeneous photoactivator of persulfate. Journal of Environmental Management. 2018, 227: 406-414. doi: 10.1016/j.jenvman.2018.08.030
49. Anantharaj S, Noda S. Amorphous Catalysts and Electrochemical Water Splitting: An Untold Story of Harmony. Small. 2019, 16(2). doi: 10.1002/smll.201905779
50. Tan BJ, Klabunde KJ, Sherwood PMA. X-ray photoelectron spectroscopy studies of solvated metal atom dispersed catalysts. Monometallic iron and bimetallic iron-cobalt particles on alumina. Chemistry of Materials. 1990, 2(2): 186-191. doi: 10.1021/cm00008a021
51. Wang WJ, Qiao MH, Yang J, et al. Selective hydrogenation of cyclopentadiene to cyclopentene over an amorphous NiB/SiO_2 catalyst. Applied Catalysis A: General. 1997, 163(1): 101-109. doi: 10.1016/S0926-860X(97)00125-7
52. Li T, Wang J, Zhu S, et al. Cu_3PdxN nanocrystals for efficient CO_2 electrochemical reduction to methane. Electrochimica Acta. 2021, 371: 137793. doi: 10.1016/j.electacta.2021.137793
53. Butt FA, Alshahrani T, Awan ZUH, et al. Electrochemical CO_2 reduction to gaseous methane and carbon monoxide using plasma-synthesized copper nanowires. Journal of Solid State Electrochemistry. 2023. doi: 10.1007/s10008-023-05600-z
54. Roy S, Li Z, Chen Z, et al. Cooperative Copper Single-Atom Catalyst in 2D Carbon Nitride for Enhanced CO_2 Electrolysis to Methane. Advanced Materials. 2024. doi: 10.1002/adma.202300713
55. Shang H, Kim D, Wallentine SK, et al. Ensemble effects in Cu/Au ultrasmall nanoparticles control the branching point for C_1 selectivity during CO_2 electroreduction. Chemical Science. 2021. doi: 10.1039/d1sc02602j
56. Zhang T, Verma S, Kim S, et al. Highly dispersed, single-site copper catalysts for the electroreduction of CO_2 to methane. Journal of Electroanalytical Chemistry. 2020, 875: 113862. doi: 10.1016/j.jelechem.2020.113862

57. Wang Q, Wang X, Wu C, et al. Electrodeposition of tin on Nafion-bonded carbon black as an active catalyst layer for efficient electroreduction of CO_2 to formic acid. Scientific Reports. 2017, 7(1). doi: 10.1038/s41598-017-14233-y
58. Ahn ST, Sen S, Palmore GTR. Grazing incidence X-Ray diffraction: identifying the dominant facet in copper foams that electrocatalyze the reduction of carbon dioxide to formate. Nanoscale. 2022, 14(36): 13132-13140. doi: 10.1039/d2nr03212k
59. Kattel S, Ramírez PJ, Chen JG, et al. Active sites for CO_2 hydrogenation to methanol on Cu/ZnO catalysts. Science. 2017, 355(6331): 1296-1299. doi: 10.1126/science.aal3573
60. El-Nagar GA, Haun F, Gupta S, et al. Unintended cation crossover influences CO_2 reduction selectivity in Cu-based zero-gap electrolysers. Nature Communications. 2023, 14(1). doi: 10.1038/s41467-023-37520-x

Appendix

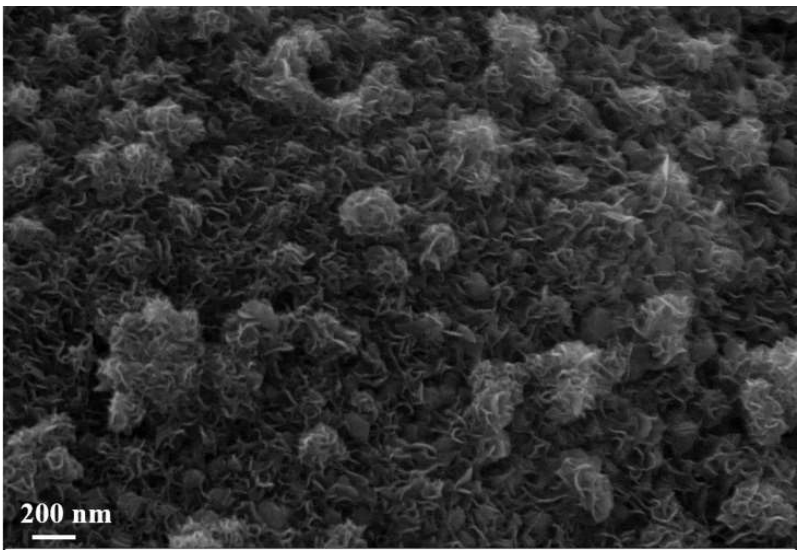

Figure A1. SEM images of $MoSe_2$.

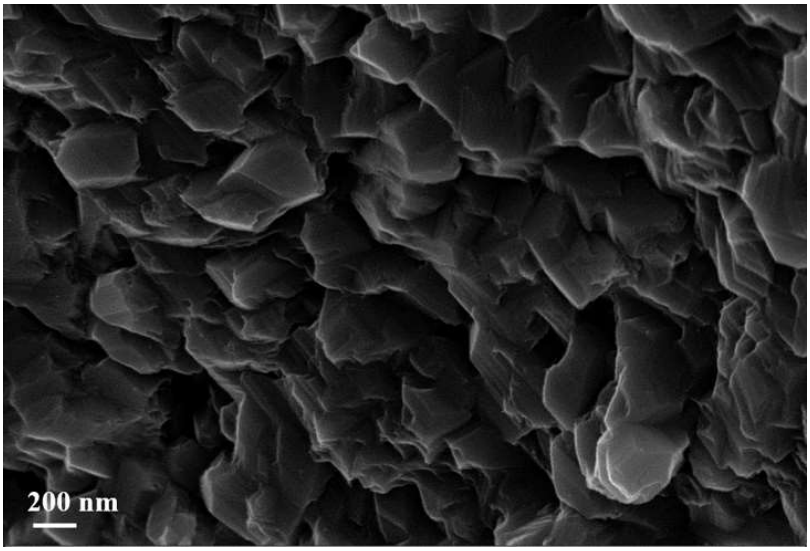

Figure A2. SEM images of $NiSe_2$.

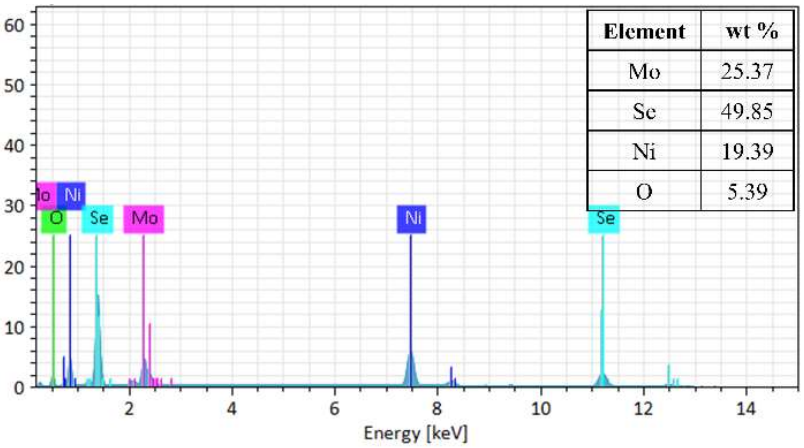

Figure A3. EDS spectrum of the $MoSe_2/NiSe_2$.

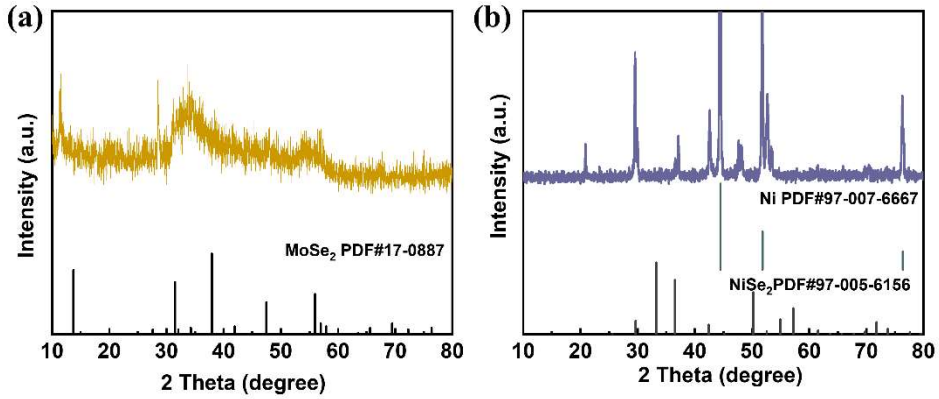

Figure A4. XRD patterns of **(a)** bare $MoSe_2$; **(b)** $NiSe_2$.

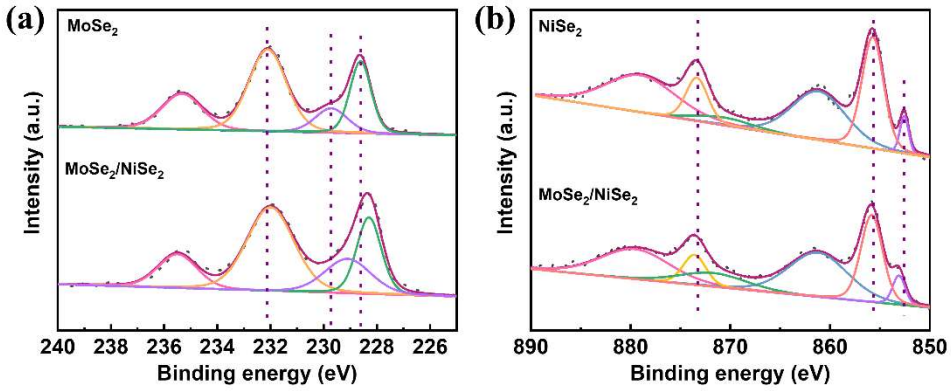

Figure A5. High-resolution XPS spectra of **(a)** Mo 3d in the $MoSe_2$ and $MoSe_2/NiSe_2$; **(b)** Ni 2p in the $NiSe_2$ and $MoSe_2/NiSe_2$.

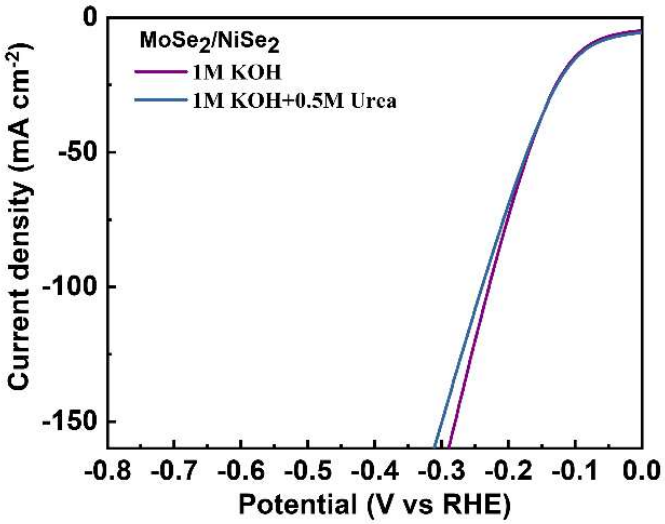

Figure A6. HER polarization plots of $MoSe_2/NiSe_2$ at a scan rate of 5 mV s^{-1} in 1 M KOH electrolyte with and without 0.5 M urea.

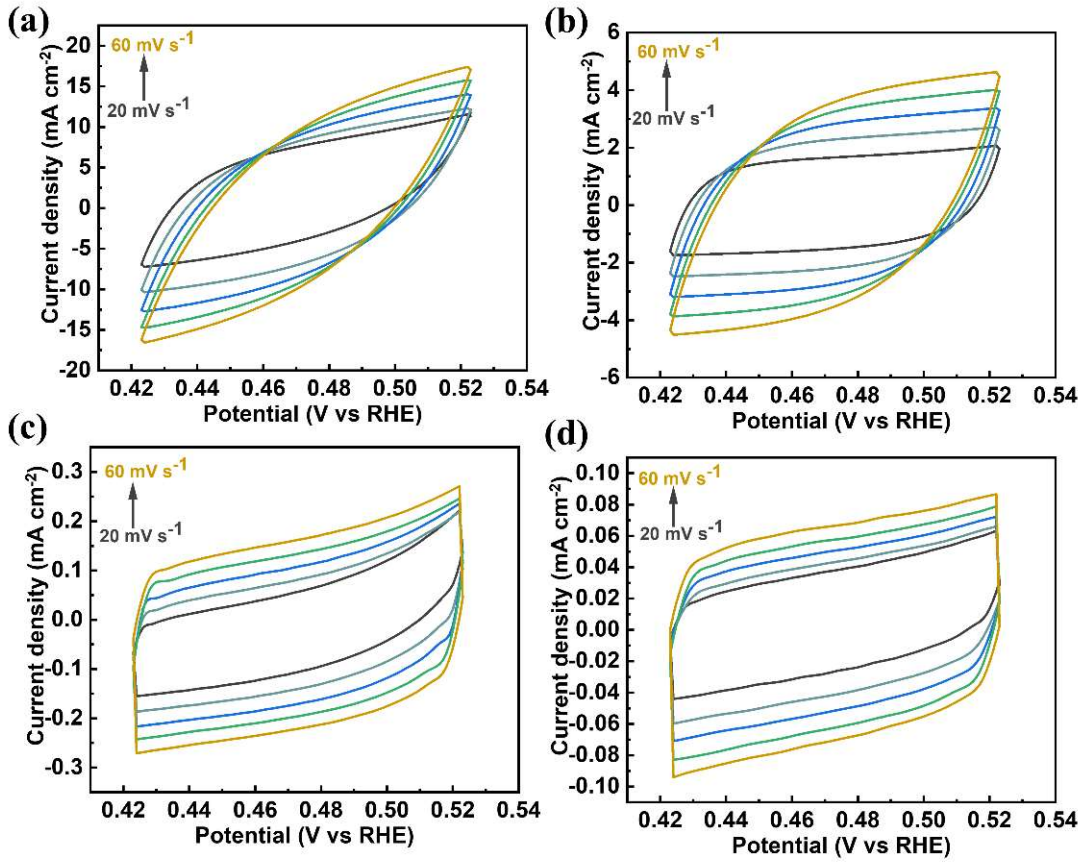

Figure A7. CV curves of **(a)** $MoSe_2/NiSe_2$; **(b)** $MoSe_2$; **(c)** $NiSe_2$; and **(d)** $NiMoO_4$/NF for HER in capacitive region at scan rates from 20 to 60 mV s^{-1} in 1 M KOH.

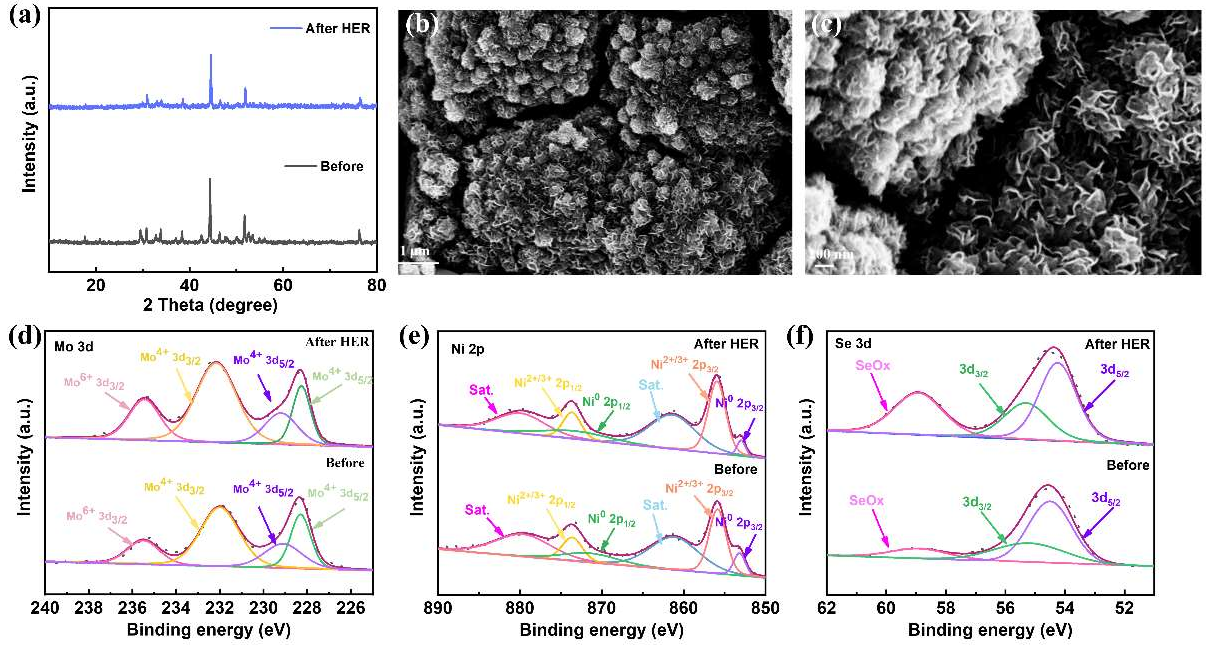

Figure A8. (a) XRD; **(b,c)** SEM images, high-resolution XPS spectra in the Mo 3d; **(d)** Ni 2p; **(e)** Se 3d; **(f)** of $MoSe_2/NiSe_2$ after HER durability test in 1M KOH.

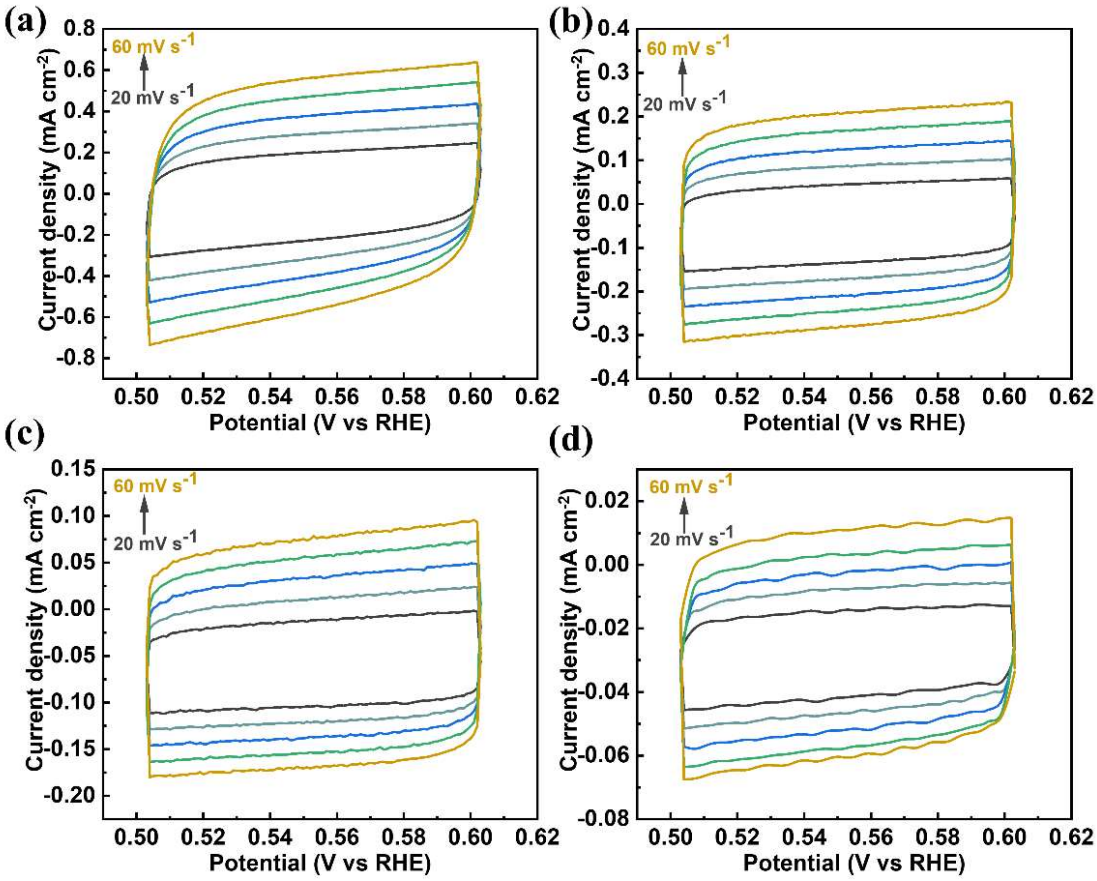

Figure A9. CV curves of **(a)** $MoSe_2/NiSe_2$; **(b)** $MoSe_2$; **(c)** $NiSe_2$; and **(d)** $NiMoO_4$/NF for UOR in capacitive region at scan rates from 20 to 60 mV s^{-1} in 1 M KOH+0.5M UOR.

Energy Storage and Conversion 2024, 2(2), 1151.
https://doi.org/10.59400/esc.v2i2.1151.

Article

AlZnO magnetron sputtered thin film for photovoltaic application

Zohreh Ghorannevis[1,*], Mehran Jamalpourkolour[1], Arash Boochani[2], Arash Yari[2], Nosratali Vahabzadeh[3], Parnia Goudarzi[4]

[1] Department of Physics, Karaj Branch, Islamic Azad University, Alborz, Iran
[2] Department of Physics, Kermanshah Branch, Islamic Azad University, Kermanshah, Iran
[3] Department of Physics, Parsabad Moghan Branch, Islamic Azad University, Parsabad Moghan, Iran
[4] Plasma Physics Research Center, Science and Research Branch, Islamic Azad University, Tehran, Iran
*** Corresponding author:** Zohreh Ghorannevis, ghorannevizohreh@gmail.com

CITATION

Ghorannevis Z, Jamalpourkolour M, Boochani A, et al. AlZnO magnetron sputtered thin film for photovoltaic application. 2024; 2(2): 1151. https://doi.org/10.59400/esc.v2i2.1151

ARTICLE INFO

Received: 5 March 2024
Accepted: 26 April 2024
Available online: 16 May 2024

Abstract: Aluminum zinc oxide (AZO) is a nontoxic and low-cost material that finds application as a transparent conducting electrode in photovoltaic devices. In this study, the (direct current) DC magnetron sputtering of AZO films is carried out at different deposition times of 5, 10, 15, 20, and 25 min's at room temperature, and its structural, optical, electrical, and morphological properties are studied for its use as a front contact for thin film solar cell application. The structural study suggests that the preferred orientation of grains along the (002) plane has a hexagonal structure, and the optical and electrical studies suggest that the films show an average transmission of 70% and a resistivity of the order of $10^{-4}\Omega$ cm. On the other hand, the scanning electron microscopy (SEM) images suggest the formation of packed grains with a homogeneous surface. Moreover, in order to study the optoelectronic properties of prepared samples, the electronic and optical calculations of the AZO are performed by the first-principles calculations using density functional theory (DFT).

Keywords: AZO; sputtering; photovoltaic; thin film solar cell; DFT

1. Introduction

Aluminum zinc oxide (AZO) is a transparent conducting oxide (TCO) material owing to its nontoxicity as well as its tunable optoelectronic properties [1–5]. AZO thin films are widely used in photonic devices such as light-emitting diodes (LED's) [6], thin film solar cells [7,8], flat panel displays [9], as well as sensing devices [10,11]. It is notable that the above applications require conductivity (sheet resistance <10 ohms per square) as well as high transmittance (>80%) in the visible region. There are different techniques to prepare AZO films, such as sputtering [12], electron beam evaporation [13], pulsed laser deposition [14], chemical vapor deposition [15], spray pyrolysis [16], and sol-gel deposition [17], that are well reported for preparing AZO thin films on different substrates. Direct current (DC) magnetron sputtering is an industrially acceptable technique due to its convenience, high deposition rate, and scalability over a large area [18]. Generally speaking, the most commonly preferred substrate of all TCO films is glass, and the physics properties of sputtered AZO thin films are highly sensitive to controlled process parameters such as base vacuum, gas pressure, substrate temperature, and deposition time. Therefore, in this study, optimized experimental conditions are found to investigate the effect of deposition time on the physical properties of AZO thin film deposited on soda lime glass substrate. The effect of deposition time is estimated on the structural, optical, morphological, and electrical properties in order to achieve the lowest resistivity and

the highest transparency for the films. On the other hand, the electronic and optical calculations of the AZO films are also performed by first-principles calculations using DFT in order to achieve more detailed studies on the prepared AZO thin film.

2. Materials and methods

Figure 1 shows a schematic diagram of a magnetron sputtering system that is used in these experiments. AZO thin films are deposited using a magnetron sputtering setup on a 3-inch-diameter target consisting of 98 wt% ZnO and 2 wt% Al_2O_3. It is worth nothing that the films are deposited at room temperature, and no oxygen is introduced in this process. First of all, the glass substrates are ultrasonically cleaned in sequentially distilled water, acetone, alcohol, distilled water, and finally dried with nitrogen gas. The substrates are then placed at a distance of a distance of 70 mm from the target. The sputtering chamber is first pumped to a base vacuum pressure of 10^{-6} Torr, and the Ar gas is introduced into the chamber. The sputtering gas pressure is set to be about 2×10^{-2} Torr. After the deposition, the samples are self-cooled and later examined for their physical properties. The surface morphology of the films and the crystal structure are studied using a field-effect scanning electron microscope (FESEM) and an X-ray diffractometer (XRD), respectively. A Dektak profilometer is also used to estimate the film thicknesses. The optical transmission measurements are also carried out with a spectrophotometer in the spectral region of 190–800 nm, and the atomic force microscope (AFM) images are also taken under the contact mode to evaluate the roughness of the films. Moreover, the resistivities of the films are measured using a four-point probe method.

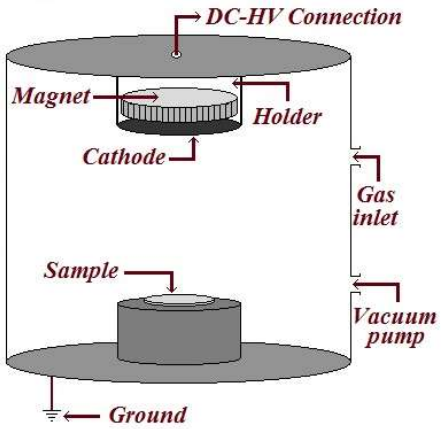

Figure 1. Schematic of magnetron sputtering setup.

3. Results

3.1. Experimental

AZO thin films prepared at different deposition times while keeping other experimental conditions constant are studied for their physical properties. By increasing the deposition time, the film thicknesses are also increased. **Table 1** gives the thicknesses of the AZO thin films prepared at different deposition times of 5, 10, 15, 20, and 25 min.

Table 1. Thicknesses of the AZO thin films prepared at different deposition times.

Thickness	Deposition time
210 nm	5 min
350 nm	10 min
520 nm	15 min
710 nm	20 min
1150 nm	25 min

Figure 2a shows the XRD spectra of AZO films grown at different deposition times. The XRD data's 5 min is not enough time to form the film, and the XRD data does not show any AZO peak. However, the film grown at the deposition time of 20 min shows a (002) peak with high intensity, which becomes much stronger, sharper, and narrower. A small diffraction intensity from (004) planes also appears in the XRD spectra. As it can be seen from **Figure 2b,** the (004) peak intensity is very low in comparison with the (002) peak intensity. Both peaks belong to AZO structures with two different planes. Moreover, a higher XRD intensity corresponds to improved film crystallinity for 20 min. It is clear that all the polycrystalline AZO thin films deposited on the glass substrates exhibit (002) crystallographic orientation due to the minimal surface energy in the ZnO hexagonal wurtzite structure. The appearance of a (002) peak in this spectra indicates that the films grown at different deposition times have a c-axis preferred orientation due to a self-texturing phenomenon [16].

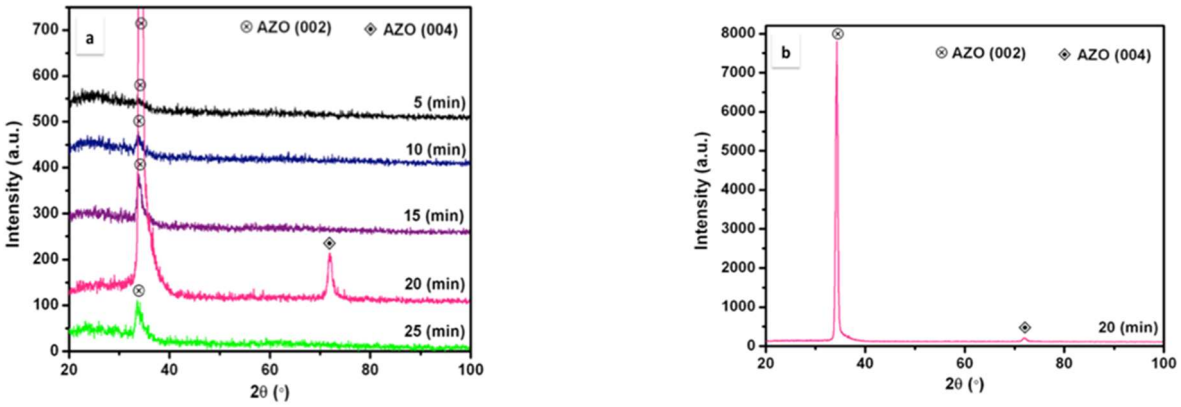

Figure 2. XRD spectra of AZO films deposited at **(a)** various deposition times; **(b)** 20 min.

From the XRD spectrum, the crystalline quality of the AZO thin films becomes weak for the higher deposition times (25 min), and no peaks corresponding to the Al_2O_3 phase are seen in the XRD pattern, which may be due to the aluminum replacing zinc substitutionally in the hexagonal lattice. From the XRD data, the average grain size of the AZO thin film can also be evaluated by the Debye-Scherrer equation [16] as follows:

$$\text{Grain size} = 0.9\,\lambda/\beta\cos\theta \quad (1)$$

where λ is the X-ray wavelength (0.154 nm), θ is the Bragg angle, and β is the full width at half maximum (FWHM) of the diffraction peak. The calculated crystal sizes of the thin films are more or less uniform for all the films, ranging from 8 to 19 nm

(**Table 2**). The maximum grain size is around 19.231 nm for the sample prepared at the 20 min deposition time.

Table 2. Calculated grain sizes and FWHM for AZO films grown at different deposition times for (002) peaks.

Time (min)	D-spacing (Å)	FWHM (degree)	Grain size (nm)
5	2.659	0.59	14.483
10	2.656	0.96	8.725
15	2.654	0.72	11.680
20	2.618	0.44	19.231
25	2.673	0.6	14.053

Figure 3 shows the graph of the FWHM of (002) and (004) XRD peaks and the corresponding grain sizes of the AZO thin films as a function of crystal planes. It is observable that the grain size for the (004) peak is larger, and the average grain size for both AZO crystal planes is around 20 nm.

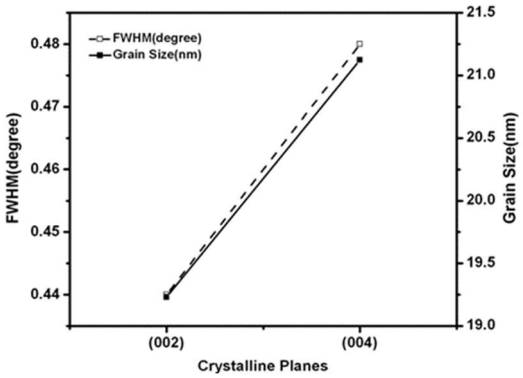

Figure 3. FWHM and grain size of (002) and (004) XRD peaks corresponding to the AZO thin film as a function of crystal planes.

Figure 4 shows the optical transmittance of the AZO thin films measured by a UV-VIS spectrophotometer in the frequency range of 200–800 nm. All the thin films sputtered at the different deposition times exhibit more than 70% transmittance in the visible region.

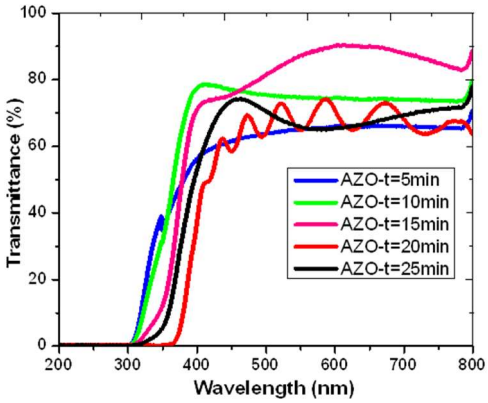

Figure 4. The transmission over the VIS range for AZO thin film at different deposition times.

An excellent surface quality and homogeneity of the film are confirmed by the appearance of interference fringes in the transmission spectra occurring when the film surface is reflecting without much scattering/absorption in the bulk of the film [17]. As can be seen in **Figure 5,** the film, which was prepared at 20 min shows these interference fringes. The electrical resistivity of the films is also given in **Table 3** for the different deposition times of the prepared samples. The lowest resistivity of the films is measured to be 4.1×10^{-4}. It can be seen that the resistivity increases as the deposition time increases to 20 min and then decreases as the deposition time increases to 25 min. Increasing the crystallite size of AZO thin films can decrease the grain boundary scattering and increase the carrier lifetime to achieve the lower resistivity of the AZO thin films.

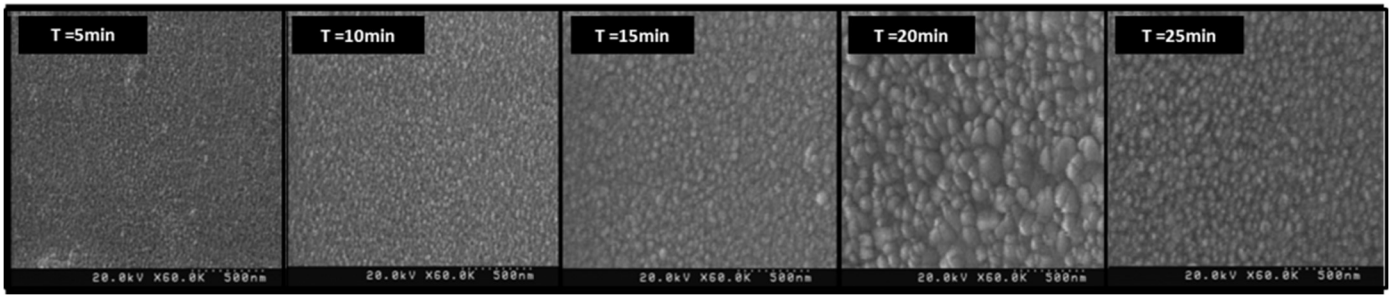

Figure 5. SEM images of AZO thin films at different deposition times.

Table 3. Electrical resistivities measured for the AZO thin films prepared at different deposition times.

Resistivity (Ωcm)	**Deposition time**
9.8×10^{-2}	5 min
3.6×10^{-2}	10 min
3.2×10^{-3}	15 min
4.1×10^{-4}	20 min
1.2×10^{-3}	25 min

SEM images of AZO are shown in **Figure 5**. These images can be used to study the AZO film surface morphology and microstructure, which show the surface micrographs of the films as a function of the deposition time. It is found that the deposition time has a great influence on the film surface structure. The AZO film deposited at 20 min shows surface features of densely packed grains and the grains that are aggregating.

Moreover, AFM images are given in **Figure 6** for the AZO thin films deposited at different deposition times. It is known that surface roughness is one of the important factors in the AZO thin film for many optoelectronic applications because the level of surface roughness will dominate carrier mobility and light scattering [19,20]. In **Figure 6**, the rough and non-uniform surface structures of the AZO thin films at the different deposition times are observed. The roughness of the films is given in **Table 4**. As it can be seen, the roughness is increased by increasing the deposition time to 20 min due to the density of the thin film, which is enhanced by increasing the deposition time.

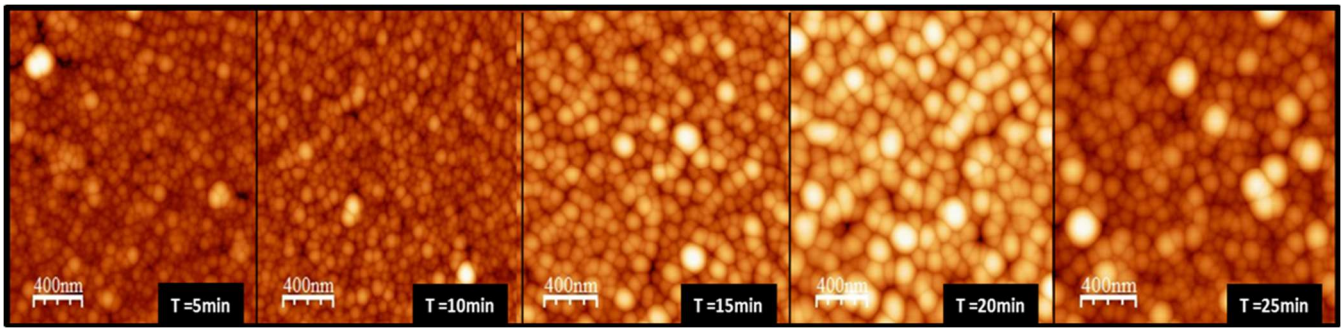

Figure 6. AFM images of AZO thin films deposited at different deposition times.

Table 4. Average roughnesses of the AZO thin films deposited at different deposition times.

Roughness	Deposition time
28.4 nm	5 min
33.4 nm	10 min
48.7 nm	15 min
49.3 nm	20 min
38.4 nm	25 min

3.2. Computational

The electronic and optical calculations of the AZO film are performed by first-principles calculations using density functional theory (DFT) [21–23]. Solving the Kohn-Sham equations is done using the full potential method of linear augmented waves (FP-LAPW) [24], which is used in the WIEN2k package [25]. The PBE-GGA approximation is used to solve the exchange-correlation potential for greater accuracy [26]. The optimized input parameters, including RKmax, KPoint, lmax, and separation energy, are selected as 8.0, 10 × 10 × 2, 10 and –7.0 Ryd, respectively. The muffin tin values of the Zn, O, and Al atoms are selected at 2.20 a.u., 1.45 a.u., and 1.8 a.u., respectively. The force convergence of the relaxation calculations is 10^{-6} dyn/a.u., and the optical calculations are approximated by the random phase approximation (RPA) with 15 × 15 × 2KPoint in the first Brillouinzone. In **Figure 7**, panel (a), the density of electronic states (DOS) of ZnO with an Al impurity of 2% is calculated with an mBJ approximation. This diagram shows that this compound has a very weak conductivity because the electron states are partially present in the Fermi level, and in the region below the Fermi level (valence area), a 2 eV gap is seen. In the –4 eV region, there are many electron states towards the lower energies of the valence region, and also in the region of –4 eV to –9.5 eV the Van Hov singularity is observed. Therefore, during the radiation or applying the heat, there is a suitable source for excited electrons. In panel (b), the partial DOS are shown.

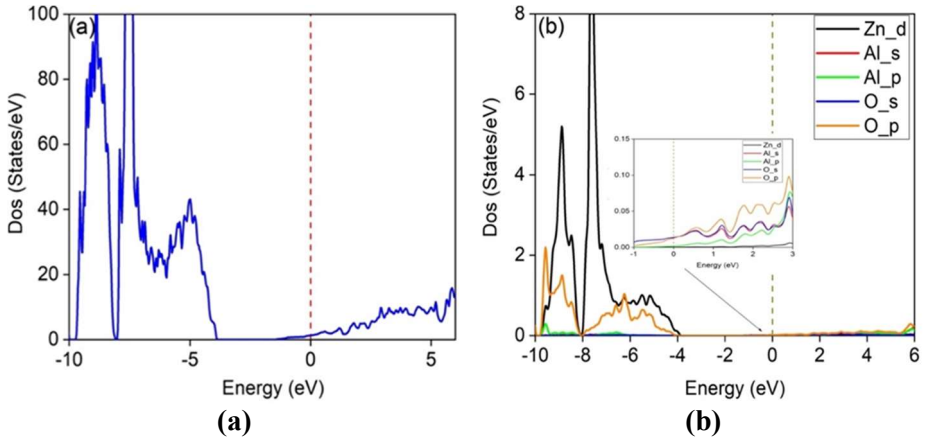

(a) **(b)**

Figure 7. (a) the density of electronic states (DOS) of ZnO with Al impurity of 2%; **(b)** the partial DOS.

It can be seen that in the valence region, the main contribution of the density of electronic states belongs to the d-Zn and p-O orbitals, and the p-O, s-O, and s-Al orbitals have the main role at the Fermi level and conduction region.

In **Figure 8**, the band structure of ZnO:Al with a 2% impurity percentage is depicted in the symmetry direction M→K→Γ→A →Γ in the first Brillouin zone. It can be seen that in the region of –9.5 eV to –4 eV, a high density of electron levels is shown, which is in perfect agreement with the DOS curves. In the region of –4.5 eV to –1.5 eV and above –1.5 eV of the Fermi level, an energy gap and electron level belonging to the s-Al orbital are given, respectively, which intersect the Fermi level. Due to the appropriate slope of this level curve, it helps the excited electrons move to the conduction region. Another point is that the gradient of the conduction region is higher than the valence region, so the excited electrons are well placed in the conduction current.

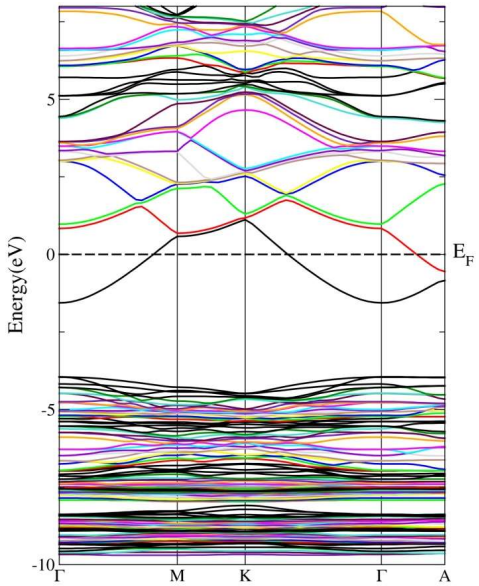

Figure 8. the band structure of AZO with 2% impurity percentage in the first Brillouin zone.

In **Figure 9**, the optical diagrams of this compound are examined. Due to the inclusion of Al impurities in the ZnO structure, its cubic symmetry is disturbed. Due to the asymmetry in the arrangement of atoms after the Al impurity atom enters the ZnO compound, the response of this compound to the light irradiated in different directions is different. Therefore, the optical behavior of the AlZnO compound was investigated in two crystal directions, x and z, which we have distinguished in the optical diagrams. Panel (a) shows the real part of the dielectric function, whose static value along the z-axis shows poor metallic behavior. However, as soon as the energy of the radiated photon increases, the dielectric function diagram is strongly reduced in Dirac form and reduced to zero and negative values, and it reaches 2.7 in the UV and visible regions. It remains constant up to the range of 8 eV.

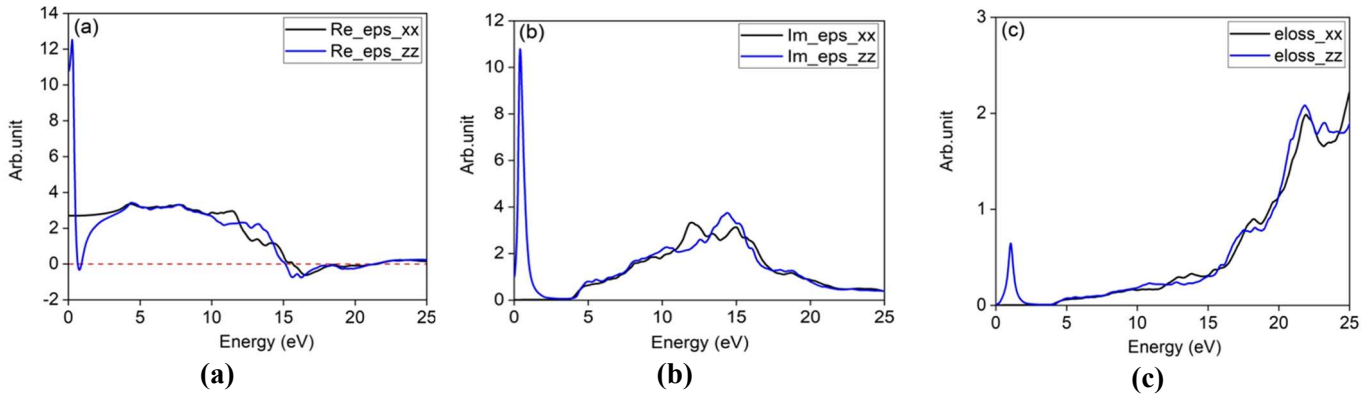

(a) **(b)** **(c)**

Figure 9. (a) real part; **(b)** imaginary part; **(c)** the spectrum of the loss of dielectric function in both x and z directions.

With radiation along the x-axis, its static value is 2.7, and it remains in this range up to 10 eV. From 10 eV onwards, this function is reduced in both directions, and at 15 eV to 20 eV, it will have negative values.The low value of the true dielectric function of this composition can be an indicator of the transparency of this composition. Panel (b) shows the imaginary part of the dielectric function in both x and z directions. Along the z-axis, we see a sharp Dirac peak that becomes zero with the increase of the emitted photon energy at the visible edge, which is consistent with the metallic behavior of this composition. Along the x-axis up to the range of 4 eV of the UV edge, a gap that increases with the increase in the energy of the irradiated photon is seen, and it has reached its maximum values from 15 to 14 eV; therefore, the electron transition occurs more at high energy. In panel (c), the spectrum of the loss function can be seen. There is a small peak in the z direction in the infrared range, which confirms the behavior of the metal. In the visible and UV ranges, the loss values are very small, and the most loss occurs in the 15 eV region. By comparing this diagram with the previous two diagrams, the transparency of this optical behavior in the infrared, visible, and UV regions is confirmed.

In **Figure 10**, the absorption, reflection coefficient, and refraction coefficient for the AZO composition are drawn. As can be seen in the absorption diagram, there is practically no absorption up to the UV edge, except for a very small peak in the direction of the z-axis, which, compared to the curves in **Figure 7**, concludes that this compound acts like a transparent material in the visible, UV, and IR regions. Also, with the increase in energy of the emitted photon, the amount of absorption increases

in both directions. In panel (b), the reflection coefficient is specified for these two directions. In the z direction, its static value is around 30%, which, of course, decreases sharply with the increase of the radiated energy and increases in the visible region. In the x direction, the value of the reflection coefficient at low energies is around 8%, and with the increase in the energy of the radiated photon, even up to the range of 15 eV, the value of the reflection coefficient for both directions is in the range of 5% to 30%, and in the IR, visible, and UV regions, it is below 10%, which again emphasizes the transparency of this composition. In panel (c), the refractive index shows that its static value is 3.2 along the z axis and 1.7 along the x axis. In the direction of the z axis, an anisotropy can be observed at low energies, which is indicative of the poor metalic behavior, but with the increase in energy of the radiated photon in both directions, the refractive index is less than 2. 10 eV and more indicates the behavior of a vacuum. It is the kind that has confirmed the transparency of the composition again.

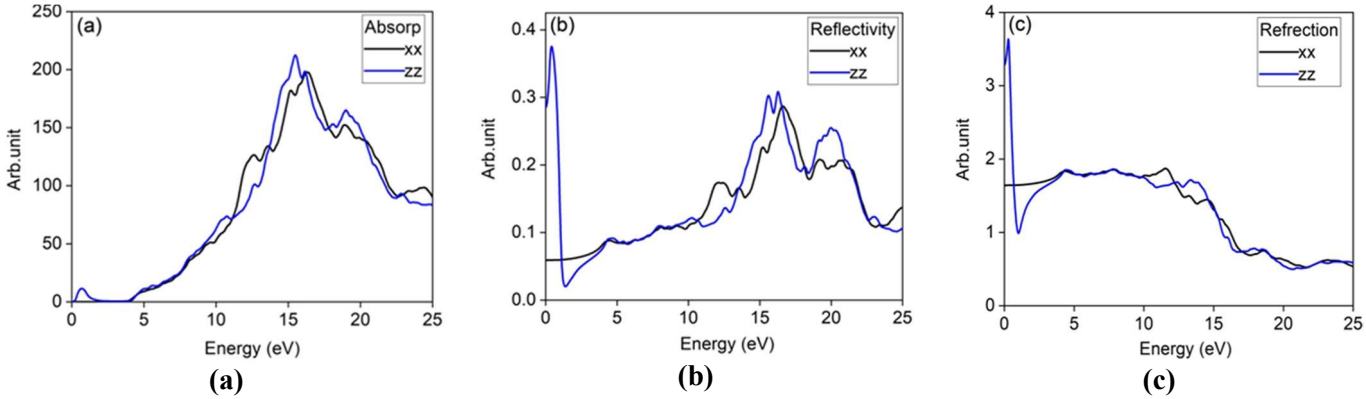

(a) **(b)** **(c)**

Figure 10. (a) absorption, **(b)** reflection coefficient, **(c)** refraction coefficient for AZO composition.

4. Discussion

AZO films are magnetron sputtered on the glass substrate at room temperature using DC magnetron sputtering to find the optimum experimental condition to make front contact for optoelectronic devices. The structural, morphological, optical, and electrical properties are studied, which suggest that the preferred orientation of grains along the (002) plane having a hexagonal structure is grown at a 20-minute deposition time that shows packed grains with a homogeneous surface. Moreover, this sample shows an average transmission of 70% and a resistivity of the order of 10^{-4} Ωcm. On the other hand, the electronic and optical calculations of the AZO are performed by first-principles calculations using density functional theory (DFT) to study more details on the physical properties of the films. DFT calculations also reveal that this compound acts like a transparent material. Therefore, experimental and theoretical results are in good agreement and confirm that the grown film has promising TCO material for optoelectronic applications.

5. Conclusion

The structural, electrical, morphological, and optical properties of AZO films deposited at room temperature on glass substrates by magnetron sputtering are

investigated to explore the possibility of producing transparent oxide films through a simple, low-cost process for photovoltaic applications. It is observed that the AZO thin films are grown with c-axis preferred orientations without degradation of the wurtzite ZnO structure. The electrical and optical properties of the AZO films improved with increasing deposition time. The higher crystallinity, lower resistivity, suitable roughness, and transmittance were obtained for the sample prepared at a 20-minute deposition time. The electronic and optical calculations of the AZO are also performed by the first-principles calculations using DFT for ZnO:Al composition with a 2% impurity percentage. This work suggests the possibility of producing AZO films with the required electrical and optical properties by a simple, low-cost process at room temperature.

Author contributions: Experimental, ZG; software, AB, AY and NV; draft ptrparation; MJ and PG. All authors have read and agreed to the published version of the manuscript.

Conflict of interest: The authors declare no conflict of interest.

References

1. Badgujar AC, Yadav BS, Jha GK, et al. Room Temperature Sputtered Aluminum-Doped ZnO Thin Film Transparent Electrode for Application in Solar Cells and for Low-Band-Gap Optoelectronic Devices. ACS Omega. 2022; 7(16): 14203-14210. doi: 10.1021/acsomega.2c00830
2. Aïssa B, Hossain MI. Photonic Cooler Based on Multistacked Thin Films with Near-Infrared Filter Properties. ACS Omega. 2024; 9(3): 3295-3304. doi: 10.1021/acsomega.3c05561
3. Pal S, Basak D. Interaction of an Ultrathin Zinc Surface Passivation Layer with a Room Temperature-Deposited Al-Doped ZnO Film Leading to Highly Improved Electrical Transport Properties. The Journal of Physical Chemistry C. 2023; 127(29): 14439–14449. doi: 10.1021/acs.jpcc.3c02329
4. Petrova D, Napoleonov B, Minh CNH, et al. The Effect of Post Deposition Treatment on Properties of ALD Al-Doped ZnO Films. Nanomaterials. 2023; 13(5): 800. doi: 10.3390/nano13050800
5. Yang B, Yao C, Yu Y, et al. Nature Degradable, Flexible, and Transparent Conductive Substrates from Green and Earth-Abundant Materials. Scientific Reports. 2017; 7, 4936. doi: 10.1038/s41598-017-04969-y
6. Chauhan RN, Tiwari N, Anand RS, et al. Development of Al-doped ZnO thin film as a transparent cathode and anode for application in transparent organic light-emitting diodes. RSC Advances. 2016; 6(90): 86770–86781. doi: 10.1039/c6ra14124b
7. Dimitrov D, Tsai CL, Petrov S, et al. Atomic Layer-Deposited Al-Doped ZnO Thin Films for Display Applications. Coatings. 2020; 10(6): 539. doi: 10.3390/coatings10060539
8. Badgujar AC, Dusane RO, Dhage SR. Cu(In,Ga)Se2 thin film solar cells produced by atmospheric selenization of spray casted nanocrystalline layers. Solar Energy. 2020; 209: 1–10. doi: 10.1016/j.solener.2020.08.080
9. Hjiri M, El Mir L, Leonardi SG, et al. Al-doped ZnO for highly sensitive CO gas sensors. Sensors and Actuators B: Chemical. 2014; 196: 413–420. doi: 10.1016/j.snb.2014.01.068
10. Yadav BS, Dey SR, Dhage SR. Effective ink-jet printing of aqueous ink for Cu (In, Ga) Se_2 thin film absorber for solar cell application. Solar Energy. 2019; 179: 363–370. doi: 10.1016/j.solener.2019.01.003
11. Samoei VK, Jayatissa AH. Aluminum doped zinc oxide (AZO)-based pressure sensor. Sensors and Actuators A: Physical. 2020; 303: 111816. doi: 10.1016/j.sna.2019.111816
12. Park KC, Ma DY, Kim KH. The physical properties of Al-doped zinc oxide films prepared by RF magnetron sputtering. Thin Solid Films. 1997; 305: 201–209. doi: 10.1016/S0040-6090(97)00215-0
13. Sahu DR, Lin SY, Huang JL. Improved properties of Al-doped ZnO film by electron beam evaporation technique. Microelectronics Journal. 2007; 38(2): 245–250. doi: 10.1016/j.mejo.2006.11.005

14. Venkatachalam S, Iida Y, Kanno Y. Preparation and characterization of Al doped ZnO thin films by PLD. Superlattices and Microstructures. 2008; 44(1): 127–135. doi: 10.1016/j.spmi.2008.03.006
15. Fragalà ME, Malandrino G, Giangregorio MM, et al. Structural, Optical, and Electrical Characterization of ZnO and Al-doped ZnO Thin Films Deposited by MOCVD. Chemical Vapor Deposition. 2009; 15(10–12): 327–333. doi: 10.1002/cvde.200906790
16. Romero R, Leinen D, Dalchiele EA, et al. The effects of zinc acetate and zinc chloride precursors on the preferred crystalline orientation of ZnO and Al-doped ZnO thin films obtained by spray pyrolysis. Thin Solid Films. 2006; 515(4): 1942–1949. doi: 10.1016/j.tsf.2006.07.152
17. Islam MR, Rahman M, Farhad SFU, et al. Structural, optical and photocatalysis properties of sol–gel deposited Al-doped ZnO thin films. Surfaces and Interfaces. 2019; 16: 120–126. doi: 10.1016/j.surfin.2019.05.007
18. Badgujar AC, Yadav BS, Jha GK, et al. Room Temperature Sputtered Aluminum-Doped ZnO Thin Film Transparent Electrode for Application in Solar Cells and for Low-Band-Gap Optoelectronic Devices. ACS Omega. 2022; 7(16): 14203–14210. doi: 10.1021/acsomega.2c00830
19. Ilican S, Caglar M, Caglar Y. Determination of the thickness and optical constants of transparent indium-doped ZnO thin films by the envelope method. Materials Science-Poland. 2007; 25(3): 709-718.
20. Wu HW, Chu CH, Chen YF, et al. Study of AZO Thin Films Under Different Ar Flowand Sputtering Power by RF Sputtering. In: Proceedig of the International Multiconference of Engineers and Computer Scientists 2013; 13–15 March 2013; Hong Kong.
21. Born M, Oppenheimer R. Zur Quantentheorie der Molekeln. Annalen der Physik. 1927; 389(20): 457–484. doi: 10.1002/andp.19273892002
22. Hohenberg P, Kohn W. Inhomogeneous Electron Gas. Physical Review. 1964; 136(3B): B864–B871. doi: 10.1103/physrev.136.b864
23. Kohn W, Sham LJ. Vibrational frequency prediction using density functional theory Physical Review. 140(1965) 1133.
24. Kohn W, Sham LJ. Self-Consistent Equations Including Exchange and Correlation Effects. Physical Review. 1965; 140(4A): A1133–A1138. doi: 10.1103/physrev.140.a1133
25. Blaha P, Schwarz K, Sorantin P, Trickey SB. Full-potential, linearized augmented plane wave programs for crystalline systems. Computer Physics Communications. 1990; 59(2): 399–415. doi: 10.1016/0010-4655(90)90187-6
26. Blaha P, Schwarz K, Madsen G, et al. WIEN2k: An APW+lo program for calculating the properties of solids. The Journal of Chemical Physics. 2020; 7(152): 074101. doi: 10.1063/1.5143061

Energy Storage and Conversion 2024, 2(2), 309.
https://doi.org/10.59400/esc.v2i2.309

Article

Experimental exploration of nano-phase change material composites for thermal management in Lithium-ion batteries

Vishnu M., Anooplal B., Rajesh Baby*

Department of Mechanical Engineering, St. Joseph's College of Engineering and Technology, Palai 686579, Kerala, India
*** Corresponding author:** Rajesh Baby, rajeshbaby@sjcetpalai.ac.in

CITATION

M. V, B. A, Baby R. Experimental exploration of nano-phase change material composites for thermal management in Lithium-ion batteries. Energy Storage and Conversion. 2024; 2(2): 309. https://doi.org/10.59400/esc.v2i2.309

ARTICLE INFO

Received: 9 November 2023
Accepted: 18 April 2024
Available online: 24 May 2024

Abstract: The present study reports an experimental investigation carried out for the thermal management of cylindrical lithium-ion battery simulators using aluminum oxide (nano particle)-eicosane (phase change material) composites. The experiment involves varying the power input from 4 to 10 W in 2 W increments and adjusting the weight percentage of nanoparticles (wt%) from 0.5 to 0.9 in 0.2 wt% intervals. The examination of battery temperature evolutions in response to heating power, a comprehensive heat transfer analysis incorporating the Nusselt number, the determination of the maximum temperature difference, thermal resistance analysis, and the exploration of temperature variations in the absence of Phase Change Material (PCM) are considered. The results show that an increase in the weight percentage of alumina nanoparticles in phase-change material cannot always improve the thermal performance. The results of the present study give guidelines for designing battery thermal management systems. The power levels used in the experiment vary from 4 W to 10 W in steps of 2 W. For a power level of 4 W, the heat flux is 1.088 kW/m^2, and for a power level of 10 W, the heat flux is 2.72 kW/m^2.

Keywords: nanomaterials; thermal management; phase change materials; mock up battery

1. Introduction

The need for power storage and sources has been steadily increasing due to technological advancements, with approximately 80% of this energy being sourced from fossil fuels. However, it's crucial to shift focus towards renewable, sustainable, and environmentally friendly energy sources. Billions of batteries are manufactured annually, highlighting their significance in various comfort and safety applications. Enhancing the power performance and lifespan of batteries is imperative. Factors such as round-trip efficiency, electrochemistry, reliability, power, energy capability, and cycle life are greatly influenced by high temperatures. Efficient thermal management systems are necessary for effective heat dissipation during battery charging and discharging processes. Integrating phase change materials (PCM) into battery thermal management systems (BTMS) can offer an efficient, reliable, and eco-friendly solution, particularly for fluctuating discharge systems. Recent research has investigated the heat transfer properties of base fluids using suspended nanometer-sized solid particles, or nanoparticles, which enhance heat transfer efficiency. Combining PCM with nanoparticles holds promise for maintaining battery temperatures within safe limits. Khlissa et al. [1] explored the critical role of PCMs in thermal energy storage, essential for reducing building energy consumption and achieving net-zero energy goals. Despite their growing importance, PCMs faced limitations due to subpar heat conductivity. The study extensively categorized and

examined PCM features, highlighting recent advancements in nanoencapsulated PCM techniques and thermal energy storage technology. The assessment underscored researchers' efforts in enhancing PCMs, particularly through nano-enhanced PCMs.

Many researchers have experimentally studied the thermal management of LIB using phase change material. Arshad et al. [2] explored the thermal performance enhancement in pin-fin heat sinks by employing n-eicosane as a PCM. Various configurations with different volumetric fractions of n-eicosane and aluminum thermal conductivity enhancers (TCEs) were investigated to optimize cooling efficiency. Results indicated that a 2 mm-thick pin-fin heat sink with n-eicosane provided the most effective thermal performance, ensuring reliable temperature control for electronic packages. In their study, Wang et al. [3] investigated the thermal performance of cylindrical batteries using a composite paraffin and fin structure. They found that the composite fin structure effectively managed higher heat densities with minimal thermal resistance and extended operational durations. Experiments were conducted with both pure PCM and finned cases, revealing that the composite PCM-fin system displayed superior thermal performance compared to pure PCM.

Similarly, Hussain et al. [4] conducted experiments employing graphene-coated nickel foam saturated with PCM to analyze thermal management in lithium-ion batteries (LIBs). Their findings indicated a significant improvement in the thermal conductivity of pure paraffin wax by 23 times after infiltration into GcN foam. Moreover, the freezing and melting temperatures of graphene-coated nickel foam saturated with paraffin wax were altered compared to pure paraffin. In a separate study, Babapoor et al. [5] investigated the thermal performance of a LIB simulator in the presence of PCM. Their results demonstrated that a mixture of PCM with 2 mm-long carbon fibers at a mass percentage of 0.46% exhibited the most favorable thermal performance, leading to a reduction in temperature rise within the battery simulator by nearly 45%.

Situ et al. [6] proposed a double copper mesh-phase change material plate (DCM-PCMP) method for heat dissipation, specifically tailored for rectangular battery modules. This approach effectively increased thermal conductivity and, when combined with air-cooling, significantly improved thermal management, reducing internal battery temperature and power consumption. Karimi et al. [7] investigated thermal management in cylindrical lithium-ion batteries (LIBs) using different phase change material (PCM) composites. By mixing pure PCM with Ag, Cu, and Fe_3O_4 nanoparticles and a metal matrix, they enhanced thermal conductivity. Ag nanoparticle-PCM composites exhibited superior performance, while metal matrix-PCM composites loaded with PCMs achieved the lowest battery body temperatures. Pan and Lai [8] studied the thermal performance of LIBs using copper/paraffin composite phase change material (CPCM). They tested four heat dissipation methods under various discharging currents and found that CPCM effectively absorbed heat, reducing battery temperature by about 50% compared to natural wind cooling with uniform temperature distribution.

Wang et al. [9] explored the use of paraffin and paraffin/aluminum foam composite PCM for LIB thermal management. They observed improved melting processes and temperature uniformity with the addition of aluminum foam, with the composite PCM exhibiting significantly higher effective thermal conductivity

compared to pure paraffin. Ling et al. [10] investigated two PCM composites with different thermal conductivities and their impact on battery thermal performance. They found that the RT44 HC/EG composite outperformed the RT44 HC/fumed silica composite, reducing the maximum temperature difference by up to 60 °C. Hussain et al. [11] developed a nickel foam-paraffin wax composite for thermal management of high-power LIBs, demonstrating a 31% and 24% reduction in temperature compared to natural cooling and pure PCM, respectively, at discharge rates less than 2 °C.

Bai et al. [12] proposed a LIB module with a phase change material/water cooling plate, effectively cooling the battery's heat generation area and preventing thermal runaway. The PCM between adjacent batteries improved temperature uniformity. Rao et al. [13] utilized a battery module with six cells along flow channels to study the effects of aluminum block length and velocity on thermal performance, finding that maximum temperature remained under 40 °C with specific inlet conditions.

Wu et al. [14] developed a paraffin/expanded graphite composite-based battery module (PCM module) and a two-dimensional thermal model, recommending a weight fraction of 15%–20% for expanded graphite for optimal thermal management. Alipanah and Li [15] investigated the thermal management system of LIBs using pure octadecane, pure gallium, and octadecane-Al foam composite materials, observing improved discharge time and reduced battery surface temperature with the use of composite materials. Jiang et al. [16] developed a tube-shell LIB pack with a PCM passive thermal management system coupled with forced air cooling, ensuring uniform temperature distribution and high heat dissipation efficiency.

Zhao et al. [17] optimized a steel cell with a PCM thermal management system using numerical simulation, achieving uniform temperature distribution and increased energy density. Lazrak et al. [18] studied thermal conductivity enhancement and PCM melting temperature effects using integrated BTMS, developing a prototype based on numerical studies. Babu Sanker and Baby [19] provided a review of the thermal performance of various thermal conductivity enhancers in PCM-based thermal management of LIBs, summarizing advancements in the field.

The research delves into the characteristics of nano-enhanced PCMs. The study focuses on investigating the unique properties and performance improvements resulting from the integration of nanomaterials in PCMs. Insights gained from these studies contribute to advancing the understanding and potential applications of nano-enhanced PCMs in various thermal management systems. Liu et al. [20] studied the impact of optical properties with the use of glazing structures incorporated with PCMs. The study revealed that the refractive index of the PCM had a limited effect on various parameters, while the extinction coefficient significantly influenced temperature characteristics and optical properties. The research suggested caution in using liquid PCM with a large extinction coefficient for optimal light utilization but deemed a high extinction coefficient in solid PCM acceptable for efficient energy utilization. Li et al. [21] investigated the thermo-physical parameters of PCM and the thermal performance of a PCM-filled double glazing unit. Results indicated that increased density, latent heat, and melting temperature of the PCM effectively improved thermal performance, resulting in an elevated temperature time lag and reduced temperature decrement factor. However, the study found that enhancing thermal conductivity and specific heat capacity became ineffective beyond certain thresholds, specifically when

thermal conductivity exceeded 2.1 W/(m K) and specific heat capacity was less than 4460 J/(kg K).

The application of PCM involves harnessing its ability to absorb and release thermal energy during phase transitions. This technology is widely used in various industries, such as building construction and electronics, to enhance thermal performance and energy efficiency. Salih et al. [22] found baffles attached alternately to the upper and lower walls. The channel contained PCM in the semi-cylinders, heated at a constant temperature, with cold air inducing convective and conductive heat transfers, fluid-structure interaction, and PCM melting. The findings, obtained through solving normalized mathematical equations with the finite element method and ALE scheme, revealed that increasing Reynolds number and decreasing the elasticity modulus of flexible baffles retarded the melting volume fraction, with notable effects on Nusselt number and pressure drop along the channel. Chen et al. [23] used PCM to cool lithium-ion batteries in electric cars. A cylindrical battery submerged in a PCM-filled chamber with varying fin configurations aimed to optimize cooling during the discharging process. Utilizing COMSOL Multiphysics software, simulations revealed that a battery with 15 fins exhibited optimal PCM melting performance initially, while the lowest maximum temperature and maximum liquid volume fraction occurred with 9 fins, providing valuable insights for effective battery cooling strategies. Ruhani et al. [24] simulated the cooling system of a two-dimensional LIB pack with nine cells, considering airflow at Reynolds numbers ranging from 80 to 140. The study, employing the finite element method, individually examined the temperature of each battery cell, assessed pressure drop, and analyzed the cooling system temperature. Results indicated that an increase in Reynolds number lowered the maximum temperature of the battery pack, while variations in intake size affected the maximum temperature of battery cells and intensified the pressure drop in the cooling system. Rashid et al. [25] highlighted the efficacy of latent heat energy storage using PCM to reduce energy consumption. Despite the fluctuating price of paraffin wax, a common PCM derived from fossil fuels, interest in bio-based PCMs for sustainable thermal energy storage grew. Bio-based PCMs, derived from readily available and biocompatible sources such as animal fat combinations and oils, were explored as a renewable alternative with reduced oxidation risk compared to paraffin wax. The study reviewed and discussed the selection, phase change mechanisms, combinations, preparation, and applications of bio-based PCMs, proposing improvements for diverse utilization in thermal energy storage applications. Kholsi et al. [26] conducted an investigation of a of a PCM energy storage tank utilizing carbon nanotube (CNT)-water nanofluid under actual climatic conditions in Ha'il, Saudi Arabia. Two configurations, with and without conductive baffles, were examined. The tank, filled with encapsulated paraffin wax as PCM and circulating CNT-water nanofluid, aimed to raise PCM temperature to 70 ℃ for thermal energy storage during night and cloudy weather. Finite element method simulations, based on measured weather conditions over three months (December, March, and July), revealed that CNT-nanofluid usage reduced charging time and enhanced performance, with the best results observed in July due to high solar irradiation. Additionally, baffles showed no beneficial effects on the melting process.

From the preceding discussions, it is clear that several investigations have been carried out to study the thermal management of cylindrical LIB. But experimental investigations using nanofluids are scarce. Thus, the aim of the present work is to

1) To perform experiments in order to determine the effect of the following parameters on the heat transfer performance.
   - Different concentrations of nanofluid—0.5 wt%, 0.7 wt% and 0.9 wt%.
   - Various input power levels—4 to 10 W in steps of 2 W.
2) To compare the performance of battery without phase change material.

In the present study, thermal management of lithium-ion batteries (LIB) using nanophase change material composites in different concentrations (Case 1, Case 2, Case 3) is done. Case 2 demonstrates optimal battery temperature reduction, enhanced heat transfer, and the lowest thermal resistance. Nusselt number enhancement of 20% is observed, with a remarkable 70% reduction in battery temperature. Case 2 limits the temperature difference to 50 ℃ and cools the battery below 40 ℃ within 200 seconds at a 4 W heat input. These findings highlight the effectiveness of nano-based PCM composites for improved battery thermal management.

2. Experimental setup

The test setup comprised a simulated battery heater enclosed within a metal casing and filled with phase change material (PCM) in between. The mock battery, constructed from aluminum, measured 18 mm in diameter and 65 mm in height. It featured a concentric hole of 6 mm diameter at the center to accommodate a heater (3.56 cm in diameter and 5 cm in length), replicating the heat generation of a commercial 18,650 lithium-ion battery (LIB). The battery, with or without aluminum oxide nanoparticles, was positioned vertically within an aluminum housing with an inner diameter of 36 mm and a wall thickness of 10 mm. To insulate the battery from the metal housing, the sides and bottom were shielded with a 25-mm layer of nylon. With slight modifications to the procedures described by Radhakrishnan et al. [27] and Kothari et al. [28], nanoparticles are mixed with n-eicosane PCM. Initially, the required weight percentage of nanoparticles was carefully measured and added to heated n-eicosane using a Rotek Magnetic Stirrer cum hot plate. After melting, the nanoparticle-infused PCM underwent sonication at 50 ℃ for 2 h using an Analab sonicator. To prevent sedimentation, the mixture was further homogenized for 30 minutes with a stirrer. The same procedure is followed for all weight percentages of nanoparticles. The PCM and eicosane used in this study were supplied by M/s Sigma Aldrich.

Nanoparticles with different weight fractions, namely, 0.50 wt%, 0.70 wt%, and 0.90 wt%, are used in conjunction with PCM, and the case without nanoparticles (pure PCM) is used as a baseline for comparison. The battery temperature was measured by nine calibrated K-type thermocouples. The experiment was started by turning on the data acquisition system (Keysight 34972A) and power supply. **Figure 1** shows the photograph of the experimental setup used in the present study.

Figure 1. A photograph of the experimental setup used.

2.1. Model assembly

The mock-up battery, metal housing, insulation cavity, heater and acrylic plate are assembled to form the model assembly. **Figure 2** represents the design of the model assembly.

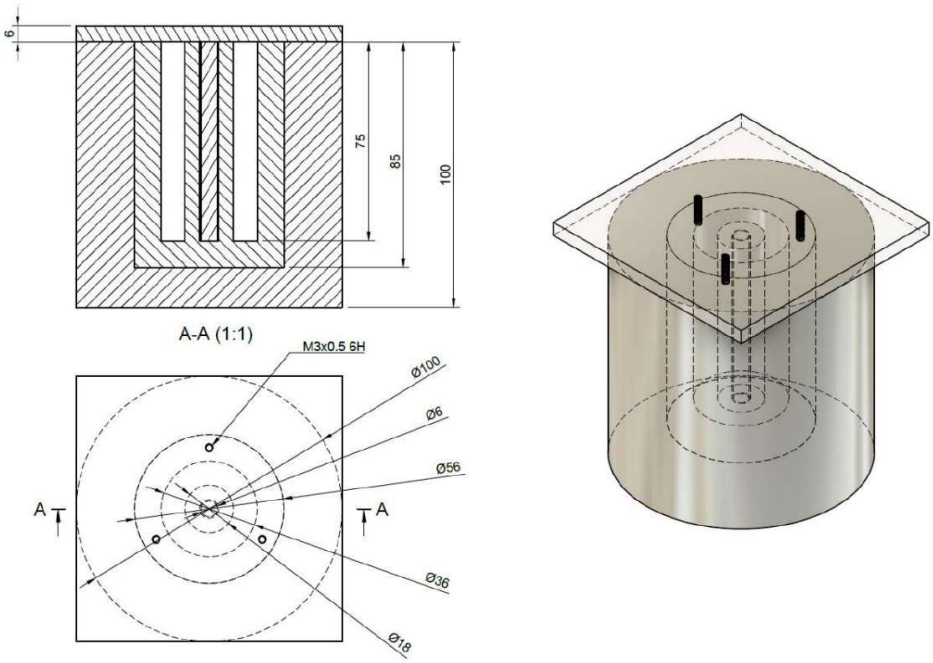

Figure 2. Schematic of the model assembly.

The mock up battery screwed in acrylic plate and bolted top of metal housing. The cartridge heater was inserted into the hole drilled at the centre of the mock-up battery. The thermocouple fixed at various positions and PCM composites melted and poured into the metal housing. The thermocouple wires are taken out through the holes made at the acrylic plate.

2.2. Equations used in the present study

The PCM (eicosane)-based alumina nanocomposites with mass concentrations of 0.5, 0.7, and 0.9 wt% and pure PCM were used to investigate the thermal management of cylindrical LIB. The temperature drops between the battery temperature at the

effective thermal control point (T_c) and the maximum melting temperature of PCM (T_m) are of particular interest to evaluate its thermal performance. The overall thermal resistance of the system is calculated from:

$$R_{cm} = \frac{T_c - T_m}{Q} \quad (1)$$

where Q is the heat input. In the present heat transfer analysis, the instantaneous Nusselt number is defined with the instantaneous battery to the housing temperature difference, namely,

$$N_u = \frac{QW}{(Tb - Tw)A_b\, k_f} \quad (2)$$

The Nusselt number shows the quality of heat transfer.

2.3. Uncertainty analysis

The results of the uncertainty analysis of the experiments are reported in **Table 1**. The final uncertainty in power was estimated to be ±2.4% for a power level of 4 W.

Table 1. Results of the uncertainty analysis.

Sl. no.	Quantity measured	Uncertainty
1	Temperature	±0.2 ℃
2	Voltage	±0.1 V
3	Current	±0.01 A
4	Power input	±2.4%

3. Results and discussion

The experiment involved utilizing power levels ranging from 4 W to 10 W in increments of 2 W. At 4 W, the heat flux measured 1.088 kW/m^2, while at 10 W, it reached 2.72 kW/m^2. The objective of this investigation is to analyze the thermal properties of the composite PCM-nanoparticle-based thermal management system. **Table 2** provides the nomenclature list for the samples.

Table 2. List of nomenclatures of samples.

Sample	Label
Pure PCM	Case 1
0.50 wt % Nano -PCM composites	Case 2
0.70 wt % Nano -PCM composites	Case 3
0.90 wt % Nano- PCM composites	Case 4

3.1. Battery temperature evolutions with heating power

Experiments were carried out on the batteries contained in the housing for various cases, as described in this section. The detailed battery temperature graph for 8 W is described in **Figure 3**. Case 2 shows the lower battery temperature curve. As compared to the case 1 about 4 ℃ to 6 ℃ difference is shown by case 2. All the nano-based PCM composites show better heat transfer performance than Case 1. The nanoparticle

addition to pure PCM increases the thermal conductivity of PCM composites and helps ensure uniform heat distribution inside the composites.

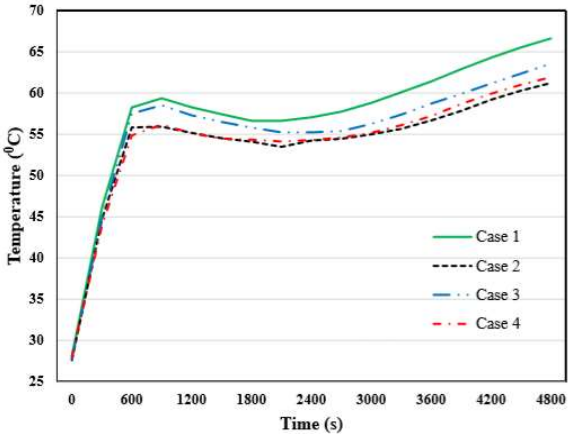

Figure 3. Battery temperature–time response for a heat input 8 W.

3.2. Heat transfer analysis with Nusselt number

In the case of Nusselt number (Nu) for heat input 8 W, case 2 and case 4 have superior Nusselt number values. Instantaneous Nusselt number for 8 W heat input is shown in the **Figure 4**.

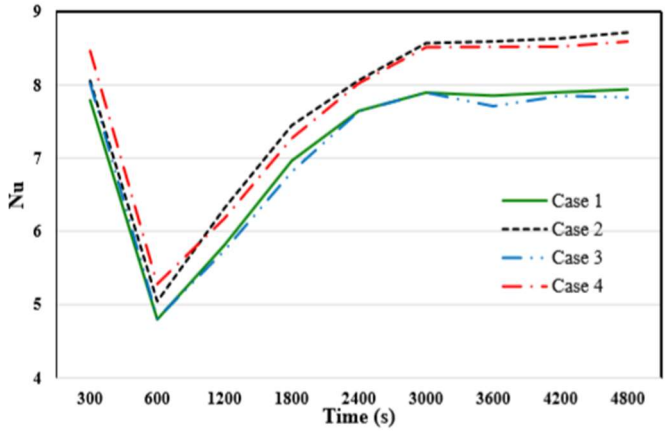

Figure 4. Instantaneous Nusselt number for heat input 8 W.

3.3. Maximum temperature difference

Battery thermal management has some main objectives, including decreasing battery body temperature, increasing the effective thermal conductivity of the cooling medium, and maintaining temperature uniformity inside the system by minimizing the temperature difference between the battery and cooling medium. The presence of nanoparticles in PCM can provide a better heat transfer path through the cooling medium. The maximum temperature difference at 4800 s for 4 W power is shown in **Figure 5**. Case 1 shows a greater maximum temperature difference of 13 °C. Case 2 has a lower maximum temperature difference of 3 °C. There is a temperature difference of around 10 °C between Case 1 and Case 2. Case 4 shows a higher maximum temperature difference among the three nano-PCM composites.

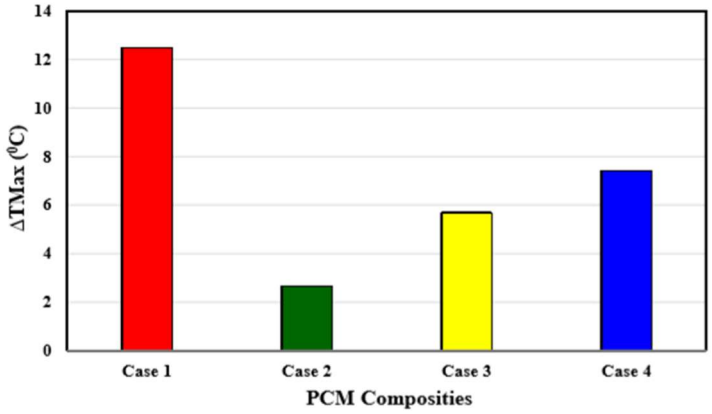

Figure 5. Maximum temperature difference at 4800 s for 4 W heat input.

3.4. Thermal resistance analysis

The thermal resistance is obtained from Equation (3)

$$R_{cm} = \frac{T_c - T_m}{q} \tag{3}$$

The obtained thermal resistance results for different nano-based PCM composites are discussed below. It is seen that the thermal resistance does decrease with the increase in percentage weight of nanoparticles in phase-change material. The improved heat transfer causes a decrease in thermal resistance within the thermal management system. **Figure 6** indicates the thermal resistance at an 8 W power level. Case 1 gives high thermal resistance, and Case 2 gives low thermal resistance and is suitable for better thermal management inside the system. Case 3 shows much higher thermal resistance than Case 2 and Case 4.

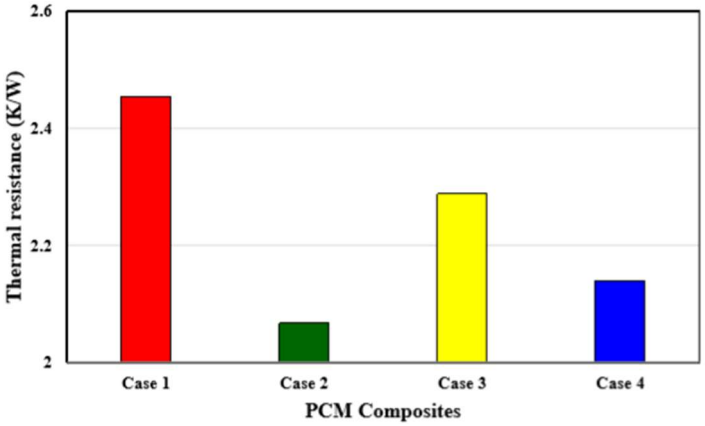

Figure 6. Thermal resistance for 8 W heat input.

3.5. Temperature variations without PCM

Battery temperature variations and the maximum temperature difference without PCM are discussed in this section. The battery temperature can be limited within a desired range using PCM composites. **Figure 7** shows the battery temperature variation for different heat inputs without PCM. For 4 W, 6 W, 8 W, and 10 W, the heat input temperatures reached at 4800 s were 118 °C, 152 °C, 180 °C and 212 °C respectively. **Table 3** shows the battery temperatures at 4800 s with PCM composites and without PCM. The effectiveness of the PCM composites in the temperature control of the battery

can be directly determined from the values in **Table 3**. The PCM composite reduces the battery temperature by around 60% to 70% at various power levels.

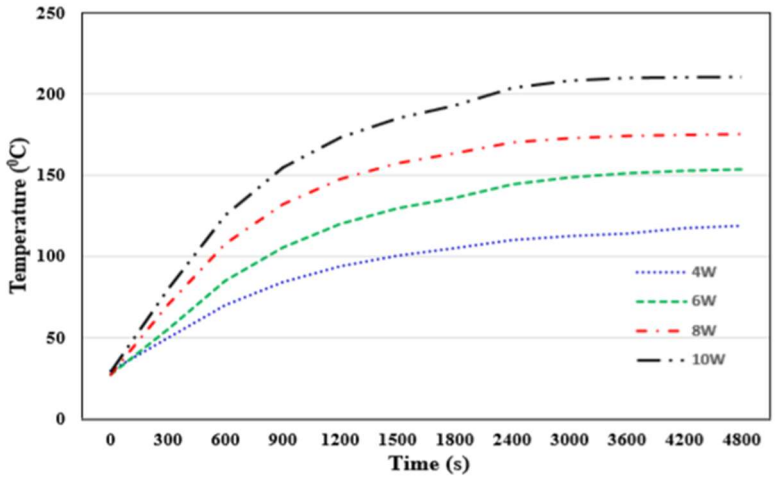

Figure 7. Battery temperature variation without PCM.

Table 3. Battery temperatures at 4800 s with PCM composites and without PCM.

Sl No	Power(W)	PCM composite	Without PCM
1	4	46 ℃	118 ℃
2	6	52 ℃	152 ℃
3	8	61 ℃	180 ℃
4	10	68 ℃	212 ℃

4. Conclusions

The present work comprises experimental investigations of the thermal behaviour of a composite structure thermal management system. The following parameters were analysed:

- Varying heat inputs (4 to 10 W in steps of 2 W).
- Varying nanoparticle weight percentages in the PCM (0.50 wt%, 0.70 wt%, and 0.90 wt% of PCM).

The nano-based phase change material composite structure was studied by examining the representative time points, effects of heat input, and different weight percentages of nanoparticle PCM composites. To control the temperature and maintain temperature uniformity inside the BTMS system, the temperature difference between the battery and cooling medium was decreased. The different trends and results from the analysis are discussed below.

- Battery temperature evolution was studied for various heat inputs, revealing optimal performance with a 4 W heat input in case 4.
- Case 2 consistently demonstrated lower battery temperatures than other nano-based PCM composite structures and the pure PCM case for heat inputs of 6 W, 8 W, and 10 W. Even at a high heat input of 10 W, case 2 limited the temperature below 70 ℃.

- Nanoparticle PCM composites consistently exhibited lower battery temperatures than the pure PCM case across all power levels, attributed to increased thermal conductivity from the addition of nanoparticles.
- Instantaneous Nusselt number analysis indicated that case 2 outperformed other composites at heat inputs of 6 W, 8 W, and 10 W, with a 20% increase compared to other cases. Improved Nusselt numbers signify enhanced heat transfer within the cooling medium due to nanoparticle addition to paraffin.
- The superior Nusselt number in case 2 contributed to an improved temperature distribution in the BTMS.
- Nano-based PCM composites consistently demonstrated lower temperature differences between the battery and cooling medium for all heat inputs, indicating a more uniform temperature distribution within the BTMS. Pure PCM exhibited higher temperature differences due to its lower thermal conductivity.
- Case 2 exhibited the least temperature difference between the battery and PCM medium for all heat inputs, limiting the difference to 50 ℃ compared to other cases.
- Thermal resistance in the cooling medium, affecting heat transfer, was reduced by the addition of nanoparticles, resulting in lower thermal resistance for PCM composite structures compared to the pure PCM case. Case 2 had the lowest thermal resistance, decreasing by 25% compared to other cases.
- In comparison to a case without PCM, the nano-based PCM composite structure demonstrated a remarkable reduction in battery temperature by up to 70%.
- The maximum temperature difference between the battery and cooling medium decreased significantly, reaching a reduction of up to 37 ℃. These findings underscore the efficacy of battery thermal management through the utilization of nano-based PCM composite structures.

To summarize the experimental investigations, the Case 2 nano-PCM composite structure has better battery temperature reduction, improved heat transfer within the medium, lower thermal resistance, and faster battery cooling. Thermal resistance in this case was found to be the lowest, and a reduction of 25% was observed when compared with case 1. Nusselt number enhancement of 20% was also observed in case 2. The temperature difference between the battery and cooling medium obtained for case 2 was a maximum 5 ℃ and we cooled down the battery below 40 ℃ within 200 s for 4 W heat input.

Author contributions: Conceptualization, VM and AB; methodology, VM; software, VM; validation, VM, AB and RB; investigation, VM; resources, VM; data curation, VM; writing—original draft preparation, VM; writing—review and editing, AB and RB; visualization, VM; supervision, AB and RB; project administration, AB and RB. All authors have read and agreed to the published version of the manuscript.

Conflict of interest: The authors declare no conflict of interest.

Nomenclature

A_b	Surface area through which heat is transferred
BTMS	Battery thermal management systems

CPCM	Composites phase change material
DCM-PCMP	Double copper mesh-phase change material plate
K_f	Thermal conductivity of the fluid
LIB	Lithium-ion battery
Nu	Nusselt number
PCM	Phase change material
Q	Heat input
R_{cm}	Overall thermal resistance
T_b	Bulk temperature of the fluid
T_c	Thermal control point
T_m	Maximum melting temperature of PCM
TMS	Thermal management system
T_w	Wall temperature of the surface
w	Width of the surface through which heat is transferred

References

1. Khlissa F, Mhadhbi M, Aich W, et al. Recent Advances in Nanoencapsulated and Nano-Enhanced Phase-Change Materials for Thermal Energy Storage: A Review. Processes. 2023; 11(11): 3219. doi: 10.3390/pr11113219
2. Arshad A, Ali HM, Yan WM, et al. An experimental study of enhanced heat sinks for thermal management using n-eicosane as phase change material. Applied Thermal Engineering. 2018; 132: 52-66. doi: 10.1016/j.applthermaleng.2017.12.066
3. Wang Z, Zhang H, Xia X. Experimental investigation on the thermal behavior of cylindrical battery with composite paraffin and fin structure. International Journal of Heat and Mass Transfer. 2017; 109: 958-970. doi: 10.1016/j.ijheatmasstransfer.2017.02.057
4. Hussain A, Abidi IH, Tso CY, et al. Thermal management of lithium ion batteries using graphene coated nickel foam saturated with phase change materials. International Journal of Thermal Sciences. 2018; 124: 23-35. doi: 10.1016/j.ijthermalsci.2017.09.019
5. Babapoor A, Azizi M, Karimi G. Thermal management of a Li-ion battery using carbon fiber-PCM composites. Applied Thermal Engineering. 2015; 82: 281-290. doi: 10.1016/j.applthermaleng.2015.02.068
6. Situ W, Zhang G, Li X, et al. A thermal management system for rectangular LiFePO4 battery module using novel double copper mesh-enhanced phase change material plates. Energy. 2017; 141: 613-623. doi: 10.1016/j.energy.2017.09.083
7. Karimi G, Azizi M, Babapoor A. Experimental study of a cylindrical lithium ion battery thermal management using phase change material composites. Journal of Energy Storage. 2016; 8: 168-174. doi: 10.1016/j.est.2016.08.005
8. Pan M, Lai W. Cutting copper fiber/paraffin composite phase change material discharging experimental study based on heat dissipation capability of Li-ion battery. Renewable Energy. 2017; 114: 408-422. doi: 10.1016/j.renene.2017.07.004
9. Wang Z, Zhang Z, Jia L, et al. Paraffin and paraffin/aluminum foam composite phase change material heat storage experimental study based on thermal management of Li-ion battery. Applied Thermal Engineering. 2015; 78: 428-436. doi: 10.1016/j.applthermaleng.2015.01.009
10. Ling Z, Wen X, Zhang Z, et al. Thermal management performance of phase change materials with different thermal conductivities for Li-ion battery packs operated at low temperatures. Energy. 2018; 144: 977-983. doi: 10.1016/j.energy.2017.12.098
11. Hussain A, Tso CY, Chao CYH. Experimental investigation of a passive thermal management system for high-powered lithium ion batteries using nickel foam-paraffin composite. Energy. 2016; 115: 209-218. doi: 10.1016/j.energy.2016.09.008
12. Bai F, Chen M, Song W, et al. Thermal management performances of PCM/water cooling-plate using for lithium-ion battery module based on non-uniform internal heat source. Applied Thermal Engineering. 2017; 126: 17-27. doi: 10.1016/j.applthermaleng.2017.07.141

13. Rao Z, Qian Z, Kuang Y, et al. Thermal performance of liquid cooling based thermal management system for cylindrical lithium-ion battery module with variable contact surface. Applied Thermal Engineering. 2017; 123: 1514-1522. doi: 10.1016/j.applthermaleng.2017.06.059
14. Wu W, Wu W, Wang S. Thermal optimization of composite PCM based large-format lithium-ion battery modules under extreme operating conditions. Energy Conversion and Management. 2017; 153: 22-33. doi: 10.1016/j.enconman.2017.09.068
15. Alipanah M, Li X. Numerical studies of lithium-ion battery thermal management systems using phase change materials and metal foams. International Journal of Heat and Mass Transfer. 2016; 102: 1159-1168. doi: 10.1016/j.ijheatmasstransfer.2016.07.010
16. Jiang G, Huang J, Liu M, et al. Experiment and simulation of thermal management for a tube-shell Li-ion battery pack with composite phase change material. Applied Thermal Engineering. 2017; 120: 1-9. doi: 10.1016/j.applthermaleng.2017.03.107
17. Zhao R, Gu J, Liu J. Optimization of a phase change material based internal cooling system for cylindrical Li-ion battery pack and a hybrid cooling design. Energy. 2017; 135: 811-822. doi: 10.1016/j.energy.2017.06.168
18. Lazrak A, Fourmigué JF, Robin JF. An innovative practical battery thermal management system based on phase change materials: Numerical and experimental investigations. Applied Thermal Engineering. 2018; 128: 20-32. doi: 10.1016/j.applthermaleng.2017.08.172
19. Babu Sanker S, Baby R. Phase change material based thermal management of lithium ion batteries: A review on thermal performance of various thermal conductivity enhancers. Journal of Energy Storage. 2022; 50: 104606. doi: 10.1016/j.est.2022.104606
20. Liu C, Wu Y, Li D, et al. Investigation of thermal and optical performance of a phase change material–filled double-glazing unit. Journal of Building Physics. 2017; 42(2): 99-119. doi: 10.1177/1744259117708734
21. Li D, Li Z, Zheng Y, et al. Thermal performance of a PCM-filled double-glazing unit with different thermophysical parameters of PCM. Solar Energy. 2016; 133: 207-220. doi: 10.1016/j.solener.2016.03.039
22. Salih SM, Alsabery AI, Hussein AK, et al. Melting control of phase change material of semi-cylinders inside a horizontal baffled channel: Convective laminar fluid–structure interaction. Journal of Energy Storage. 2023; 58: 106312. doi: 10.1016/j.est.2022.106312
23. Chen H, Abidi A, Hussein AK, et al. Investigation of the use of extended surfaces in paraffin wax phase change material in thermal management of a cylindrical lithium-ion battery: Applicable in the aerospace industry. Journal of Energy Storage. 2022; 45: 103685. doi: 10.1016/j.est.2021.103685
24. Ruhani B, Abidi A, Hussein AK, et al. Numerical simulation of the effect of battery distance and inlet and outlet length on the cooling of cylindrical lithium-ion batteries and overall performance of thermal management system. Journal of Energy Storage. 2022; 45: 103714. doi: 10.1016/j.est.2021.103714
25. Rashid FL, Al-Obaidi MA, Dhaidan NS, et al. Bio-based phase change materials for thermal energy storage and release: A review. Journal of Energy Storage. 2023; 73: 109219. doi: 10.1016/j.est.2023.109219
26. Kolsi L, Hussein AK, Hassen W, et al. Numerical Study of a Phase Change Material Energy Storage Tank Working with Carbon Nanotube–Water Nanofluid under Ha'il City Climatic Conditions. Mathematics. 2023; 11(4): 1057. doi: 10.3390/math11041057
27. Radhakrishnan N, Thomas S, Sobhan CB. Characterization of thermophysical properties of nano-enhanced organic phase change materials using T-history method. Journal of Thermal Analysis and Calorimetry. 2019; 140(5): 2471-2484. doi: 10.1007/s10973-019-08976-1
28. Kothari R, Sahu SK, Kundalwal SI. Investigation on thermal characteristics of nano enhanced phase change material based finned and unfinned heat sinks for thermal management system. Chemical Engineering and Processing - Process Intensification. 2021; 162: 108328. doi: 10.1016/j.cep.2021.108328

Energy Storage and Conversion 2024, 2(2), 1321.
https://doi.org/10.59400/esc.v2i2.1321

Article

Investigation of self-excited induction generator for supporting domestic loads and its extension to a microgrid

Arunava Chatterjee

Electrical Engineering Department, Raghunathpur Government Polytechnic, Purulia 723121, India; arunava7.ju@gmail.com

CITATION

Chatterjee A. Investigation of self-excited induction generator for supporting domestic loads and its extension to a microgrid. Energy Storage and Conversion. 2024; 2(2): 1321. https://doi.org/10.59400/esc.v2i2.1321

ARTICLE INFO

Received: 2 April 2024
Accepted: 13 May 2024
Available online: 2 June 2024

Abstract: This study provides a technical and financial analysis for the incorporation of a microgrid structure with a wind energy conversion system for producing electricity. This study's primary aim is to provide solutions for issues that arise when isolated induction generators are employed with microgrids. A closed-loop smart electronic load controller is used to regulate the loads in the system that are supplied by the generator. A switched variable capacitor bank is used to supply reactive power initially during a voltage dip at varying winds and loads to sustain the voltage profile. Additionally, a simple voltage control loop-based controller for the generator-side converter maintains the voltage at a steady level. Using HOMER software, an economic study of the suggested wind-based microgrid structure is also presented. A laboratory experimental setup is used to support the MATLAB/Simulink study of the proposed method and its control. The findings support the feasibility of implementing the suggested plan in grid-isolated regions for supplying critical loads.

Keywords: induction generator; microgrid; smart electronic load controller; voltage regulation; wind power

1. Introduction

Nowadays, the mainstream of the energy used to generate electricity comes from the burning of fossil fuels like coal, oil, and natural gas. These fossil fuels have finite stocks, and burning them releases a significant amount of toxic gases into the atmosphere. Therefore, finding clean and sustainable sources of energy is always necessary. Wind is a pure and limitless renewable energy source. There are several ways to transform wind energy into electrical form, but using a wind turbine is by far the most common method [1]. In theory, any sort of generator may be installed atop a wind turbine to produce electricity. Even if the generator only produces direct current or alternating current with variable amplitude and frequency, the requirement for grid-compatible electric current may currently be satisfied by connecting appropriate converters.

With its robustness, minimal maintenance requirements, and easy controls, the induction generator (IG) seems to be an excellent option for these applications [2]. IG is preferred for producing wind energy due to its ease of use, dependability, and compact size per generated kilowatt. Moreover, IGs do not require an external power source to produce the excitation magnetic field. They can therefore be applied in far-off [3] and grid-isolated isolated locations [4]. The main limitations of IGs, however, are reactive power consumption and poor voltage regulation at variable speeds, although the invention of static power converters has made it easier to regulate the output voltage of IGs [5].

Because it does not require an external power source to generate the magnetic field, the self-excited induction generator (SEIG) is an excellent choice for wind-driven electric generation applications, particularly for variable wind speeds and isolated places. Although the SEIG scheme was discovered more than 80 years ago, a significant number of research publications have only recently become increasingly focused on the examination [6] and uses of SEIGs [7]. This is because voltage and frequency control techniques have advanced and because the development of renewable energy sources has received enormous global attention over the past thirty years.

The SEIG system's inability to regulate voltage and frequency under variable load situations is its primary operating issue. The machine excitation is immediately impacted by a change in the load impedance. This is because both the induction machine acting as a generator and the load impedance share the excitation capacitors' reactive power. As a result, when the load impedance is increased, the generator's voltage lowers, leading to poor voltage control. On the other hand, even though the speed of the prime mover is constant, the slip of the induction generator rises with increasing load, resulting in a frequency that depends on the load. Many studies have been conducted in the past to regulate the voltage and frequency of a SEIG system operating with variable loads. A high-cost speed governor is generally used as a conventional SEIG controller. A sliding mode controller was proposed, showing controlled dynamic response and behavior of the system upon changes in generator parameters and load [8]. Regulating the voltage and frequency of a SEIG under varying load conditions by an electronic load controller (ELC) was examined [9]. With the adoption of static converters, the voltage regulation problem is somewhat resolved [10], although the system cost has increased to a considerable extent [11]. Often, maximum power point tracking (MPPT)-based control techniques are adopted. Although various MPPT approaches make it easier to operate [12], especially in grid-connected generation [13], standalone grid-secluded generation is frequently controlled without MPPT to reduce the system complexity [14]. However, maintaining a constant generation becomes crucial since independent generations are frequently employed to handle important loads [15]. Hybrid energy storage-based microgrids with modified controls were recently studied for wind power generation [16]. The use of SEIG under unbalanced conditions has also been studied for power generation [17]. This method, although cheap, requires derating the machine, and thus IG operates with reduced capacity. Recent research for wind based renewable power generation focuses on control based on electric springs for flexible voltage control and wind power integration at the expense of cost and complexity [18,19]. Lowering the cost of electric spring-based microgrids is also attempted in the study of Mohanty et al. [20]. Although sometimes it is difficult to effectively regulate voltage for SEIGs without increasing the system cost and complexity.

This research includes a technical and economic analysis of the IG system when feeding varying domestic loads in an effort to aid in the resolution of the aforementioned operational issues with SEIGs. A dynamic capacitor-based voltage regulation scheme is proposed in the planned study, which is shown to be promising in providing variable reactive power initially during load and speed transients. A smart electronic load controller (SELC) is also proposed for load control, which is unique.

The transient response is observed to be better using a simple voltage loop-based converter control for the IG. The IG can then be connected to other renewable generating sources for providing continuous power to grid-isolated loads.

2. System description

The proposed generation system consists of a three-phase induction machine that is connected to a wind turbine for generation purposes. The IG is connected to a bus where system loads can also be connected for supply. To supply the initial reactive power, the stator windings of the induction machine are linked to a capacitor bank. The initial excitation is calculated from reactive power balancing [21]. For augmenting and supporting generation, the IG system can also be connected to a standby PV panel. A storage battery is also connected via a charge controller to support the loads during lean generation periods. The overall connected system is shown in **Figure 1**.

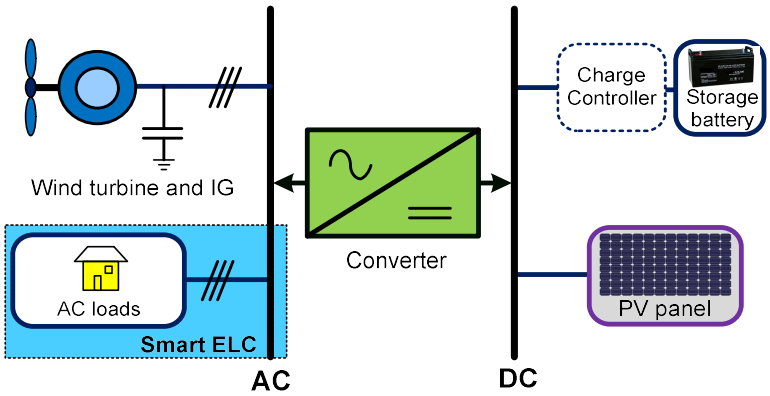

Figure 1. Block diagram of the wind-PV hybrid generation system.

The proposed system is envisioned to be used in a grid-isolated location in an onshore eastern Indian location. The location is not connected to a grid, and hence the utility of the proposed scheme of generation is of prime importance in supplying power to the remotely connected loads.

3. Proposed control scheme

The proposed system generation is provided using the IG. With the IG, a photovoltaic (PV) panel may also be connected. For the control, the microgrid structure with PV panels is not considered. The control is mainly focused on the IG side control of the smart electronic load controller (SELC) and the capacitor bank control with variable wind speeds and variable loads. The control scheme is shown in **Figure 2**. The SELC consists of an ESP-based Wi-Fi-enabled controller that can turn ON/OFF consumer loads based on the generated voltage and load requirements. This is done with the help of relay control, which is obtained using commands to be provided by the operator using the ESP board and a visual dashboard. The entire communication established with the load is done using the Internet of Things (IoT). Any communication protocol may be used, such as the popular message queuing telemetry transport (MQTT) [22] or data distribution system as in the study of

Chatterjee et al. [23]. Here, MQTT is used as it is lightweight and flexible for such control [24].

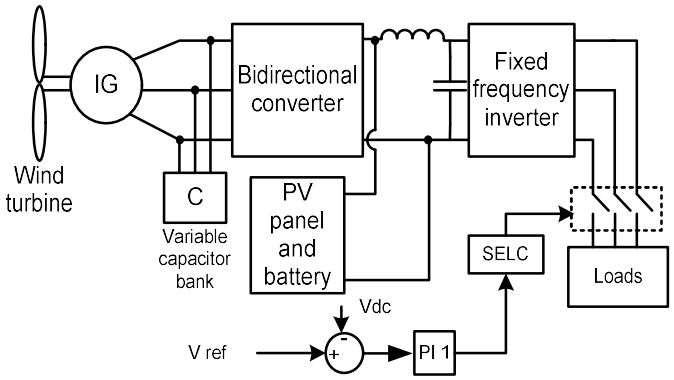

Figure 2. Block diagram of the control scheme for IG with loads.

For the proposed automatic load control, the DC bus voltage is sensed using a voltage sensor. The reference is compared, and the set error is sent to a proportional-integral controller (PI1). The output from the PI1 is taken as the reference data for sending it to SELC. The variable capacitors are controlled by load and speed parameters according to necessity. The SELC consists of an ESP8266-based controller. The operator is thus in a position to control the loads automatically using the sensed voltage data or can decide to turn ON/OFF loads as per requirement using the SELC controller.

4. Connection with microgrid

The IG-based generation system is to be connected with a microgrid, and its cost will also have to be estimated. The cost estimation and optimization are done using "HOMER" software [25]. HOMER Energy is the global standard for optimizing microgrid design in all sectors, from village power and island utilities to grid-connected campuses and military bases. Originally developed at the National Renewable Energy Laboratory and enhanced and distributed by HOMER Energy, HOMER (Hybrid Optimization Model for Multiple Energy Resources) nests three powerful tools in one software product, so that engineering and economics work side by side. HOMER is used because it can simplify and compare hundreds of alternatives to optimization in a single run. This also enables us to observe the effects of external factors, including wind speed and insolation, and comprehend the effect of fluctuations in the ideal system.

For the online microgrid simulation, some elements are used. The elements are an IG-based wind generator, a primary load, a converter, a battery, and a PV panel. There are two buses used. PV cells should be connected to a DC bus only. It is used only when the wind power is not enough to start the generator. A battery is also used there, with the DC bus as the backup source of power. The generator is connected to the AC bus only since it is an IG. A primary load is connected to an AC bus. The system simulation model is shown in **Figure 3**.

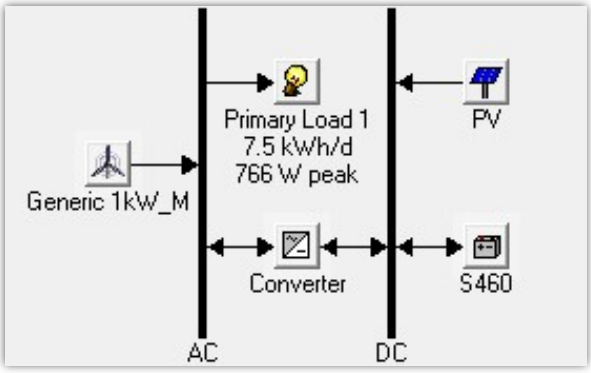

Figure 3. Simulation model of the proposed system.

The converter here is connected to both the AC and DC buses, as shown in **Figure 3**. After the connection is done, the results can be calculated and optimized with different numbers of iterations. The solar and wind data are obtained for the proposed place for setup using the NREL laboratory, as shown in **Figure 4**.

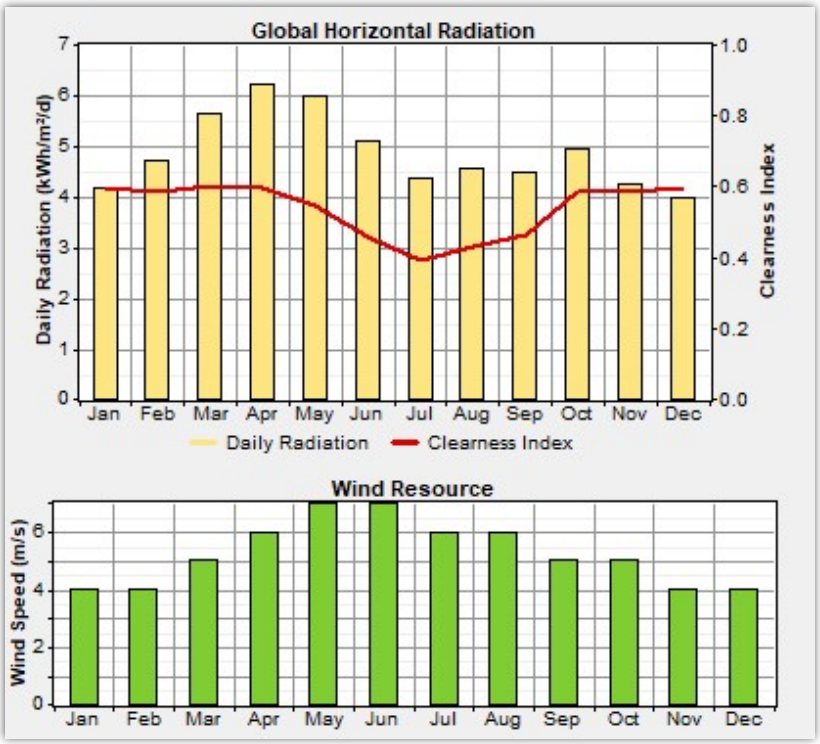

Figure 4. Solar radiation data and wind speed data variation for different months in a year for the installed place.

The PV module is employed when the availability of wind power is low, although it always remains connected to the system and surplus energy is stored in the battery. So, the PV module can supply loads in such cases. Whenever the wind power is low, the PV module provides the power, and whenever the PV module's power is low, the wind generates the power, as seen in **Figure 4**. It is concluded that the two powers complement each other for the proposed place of setup. The HOMER is used mainly to provide economic analysis along with technological support analysis. Therefore,

using the software, the tabulated optimized cost output is shown in **Table 1**.

Table 1. Analysis of the proposed microgrid system with SEIG and PV support.

Initial capital ($)	Net present cost ($)	Operating cost ($/year)	Cost of energy ($/kwh)	Renewable fraction
4580	5350	105	0.158	1.00

The different optimized costs are assessed using the HOMER software when provided with the initial cost of the system components. These costs are verified using a market survey. With the 1 kW IG for the setup, two 500W-peak polycrystalline silicon PV panels are used. Both panels have a voltage rating of 48 V. Deep-cycle lead acid storage batteries with ratings of 12 V and 150 Ah of four numbers in series with overcharge/discharge protection are used for the connected system. The peak load is 760 W. The batteries offer a two-hour backup. The 22-A charge controller is used for charging purposes. The turbine-generator system costs about $3000, and replacing it will set you back $2500. Annually, the cost of operation and maintenance is estimated to be 2% of the original cost. The turbine is erected at a hub height of 10 m. The simulation uses a PV panel rated for 1 kW-peak, 48 V, with a capital cost of $1000 and 2% of the initial cost reserved for annual maintenance. The converter is rated at 1 kW, costs $300 in original capital, and requires $200 in replacement with zero maintenance annually. The battery costs $100 in capital when purchased, and it costs $50 to replace. Watering the battery is mostly covered by the $5 yearly operation and maintenance fee. The table provides the initial capital requirement after discounts, the net present cost of the system, and the operating cost of running such a system in a year. The different cost parameters are simulated and optimized in HOMER. To calculate the Net Present Cost (*NPC*) of the system, the discounted costs are typically deducted from the present values of the various power sources. Thus,

$$NPC = C_i + C_o + C_r - (C_e + C_s) \tag{1}$$

C_o is the system operation and maintenance cost, C_i is the initial system cost, C_r is the cost of system replacement, C_e and C_s are the sold surplus electricity cost and the salvaging cost of equipment at the end of total project life. The C_e value is calculated per hour and it is dependent on the load demand and power generated from the system. The value of C_r is calculated from the studies of Chatterjee and Banerjee [26], Dufo-López et al. [27] as,

$$C_r = \sum_{i=1}^{j} C_{r_k} \frac{(1+g_k)^{ij_k}}{(1+I_r)^{ij_k}} \tag{2}$$

where, C_{r_k} is cost of the replaced component, g_k is inflation rate and I_r is the rate of interest and j_k is total lifetime of k-th component. The value of C_s can be given as,

$$C_s = C_{r_k} \frac{R_c - (R_p - R_r)}{R_c} \tag{3}$$

where, R_c, R_p and R_r are respectively the individual component life, total project life and duration of replacement cost calculation. The cost of operation per year is the summation of running costs and other expenses which essentially exclude the initial cost of the system. The initial system cost C_i is given as,

$$C_i = C_{\text{wtg}}P_{\text{wtg}} + C_{\text{pv}}P_{\text{pv}} + C_{\text{cnv}}P_{\text{cnv}} + C_{\text{bat}}P_{\text{bat}} + C_cP_c \tag{4}$$

where C denotes unit cost and P denotes the nominal power of the sources of the wind turbine generator, PV panel, converters, and batteries, respectively. The C_c denotes the unit cost of the controller, and its nominal power is denoted as P_c which can be neglected. The various equations show that the *NPC* is a variable that may be tuned to reduce the overall cost of the system. The HOMER is used to do this task. The cost of energy (*COE*) is another metric that establishes the optimal net present cost. The ratio of the yearly cost of electricity production to the total electric load provided is used to determine this number. It is defined as,

$$COE = \frac{C_a}{E_s} \tag{5}$$

where total annualized cost of the proposed system is given as C_a (\$/yr) and the total load in terms of energy served is denoted as E_s (kWh/yr). It may be roughly understood as the *NPC* to total load supplied ratio.

It is estimated that the system is going to be used for a period of 25 years. By this time, the net present cost of the system can be mostly salvaged. The cost of generation from fossil fuels is around \$0.120 per kWh [28] to \$0.140 per kWh [29], which is also comparable with full renewable energy generation in the present case.

The cost of production of one unit of energy for such a system is shown to be lower, which is a definite advantage. Such a system, when connected to the grid, can thus supply power at a very cheap rate.

5. Results and discussion

The hardware implementation of the project is done in two parts. Firstly, the simulation results are tested using MATLAB/Simulink. It uses the preset models of the three-phase induction machine and other components. The IG model is considered to have a stationary reference frame and have the same parameters as the experimental machine. The hardware implementation is tested using a laboratory prototype. Secondly, a smart electronic load controller is designed for the proposed IG hardware setup.

The 3-phase induction machine operated as a generator is rated at 2 kW, 415 V, 50 Hz, and is wound for 4 stator poles. The machine parameters are provided in Appendix. The voltage generation initiates at a speed of 1150 rpm at no load without the proposed control (**Figure 2**). Although the speed is low for generation, the capacitor used reduces the operating point of the IG, and thus generation initiates at a lower speed. However, the generated voltage frequency at this speed is lower than 50 Hz. As the generator reaches a steady state, terminal loads across the main windings of the generator can be connected. The experimental setup, as shown in **Figure 5,** uses an induction machine coupled with a DC machine. The DC machine acts as a prime mover. The DC machine can be used to emulate wind turbine characteristics with some modifications. The generator-side bidirectional converter is controlled using a simple voltage loop-based proportional-integral (PI) controller. This controller is responsible for providing stable voltage output with load and speed transients. The voltage reference is taken as a dynamic function of the available wind speed (ω_r), which is compared with the generated voltage. The error is fed to the PI controller. The output of the PI controller is the current reference, which is used to generate pulses for the

converter using hysteresis band-based control to sense the generator current. The PI controller is tuned using the Ziegler-Nichols method. Initially, the integral gain is set to zero, and the proportional gain is increased from zero until sustained oscillations are observed. This gain value and oscillation time are used to set the integral gain for minimal overshoot with judicious settling time. The controller is shown in **Figure 6**. The fixed-frequency inverter is operated at 50 Hz to supply the connected loads.

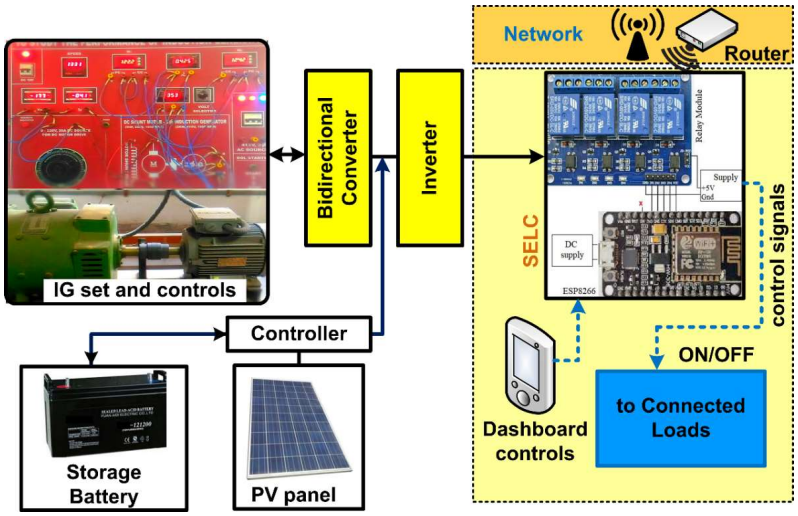

Figure 5. Experimental setup of the IG system with the smart electronic load controller.

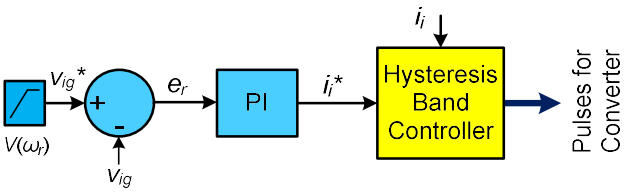

Figure 6. Controller for IG side converter.

However, it is assumed that the prime mover drives the generator at rated speed, considering that some gears may be used in real practice with the wind turbine to generate at rated speed for the IG. It was observed that the mechanical contacts of the laboratory-based experimental IG are competent enough for repeating use. This is due to mechanical wear and tear, and thus an electronic contactor switch was necessary. An ESP8266-controlled relay switch is developed for connecting the variable capacitors and loads. This is done using an electronic relay switch module. The connection of the relay coil for switching loads and capacitances makes the circuit better suited for the different loads and wind speed conditions. At first, the system is simulated using a three-phase induction machine model, which is used as IG in MATLAB/Simulink using a standard stationary frame model [30].

The simulated model has the same ratings as the proposed experimental setup. The proposed control is implemented for the simulated model. The generated voltage profile along with the change in wind speed is shown in **Figure 7**. With the proposed converter control, the voltage regulation is shown to be good with minimal change in voltage when the shaft speed is reduced by 200 r/min. Thus, with speed transients, the voltage is kept stable.

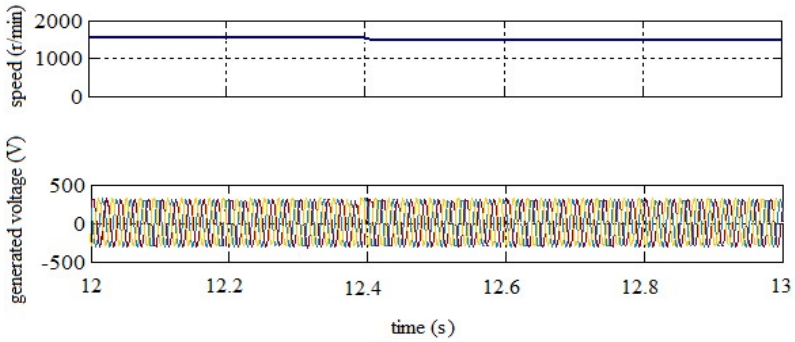

Figure 7. Simulated IG generated voltage with change in speed.

Next, the IG voltage variation with change in load from 1 A to 1.8 A at rated speed is done for the proposed control. It is observed that the generated voltage minimally changes with change in load. The same is shown in **Figure 8**. The load variation is done using the electronic load controller.

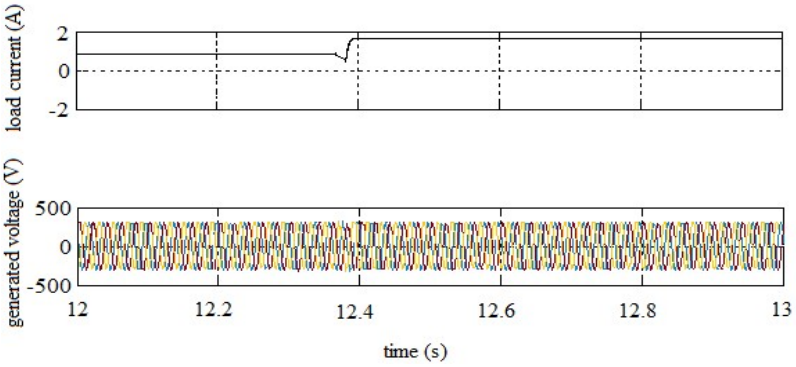

Figure 8. Simulated IG generated voltage with change in load.

The experimental waveforms for the proposed scheme are also shown. The generated voltage profile, along with a similar change in load and wind speed as that of the simulation study, are shown in **Figures 9a** and **9b,** respectively. It is observed that the simulation and experimental results are in good agreement.

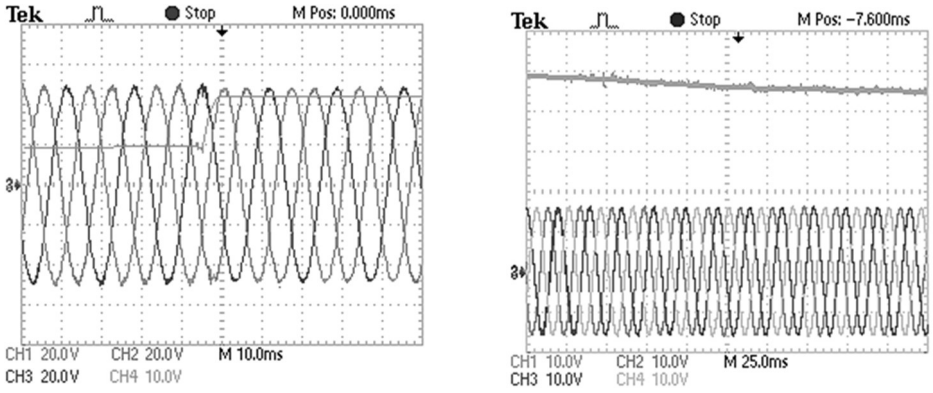

(a) **(b)**

Figure 9. Experimental IG generated voltage with change in **(a)** load (CH1, 2 and 3: *Y*-axis 200 V/div., CH4: *Y*-axis: 1 A/div.); and **(b)** speed (CH1: *Y*-axis: 300 r/min/div., CH2, 3 and 4: *Y*-axis: 200 V/div.).

The electronic load controller switching transients are observed experimentally. With a change in load, the observed waveform is shown in **Figure 10**. It is seen that the controller transients are minimal. The voltage regulation for such a change in load is shown in **Figure 9a**. The observed voltage regulation is better than most conventional control schemes. The load and speed transients are also better. Moreover, the cost and complexity of the scheme are also on the lower side, which are the added advantages.

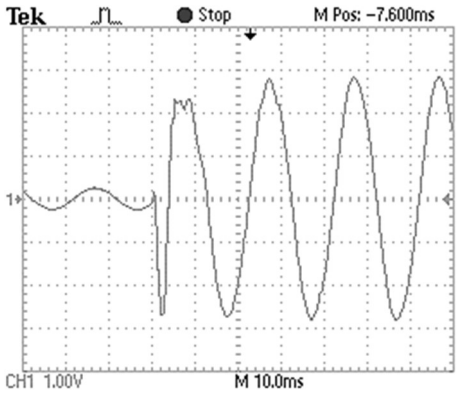

Figure 10. Experimental waveform for change in load in SELC.

6. Conclusion

This research presents a technical and economic analysis of a wind energy conversion system and its integration into a microgrid structure for isolated electricity generation. The modeling is done in HOMER software, which provides the platform to simulate the economic viability of the scheme. The cost of generation obtained is comparable to conventional generation with less system complexity. The bidirectional converter control helps to provide stable voltage with an active voltage control loop. The smart electronic load controller also helps to provide flexible switching of loads with minimal transients for load control.

The characteristics of the SEIG and its proposed control are studied in a MATLAB/Simulink environment and later validated with a laboratory experimental prototype. It is found to be a viable solution for providing power to a remote location. With even proper cost details, the accuracy of the cost optimization can be increased. Moreover, some meta-heuristic or artificial intelligence-based optimization techniques can also be applied for further improved results.

In the future, suitable design procedures with further optimizations for the IG can be implemented. Further, the study of grid integration of the IG with the proposed controller can be a scope of research, and its performance improvement study can also be considered.

Conflict of interest: The author declares no conflict of interest.

References

1. Patel MR, Beik O. Wind and Solar Power Systems, 3rd ed. CRC Press; 2021.
2. Chojaa H. A novel DPC approach for DFIG-based variable speed wind power systems using DSpace. IEEE Access. 2023; 11: 9493-9510. doi: 10.1109/access.2023.3237511

3. Faisal Khan M, Khan M, Iqbal A. Effects of induction machine parameters on its performance as a standalone self-excited induction generator. Energy Reports. 2022; 8: 2302-2313. doi: 10.1016/j.egyr.2022.01.023
4. Grgic I, Basic M, Vukadinovic D, et al. Optimal control of a standalone wind-solar-battery power system with a quasi-z-source inverter. In: Proceedings of the 2020 9th International Conference on Renewable Energy Research and Application (ICRERA); 27-30 September 2020; Glasgow, UK. pp. 61-66. doi: 10.1109/ICRERA49962.2020.9242854
5. Hamid B, Hussain I, Iqbal SJ, et al. Optimal MPPT and BES Control for Grid-Tied DFIG-Based Wind Energy Conversion System. IEEE Transactions on Industry Applications. 2022; 58(6): 7966-7977. doi: 10.1109/tia.2022.3202757
6. Ion CP. A Comprehensive Overview of Single–Phase Self-Excited Induction Generators. IEEE Access. 2020; 8: 197420-197430. doi: 10.1109/access.2020.3034291
7. Chatterjee A, Chatterjee D. PV-assisted microgeneration scheme with single-phase induction generator suitable for wide speed range application. IET Power Electronics. 2017; 10(14): 1859-1869. doi: 10.1049/iet-pel.2016.0535
8. Mi Y, Song Y, Fu Y, et al. The Adaptive Sliding Mode Reactive Power Control Strategy for Wind–Diesel Power System Based on Sliding Mode Observer. IEEE Transactions on Sustainable Energy. 2020; 11(4): 2241-2251. doi: 10.1109/tste.2019.2952142
9. Singh S, Azad ML, Kumar A. Electronic load controllers for self-excited induction generator. In: Proceedings of the 2016 International Conference on Innovation and Challenges in Cyber Security (ICICCS-INBUSH); 3-5 February 2016; Greater Noida, India. pp. 300-303. doi: 10.1109/ICICCS.2016.7542354
10. Chatterjee A. Analysis of a Wind-PV hybrid system with smart control for grid-secluded critical loads in onshore Indian area. In: Bhaumik S, Chattopadhyay S, Chattopadhyay T, Bhattacharya S (editors). Proceedings of International Conference on Industrial Instrumentation and Control (ICI2C 2021); 20-22 August 2021; Kolkata, India. Springer; 2022. pp. 495-503. doi: 10.1007/978-981-16-7011-4_47
11. Chatterjee A. Wind-PV based generation with smart control suitable for grid-isolated critical loads in onshore India. Journal of The Institution of Engineers (India): Series B. 2022; 52: 1-11. doi: 10.1007/s40031-022-00827-2
12. Huynh P, Tungare S, Banerjee A. Maximum Power Point Tracking for Wind Turbine Using Integrated Generator–Rectifier Systems. IEEE Transactions on Power Electronics. 2021; 36(1): 504-512. doi: 10.1109/tpel.2020.3002254
13. Shutari H, Ibrahim T, Mohd Nor NB, et al. Development of a Novel Efficient Maximum Power Extraction Technique for Grid-Tied VSWT System. IEEE Access. 2022; 10: 101922-101935. doi: 10.1109/access.2022.3208583
14. Roy K, Chatterjee A, Chatterjee D, et al. A Photovoltaic-based Improved Excitation Control Strategy of Three-phase Self-excited Induction Generator Suitable for Wind Power Generation. Electric Power Components and Systems. 2015; 43(17): 1912-1920. doi: 10.1080/15325008.2015.1070382
15. Chatterjee A, Ghosh S, Mitra A. Wind-PV based isolated hybrid generation for smart irrigation management and supplying other critical loads. In: Proceedings of the 2022 IEEE 2nd International Conference on Sustainable Energy and Future Electric Transportation (SeFeT); 4-6 August 2022; Hyderabad, India. pp. 1-6. doi: 10.1109/SeFeT55524.2022.9908711
16. Behera PK, Pattnaik M. Coordinated Power Management of a Laboratory Scale Wind Energy Assisted LVDC Microgrid With Hybrid Energy Storage System. IEEE Transactions on Consumer Electronics. 2023; 69(3): 467-477. doi: 10.1109/tce.2023.3287099
17. Liu Y, Masadeh MA, Pillay P. Power-Hardware-In-The-Loop-Based Emulation of a Self-Excited Induction Generator Under Unbalanced Conditions. IEEE Transactions on Industry Applications. 2022; 58(1): 588-598. doi: 10.1109/tia.2021.3118985
18. Panda D, Kundu P, Rajpuroit BS. Real-time voltage control and harmonics elimination of islanded microgrid using back-to-back electric spring. IEEE Transactions on Industry Applications. 2024. doi: 10.1109/TIA.2024.3397963
19. Mohanty S, Pati S, Kar SK, et al. A Novel Electric Spring with Improved Range of Operation for Isolated Microgrid Systems. IEEE Access. 2023; 11: 75761-75781. doi: 10.1109/access.2023.3295888
20. Mohanty S, Pati S, Kumar Kar S. Improved islanded microgrid performance with sliding mode controller based electric spring. Renewable Energy Focus. 2024; 48: 100535. doi: 10.1016/j.ref.2023.100535
21. Trzynadlowski A. Control of Induction Motors, 1st ed. Academic Press; 2001.
22. Ghosh S, Chatterjee A, Chatterjee D. Extraction of statistical features for type-2 fuzzy NILM with IoT enabled control in a smart home. Expert Systems with Applications. 2023; 212: 118750. doi: 10.1016/j.eswa.2022.118750
23. Chatterjee A, Ghosh S, Mitra A. Hybrid generation scheme for delivering irrigation loads and other critical loads with smart IoT based control. IEEE Transactions on Industry Applications. 2024; 60(1): 828-837. doi: 10.1109/TIA.2023.3322114
24. Ganguly B, Chatterjee A. MQTT protocol based extensive smart motor control for electric vehicular application. In:

Proceedings of the 2020 IEEE 7th Uttar Pradesh Section International Conference on Electrical, Electronics and Computer Engineering (UPCON); 27-29 November 2020; Prayagraj, India. pp. 1-5. doi: 10.1109/UPCON50219.2020.9376452
25. Homer Energy. Available online: https://www.homerenergy.com/ (accessed on 17 April 2024).
26. Chatterjee A, Banerjee B. Cost-Effective Hybrid Wind-Photovoltaic Generation System for Isolated Critical Loads: A Case Study. Journal of Electronics and Electrical Engineering. 2023. doi: 10.37256/jeee.2220233735
27. Dufo-López R, Bernal-Agustín JL, Mendoza F. Design and economical analysis of hybrid PV–wind systems connected to the grid for the intermittent production of hydrogen. Energy Policy. 2009; 37(8): 3082-3095. doi: 10.1016/j.enpol.2009.03.059
28. Global Petrol Prices. Available online: https://www.globalpetrolprices.com/India/electricity_prices/ (accessed on 17 April 2024).
29. Strielkowski W. Renewable energy sources, power markets, and smart grids. In: Social Impacts of Smart Grids, 1st ed. Elsevier; 2020. pp. 97-151.
30. Bose BK. Modern Power Electronics and AC Drives, 1st ed. Prentice Hall; 2001.

Appendix

Table A1. Induction machine parameters.

Parameters	**Values per phase**
Stator circuit resistance	6.44 Ω
Rotor circuit resistance	6.57 Ω
Stator and rotor leakage inductance	8.55 mH
Magnetising inductance	276.55 mH
Inertia constant	0.142 kg·m^2

Energy Storage and Conversion 2024, 2(2), 523.
https://doi.org/10.59400/esc.v2i2.523

Review

Research progress on ZnO/MoS_2/rGO ternary photocatalysts

Runlin Zhang[1], Weiwei Yang[2], Qiuyu Chen[3], Zhengyan Du[1,*], Zeshuo Meng[1,*]

[1] Key Laboratory of Automobile Materials of MOE, School of Materials Science and Engineering, Jilin University, Changchun 130012, Jilin, China
[2] No.11 High School of Changchun, Changchun 130062, Jilin, China
[3] School of Public Health, Jilin University, Changchun 130021, Jilin, China
*** Corresponding authors:** Zhengyan Du, zydu21@jlu.edu.cn; Zeshuo Meng, mengzs21@jlu.edu.cn

CITATION

Zhang R, Yang W, Chen Q, et al. Research progress on ZnO/MoS_2/rGO ternary photocatalysts. Energy Storage and Conversion. 2024; 2(2): 523. https://doi.org/10.59400/esc.v2i2.523

ARTICLE INFO

Received: 29 January 2024
Accepted: 11 March 2024
Available online: 11 April 2024

Abstract: Energy shortages and environmental pollution have become one of the important global issues, and semiconductor photocatalytic technology is considered one of the most effective means to solve these problems. As a new and efficient green material, ZnO has attracted wide attention. ZnO is widely used in the field of photocatalysis due to its non-toxicity, low cost, environmental friendliness, adjustable band gap, high electron density, and chemical stability. However, the recombination of photogenerated charge carriers in ZnO hinders its practical application and lowers the utilization efficiency of visible light. On the other hand, molybdenum disulfide/reduced graphene oxide (MoS_2/rGO), as a binary non-precious metal co-catalyst, has a larger specific surface area, suitable band gap width, and visible light response capability compared to a single-phase graphene co-catalyst. Therefore, introducing the MoS_2/rGO co-catalyst into the ZnO system can provide more active sites, reduce the probability of photogenerated charge carrier recombination, and improve the utilization efficiency of visible light. In this review, we summarize the hydrothermal synthesis methods for preparing this highly demanded nanocomposite material, including one-step and stepwise methods. Subsequently, we elaborate on the mechanism of enhancing light absorption and achieving efficient electron-hole separation behavior in the ternary system heterojunction structure during the photocatalytic process. Due to its significant advantages, this ternary system heterojunction structure has been widely applied in the field of photocatalysis, including applications such as pollutant degradation, sterilization, and water splitting.

Keywords: ZnO; MoS_2; graphene; ternary composite materials; photocatalysis

1. Introduction

Since the discovery in 1967 by Fujishima and his colleagues at the University of Tokyo, Japan, that water can be electrolyzed by illuminating a TiO_2 electrode, the application of TiO_2 in the field of photocatalysis has experienced rapid development, and semiconductor photocatalysts have also advanced rapidly as a result [1]. Subsequently, in 1976, Frank and his colleagues successfully applied photocatalytic oxidation technology to the degradation of pollutants in water, achieving breakthrough progress and laying an important theoretical foundation for the application of this technology in wastewater treatment [2]. In 2015, a Japanese company developed a new type of nanophotocatalyst, which is expected to address the increasingly severe water scarcity issue [3]. Since the beginning of the 21st century, energy shortages and environmental pollution have become significant challenges for humanity, with water pollution being particularly prevalent [4]. Therefore, there is an urgent need to explore efficient and clean new energy sources and technologies for treating pollutants. Photocatalysts, as a new and effective green material, have attracted increasing

attention. It is crucial to develop high-performance photocatalysts, with key factors including high light absorption efficiency, a low recombination rate of photo-generated electron-hole pairs, and a large surface area.

In the new generation of photocatalysts, ZnO is widely used in the field of photocatalysis due to its advantages such as non-toxicity, low cost, environmental friendliness, adjustable band gap, high electron density, and chemical stability [5]. Under the illumination of light with energy higher than its band gap, ZnO photocatalysts can undergo photocatalytic reactions, generating strong oxidative radicals and ions, thereby achieving the degradation of organic pollutants [6]. Therefore, ZnO has wide applications in air purification, wastewater treatment, antibacterial materials, and the degradation of organic pollutants. However, ZnO suffers from the recombination of photogenerated charge carriers, resulting in low utilization efficiency of visible light, which hinders the progress of photocatalytic reactions [7]. On the other hand, MoS_2/rGO, as a binary non-precious metal co-catalyst, has a larger specific surface area, a suitable band gap width, and a higher utilization efficiency of visible light compared to simply introducing graphene as a co-catalyst [8]. Therefore, introducing the MoS_2/rGO co-catalyst into the ZnO system can provide more active sites, reduce the recombination probability of photogenerated charge carriers, and enhance the absorption capacity of visible light [9]. ZnO/MoS_2/rGO ternary photocatalyst can effectively improve the solar energy utilization efficiency of semiconductor photocatalysts, and it is one of the important directions to promote the further development of photocatalytic technology (**Figure 1**) [10]. However, there are still some problems and challenges to be solved in the synthesis and application of ternary systems. Firstly, the controlled synthesis of the ternary system is still in the exploratory stage. In hydrothermal synthesis, the various physical and chemical properties of different components make the influencing factors of structure very complicated, which makes it difficult for researchers to control the formation of morphology while maintaining close contact with heterogeneous structures. In addition, hydrothermal reactions and other precise synthesis methods containing more reaction variables and forms remain to be explored. Secondly, there are still some differences in the catalytic activity of the same system used in the photocatalytic hydrogen evolution reaction, so the heterostructure of the ternary system as the excellent activity source of the photocatalyst still needs further study. This requires more advanced in situ characterization and computational simulation to further elucidate the reaction mechanism and theoretical explanation of catalysis. In order to solve these problems and challenges, it is necessary to systematically summarize the ternary system photocatalysts. Therefore, we summarized the recent progress of ternary system heterostructures as photocatalysts, including synthesis, principle, and application, in order to provide some inspiration and guidance for future researchers.

Herein, this review summarizes the hydrothermal synthesis methods for preparing such high-demand nanocomposite materials, including one-step and stepwise methods. Subsequently, we elaborate on the mechanism of how the heterojunction structure of the ternary system enhances light absorption and achieves efficient electron-hole separation behavior during the photocatalytic process. Due to its significant advantages, this heterojunction structure of the ternary system has been

widely applied in the field of photocatalysis, including applications such as pollutant degradation, sterilization, and water splitting. We believe that these studies provide important references for a deeper understanding of the diversity and application potential of ternary composites and open up new possibilities for the development of materials science and energy fields (**Figure 2**).

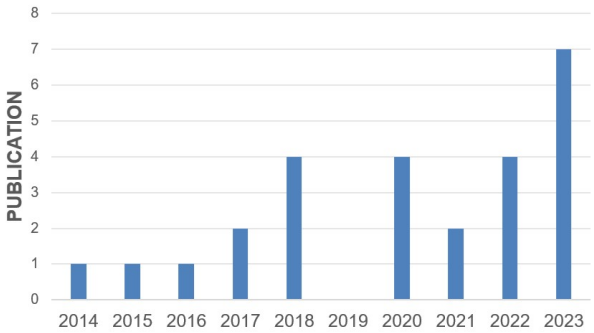

Figure 1. Number of publications ZnO/MoS_2/rGO ternary photocatalysts according to Web of Science (accessed: 7 March 2024).

Figure 2. The comprehensive overview of ZnO/MoS_2/rGO ternary photocatalysts.

2. Synthesis of the ZnO/MoS_2/rGO ternary system

Due to the complexity of ternary systems, it is often necessary to synthesize heterostructure nanocomposite materials with high specific surface areas under harsh conditions. Therefore, hydrothermal and solvothermal methods are the main synthesis methods. Hydrothermal synthesis refers to the method of forming and growing crystals through chemical reactions and changes in the solubility of substances in a closed heating solution at temperatures and pressures higher than ambient conditions [11]. Typically, this high-temperature and high-pressure environment is achieved using a high-pressure autoclave equipped with a polytetrafluoroethylene (PTFE) container. The conditions of hydrothermal synthesis can be precisely controlled by adjusting internal parameters of the system, such as solute concentration and ratio, pH value, time, pressure, additives, or soft/hard templates, as well as external environmental conditions, such as the method of inputting energy [12]. The solvothermal method is a development of hydrothermal synthesis and typically involves the use of non-aqueous organic reaction systems. Ternary systems require close contact between different materials to form heterostructures and achieve smaller particle sizes for obtaining more reaction sites, making the synthesis of composite materials

challenging. Here, we summarize two different hydrothermal synthesis pathways in order to provide guidance for future researchers in their synthesis endeavors.

2.1. One-step hydrothermal method

Due to the uniform heating environment and highly controllable reaction conditions, the hydrothermal method has become an effective approach for synthesizing high-surface-area nanocomposite materials. In this regard, Guan et al. [13] utilized a one-step hydrothermal method to synthesize heterostructures in a ternary system. They dispersed graphene oxide (GO) in distilled water to prepare a GO solution after subjecting it to ultrasonication for 6 h at 500 W. Then, the GO solution, ZnO, $Na_2MoO_4 \cdot 2H_2O$, and thioacetamide were dispersed in distilled water in specific quantities and stirred. Finally, the mixture was heated at 200 ℃ for 24 h in a high-pressure autoclave. The resulting gray precipitate was washed, dried, and annealed at 300 ℃ under a nitrogen atmosphere for 2 h, yielding irregular particles with sizes ranging from 40–400 nm. Additionally, some MoS_2 nanoparticles were uniformly dispersed on the surface (**Figure 3a**). Close contact was formed between ZnO, MoS_2, and reduced graphene oxide (rGO), which facilitated the transfer of electrons from ZnO to RGO and/or MoS_2, thereby delaying the recombination of electron-hole pairs (**Figure 3b**) [13]. Priyadharsan et al. [14], on the other hand, modified the sulfur source and zinc source to reduce the synthesis temperature and complexity of the reaction system. They first prepared a suspension of reduced graphene oxide (rGO) and sonicated it for 1 h to ensure uniform dispersion. Then, Na_2MoO_4, CH_4N_2S, and $Zn(CH_3COO)_2 \cdot 2H_2O$ were added to the solution in specific proportions, followed by stirring the solution and heating it at 160 ℃ for 12 h in a reaction vessel. The resulting sample was washed, dried overnight at 80 ℃, and became a ternary nanocomposite material (MZG). MZG consisted of uniformly distributed wurtzite ZnO, flower-like MoS_2 nanospheres, and wrinkled rGO nanosheets. It can be observed that the metal oxide nanoparticles were adsorbed on both sides of the graphene sheets, resulting in a multilayered structure of graphene (**Figures 3c** and **3d**) [14].

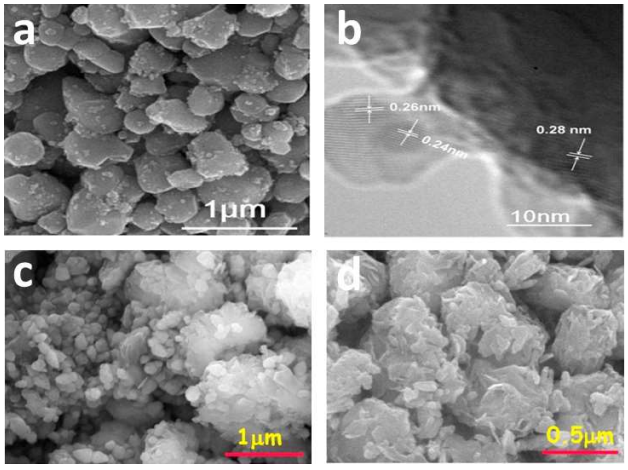

Figure 3. (a) SEM image; **(b)** HRTEM image of 0.75 wt%5G95M/ZnO [13]. SEM images of **(c)** and **(d)** MZG nanocomposites [14].

2.2. Stepwise hydrothermal method

To achieve more precise control over the proportions of different components in the ternary system and reduce the limitations of synthesis conditions, researchers have utilized a stepwise hydrothermal method. This approach involves sequentially synthesizing the co-catalyst and photocatalyst to explore the optimal content of different materials for achieving synergistic effects while ensuring close contact between the heterostructures. Ugur et al. [15] employed a multi-step hydrothermal method to precisely control the proportion of the co-catalyst in the sample, aiming to achieve positive synergistic effects in the ternary system. Firstly, they used $Na_2MoO_4 \cdot 2H_2O$, CH_4N_2S, and graphene oxide (GO) as precursors to synthesize MoS_2-rGO (MG) through hydrothermal synthesis, adjusting the content of rGO to achieve different hybridization effects. Subsequently, the obtained MG composite was dispersed in a 100-mL solution containing 30 mL of ethanol and 70 mL of deionized water, and 300 mg of ZnO dispersed in 100 mL of deionized water was added dropwise. The mixture was stirred for 2 h at room temperature. The resulting mixture was then heated in a high-pressure autoclave at 180 ℃ for 10 h, followed by cooling to room temperature, washing, and drying, resulting in the successful synthesis of the sample (**Figure 4a**) [15]. Kumar et al. [16], on the other hand, used $Na_2MoO_4 \cdot 2H_2O$, GO, and L-cysteine as precursors. The precursors were subjected to a high-pressure autoclave at 180 ℃ for 24 h. The resulting product was washed and dried overnight at 80 ℃ to obtain MoS_2-rGO hybrid. Subsequently, the hybrid material was dispersed in deionized water, and a solution containing $Zn(CH_3COO)_2 \cdot 2H_2O$ and NaOH was added to form a homogeneous solution. The solution was then transferred to a high-pressure autoclave and treated at 160 ℃ for 2 h. After washing and drying, the desired product was obtained. This method allows for the control of the MoS_2-rGO hybrid content to optimize the heterostructure (**Figure 4b**) [16]. Li et al. [17] proposed a microwave-assisted method to synthesize the MoS_2-rGO component in the ternary system. They added varying amounts of GO to a solution of phosphomolybdic acid hydrate and adjusted the pH to 7 using a NaOH solution. Then, they added a thioacetamide solution and stirred for 10 min to generate a homogeneous dispersion. Subsequently, the mixture was heated at 150 ℃ for 10 min under microwave irradiation with a power of 150 W using an automated focusing microwave system. After washing and drying the resulting precipitate, the sample was obtained [17].

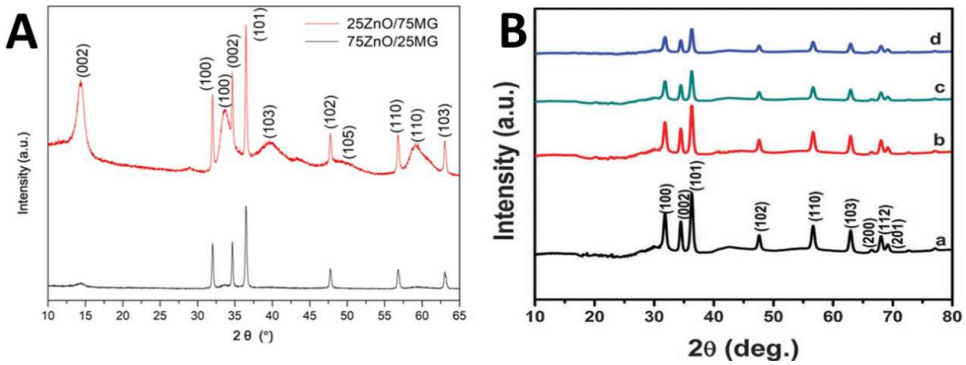

Figure 4. (A) XRD images of ZnO/MG hybrids [15]; **(B)** XRD patterns of a: ZnO NP, b: ZMG0.5, c: ZMG1 and d: ZMG2 [16].

In conclusion, the current synthesis of ternary systems primarily relies on relatively simple hydrothermal methods. However, there is a lack of in-depth exploration and understanding of additional reaction conditions (such as external fields, templates, etc.) and synthesis mechanisms.

3. Photocatalytic applications of ZnO/MoS_2/rGO ternary system

For a long time, the photocatalytic activity of semiconductors has been limited by issues such as low efficiency, narrow light absorption range, and rapid recombination of photogenerated electron-hole pairs [18–20]. Combining wide-bandgap and narrow-bandgap semiconductors to form heterostructures with band offset has been proven to be an effective strategy for improvement [21]. In this research context, researchers have paid significant attention to the heterostructure of a ternary system composed of wide-bandgap ZnO, narrow-bandgap MoS_2, and zero-bandgap graphene with a low Fermi level [22–24]. Due to the difference in the conduction band (CB) positions between ZnO and MoS_2, photogenerated electrons can thermodynamically transfer from ZnO to MoS_2, thereby slowing down the recombination process of electron-hole pairs (**Figure 5**). At the same time, rGO in graphene, with its two-dimensional sp^2-hybridized conjugated structure, exhibits favorable band potential and Fermi-level positions. It can act as an electron reservoir, receiving and transferring electrons from active sites in photocatalytic reactions [25].

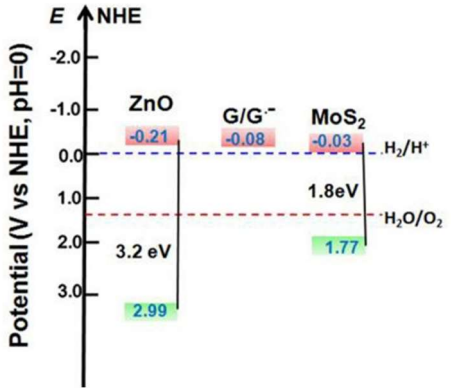

Figure 5. Schematic illustration of the potential and band positions for the ZnO, MoS_2 and rGO [13].

rGO also possesses excellent physicochemical properties, which can alleviate the aggregation issue of MoS_2 and ensure close contact between semiconductors, thus forming a stable heterostructure [26]. Furthermore, some literature suggests that doping MoS_2 and rGO as co-catalysts into ZnO can effectively adjust the band positions of the heterostructure, enhance visible light absorption, and improve overall light absorption capacity. Based on these findings, we have summarized some understanding of the heterostructure of the ternary system in overcoming challenges in semiconductor photocatalysis and outlined the research progress of the ternary system widely applied in photocatalytic hydrogen evolution, pollutant degradation, and antibacterial applications.

As an efficient photocatalyst that is metal-free, non-toxic, and low-cost, ZnO is limited by its wide band gap, which can only be excited by ultraviolet (UV) radiation

[27–29]. However, UV radiation accounts for only about 5% of the solar spectrum, while the visible light region accounts for approximately 43%. This significantly limits the energy utilization efficiency of ZnO [30,31]. Therefore, it is necessary to broaden the light absorption range of ZnO to the visible light region and enhance its light absorption/capturing capability. In this regard, Kumar et al. proposed the ZnO-MoS_2-rGO heterostructure, which enhances light capture in both the UV and visible light regions, thereby generating more photo-induced charge carriers. Through diffuse reflectance spectroscopy (DRS) analysis in the range of 200–800 nm, they found that the light absorption capacity of the heterostructure increases with increasing MoS_2-RGO content (**Figure 6**). This is attributed to the absorption characteristics of MoS_2 in the wavelength range of 200–800 nm, and the synergistic effect of MoS_2-rGO leads to a redshift in the absorption spectrum of the heterostructure, enabling better utilization of the visible light region. For samples with different doping levels, they explained the variation in the bandgap as a result of chemical bonding at specific sites between the semiconductor and GO, leading to charge delocalization and optimizing the optical properties of the heterostructure [16,32].

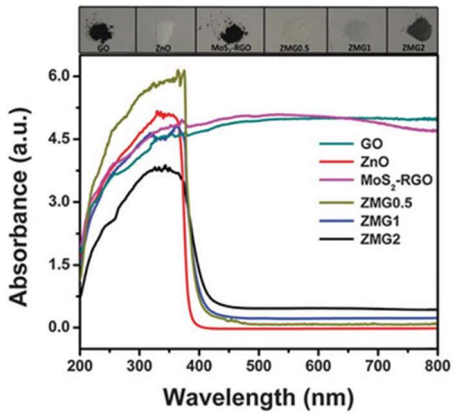

Figure 6. DRS of GO, ZnO NP, MoS_2-RGO, ZMG0.5, ZMG1 and ZMG2 [16].

In semiconductor materials used for photocatalysis, the photogenerated electrons in the CB exist in metastable states and eventually recombine with holes in the VB. The rapid recombination of electron-hole pairs shortens the lifetime of charge carriers, resulting in lower photocatalytic activity [33]. Extending the charge transfer pathway is one effective way to enhance the material's capability for photocarrier separation. Ternary systems composed of semiconductors with different band gaps and rGO demonstrate significant potential in this regard [34]. Regarding the application of MoS_2-rGO/ZnO in photocatalytic hydrogen evolution, Guan et al. proposed the reasons behind the high hydrogen evolution activity of the ternary system, attributing it to the positive synergistic effect between MoS_2 and rGO, where rGO functions as both a co-catalyst for hydrogen evolution and a powerful pathway for electron transfer (**Figure 7a**). Through characterization techniques such as UV-vis absorption spectroscopy (**Figure 7d**), nitrogen adsorption-desorption analysis, photoluminescence (PL) spectroscopy (**Figure 7e**), and photocurrent response measurements (**Figure 7b**), they ruled out other factors influencing the hydrogen evolution activity and demonstrated that rGO accelerates the transfer of electrons from ZnO to MoS_2, improving electron transport. This impedes the recombination of

electron-hole pairs in the material, thereby enhancing the release activity of H_2. Additionally, they proposed a mechanism to explain the hydrogen evolution process in the ternary system and provided insights for the design of other multicomponent photocatalysts [13]. Regarding the photocharge enhancement and charge separation capability in the ternary system, Kumar et al. [16] provided another insight (**Figure 7c**). They noted that in the process of photocatalytic hydrogen evolution, the presence of catalyst dispersed in the electrolyte (S^{2-} and SO_3^{2-}) enhances the hydrogen evolution rate (**Figure 7f**), with the optimal sample exhibiting a performance of 28.616 mmol $h^{-1}g_{cat}^{-1}$ under sunlight irradiation. They attributed this to the in-situ generation of ZnS, which improves the interface charge transfer between the co-catalyst MoS_2 and rGO. Furthermore, rGO provides a large number of active sites available for photocatalytic reactions. Through characterization experiments such as scanning electron microscopy, transmission electron microscopy, X-ray diffraction, and energy-dispersive X-ray spectroscopy, they proved the presence of ZnS and indicated that the generation of ZnS results in extended absorption in the visible light region. Additionally, they suggested that the CB of ZnS has a lower potential than that of ZnO, while the VB of ZnO has a positive potential relative to that of ZnS [35,36]. The more negative CB potential of ZnS allows electrons to transfer from the CB of ZnS to the CB of ZnO, while holes transfer from the VB of ZnO to the VB of ZnS. As a result, the ZnS-ZnO heterostructure facilitates the effective separation of photogenerated charge carriers at the interface. Furthermore, rGO acts as an electron acceptor and shuttle, with its high charge transfer mobility extending the lifetime of photogenerated charge carriers [37].

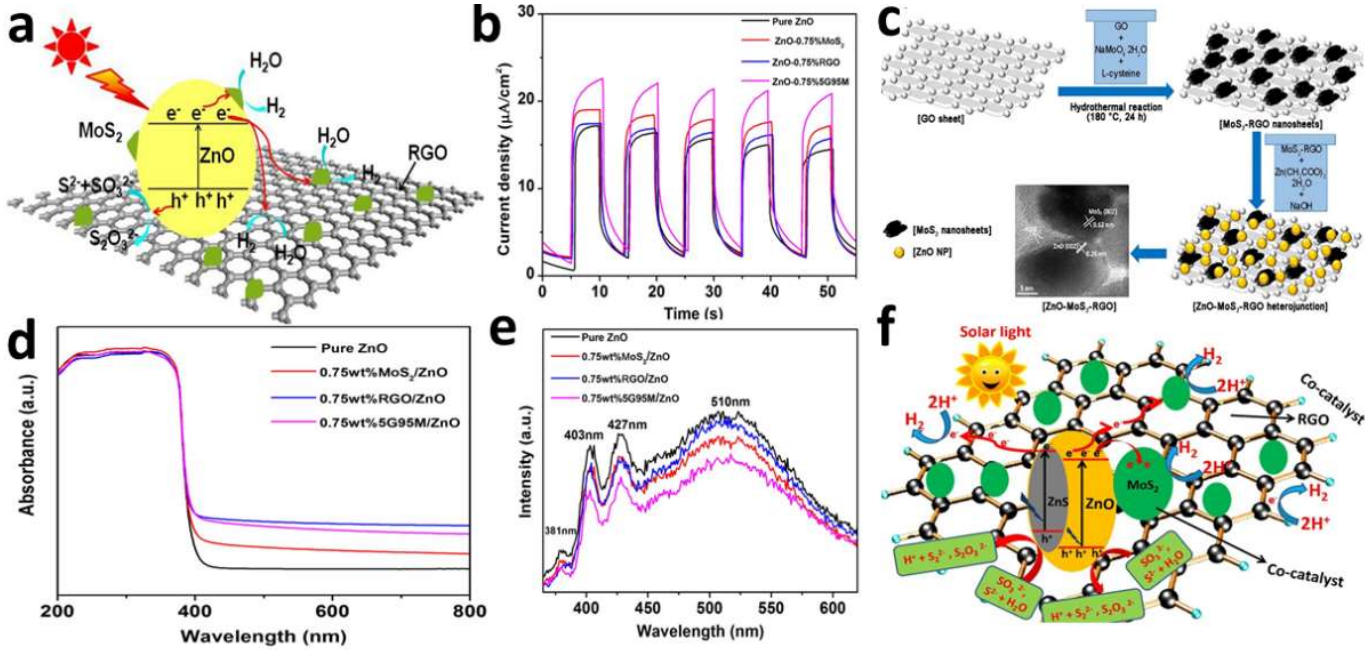

Figure 7. (a) mechanism of H_2 evolution process in the MG/ZnO composite under irradiation; **(b)** transient photocurrent responses; **(c)** scheme of ZnO-MoS_2-rGO ternary nanocomposites; **(d)** UV-vis absorption spectra; **(e)** the PL spectrum of pure ZnO, 0.75 wt% MoS_2/ZnO, 0.75 wt% rGO/ZnO and 0.75 wt% 5G95M/ZnO samples [13]; **(f)** proposed mechanism for enhanced electron transfer across the ZnS-ZnO-MoS_2-rGO hetero-junction under sunlight irradiation for photocatalytic H_2 generation with Na_2S-Na_2SO_3 as a sacrificial reagent [37].

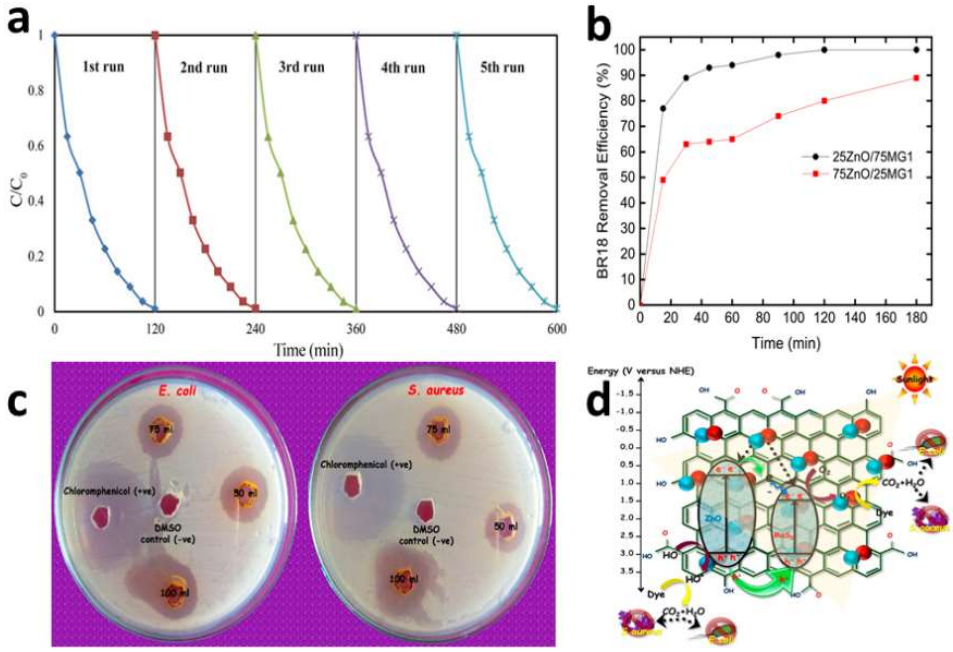

Figure 8. (a) reusability of rGO/ZnO/MoS_2 nanocomposite in optimal condition for degradation process of aniline during the five cycles [38]; **(b)** photocatalytic degradation of BR18 dye for 25ZnO/75MG1 and 75ZnO/25MG1 [15]; **(c)** zone of inhibition tests for WFG nanocomposites materials towards gram-negative *E. coli* bacteria and gram-positive *S. aureus* bacteria; **(d)** photocatalytic mechanism scheme of the MZG nanocomposite [14].

The enhanced light absorption capacity, photocarrier separation ability, and prolonged carrier lifetime greatly expand the application range of ternary systems in photocatalytic applications. Ghasemipour et al. [38] applied rGO/ZnO/MoS_2 ternary nanocomposites to the photocatalytic degradation of aniline in aqueous solutions and investigated the effects of operational variables such as solution pH, catalyst dosage, and initial aniline concentration on achieving maximum degradation efficiency. They found that under conditions of pH = 4, catalyst dosage of 0.7 g L^{-1}, aniline concentration of 80 ppm, and light intensity of 100 W, complete degradation of aniline was observed. Based on the results of scavenger experiments, hydroxyl radicals were identified as the main active species in the photocatalytic reaction. Additionally, due to the synergistic effects between the components in the ternary system, the catalyst exhibited excellent reusability and stability even after five consecutive uses (**Figure 8a**). This study demonstrates the tremendous potential of rGO/ZnO/MoS_2 in treating various organic pollutants in wastewater. Priyadharsan et al. [38] proposed that MoS_2-ZnO-reduced graphene oxide (MZG) nanocomposites exhibit high antibacterial activity against *Escherichia coli* (*E. coli*) and *Staphylococcus aureus* (*S. aureus*) (**Figure 8d**). They investigated the antibacterial activity of MZG nanocomposites against these two pathogenic bacteria using the well diffusion method on Mueller-Hinton agar plates (**Figure 8c**). The results demonstrated that the antibacterial activity of MZG nanocomposites was positively correlated with the dosage. At higher concentrations (100 μg mL^{-1}), bacterial growth was completely inhibited. The bio-deactivation mechanism occurred through the production of abundant surface oxygen, leading to bacterial membrane rupture and ultimately killing the pathogens. This study

highlights the potential application of ternary materials as effective antibacterial agents [14,39]. Ugur et al. [15] synthesized a ternary hybrid nanostructure composed of ZnO nanorods and MG co-catalyst and applied it to the degradation of the water pollutant BR18 dye commonly found in the textile industry. Under the conditions of 25ZnO/75MG1 heterostructure, 100% dye degradation could be achieved within 180 min (**Figure 8b**). When the content of GO in the co-catalyst increased to 5%, 25ZnO/75MG2 achieved complete degradation of the dye solution within the first 30 min. They attributed this excellent photocatalytic performance to the positive synergistic effect of the MoS_2-rGO co-catalyst and highlighted the effective role of GO content in accelerating charge separation and electron transfer characteristics [15].

4. Conclusions

The ZnO/MoS_2/rGO ternary system heterostructure is a highly promising photocatalyst that benefits from the synergistic interaction between the catalyst and co-catalyst. This system exhibits significant advantages in terms of solar light absorption capacity and range, specific surface area, and efficiency of photogenerated electron-hole separation. This review summarizes the hydrothermal synthesis methods for preparing such high-demand nanocomposite materials, including one-step and stepwise methods. Subsequently, we elaborate on the mechanism of how the heterostructure of the ternary system enhances light absorption and achieves efficient electron-hole separation behavior during the photocatalytic process. Due to its tremendous advantages, this ternary system heterostructure has been widely applied in the field of photocatalysis, including applications such as pollutant degradation, sterilization, and water splitting (**Table 1**).

Table 1. Synthesis methods for various heterostructures.

Material	Synthesis	Catalytic performance	Ref.
ZMG1	Stepwise hydrothermal method	The degradation of MB dye and carbendazim under natural sunlight irradiation: 98% after 60 min	[16]
0.5 wt%MoS_2/ZnO	One-step hydrothermal method	Photocatalytic H_2 evolution: 98.1 μmol g^{-1} h^{-1}	[13]
ZMG4	Stepwise hydrothermal method	Photocatalytic H_2 evolution: 28.616 mmol h^{-1} g^{-1}	[37]
RGO 10%/ZnO 20%/MoS_2	One-step hydrothermal method	In real wastewater, the COD and TOC ratios decreased to zero and 7%, respectively after 440 min under the operational conditions.	[38]
MZG	One-step hydrothermal method	The growth of *E. coli* and *S. aureus* in Mueller Hinton agar in the concentration of 100 μg/mL was completely declined	[14]
25ZnO/75MG1	Stepwise hydrothermal method	100% degradation of BR18 dye for 180 min	[15]

5. Perspective

Despite the enormous potential of the ZnO/MoS_2/rGO ternary system as an efficient photocatalyst, it still faces significant challenges in both fundamental and practical aspects:

1) The content ratio of different components in the ternary system needs to be optimized for specific applications (**Figure 9**). A high co-catalyst content may lead to light shielding effects, reducing the number of active sites in ZnO and hindering the excitation of photogenerated charge carriers. On the other hand, a

low co-catalyst content may be insufficient to effectively prevent particle aggregation and achieve efficient charge separation.

2) The utilization of photocatalytic active sites is influenced by factors such as the size, morphology, pore structure, phase, and impurities of the highly efficient catalyst nanostructures. Therefore, the development of more efficient and diverse synthesis methods is crucial to synthesizing phases with high photocatalytic activity and achieving precise control.
3) Further optimization of the co-catalyst is still needed. Strategies such as heteroatom doping and introducing vacancies can improve the electron state density of the co-catalyst, leading to enhanced electron mobility and charge separation efficiency. Further exploration is required in this aspect.
4) A deeper understanding of the relationship between composition, structure, and performance requires a collaborative effort between theoretical calculations and experimental validation.

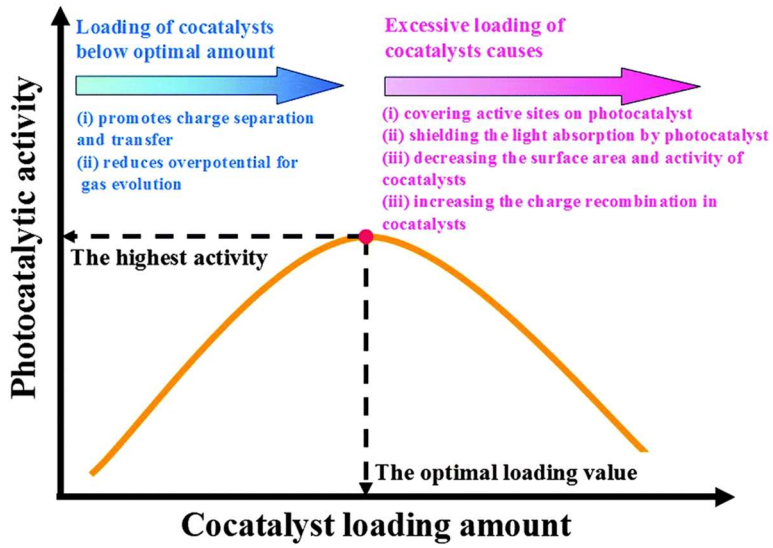

Figure 9. A volcano-type relationship between the loading amount of a cocatalyst and the photocatalytic activity of the cocatalyst-loaded semiconductor photocatalyst [21].

Addressing these challenges will require further research and exploration to achieve the efficient application of ZnO/MoS_2/rGO ternary system photocatalysts.

Funding: This work was financially supported by the Graduate Innovation Fund of Jilin University (Grant No. 2022177).

Conflict of interest: The authors declare no conflict of interest.

References

1. Fujishima A, Honda K. Electrochemical Photolysis of Water at a Semiconductor Electrode. Nature. 1972; 238(5358): 37-38. doi: 10.1038/238037a0
2. Sadhishkumar S, Balusamy T. Performance improvement in solar water heating systems—A review. Renewable and Sustainable Energy Reviews. 2014; 37: 191-198. doi: 10.1016/j.rser.2014.04.072
3. Zhao Z. Research progress of semiconductor photocatalysis applied to environmental governance. In: Proceedings of the 3rd

International Conference on Air Pollution and Environmental Engineering; 28-29 September 2020; Xi'an, China. doi: 10.1088/1755-1315/631/1/012022
4. Ge J, Zhang Y, Park SJ. Recent Advances in Carbonaceous Photocatalysts with Enhanced Photocatalytic Performances: A Mini Review. Materials. 2019; 12(12): 1916. doi: 10.3390/ma12121916
5. Dhiman V, Kondal N. MoS2-ZnO nanocomposites for photocatalytic energy conversion and solar applications. Physica B: Condensed Matter. 2022; 628: 413569. doi: 10.1016/j.physb.2021.413569
6. Ahamed M, Javed Akhtar M, Majeed Khan MA, et al. Facile green synthesis of ZnO-RGO nanocomposites with enhanced anticancer efficacy. Methods. 2022; 199: 28-36. doi: 10.1016/j.ymeth.2021.04.020
7. Cao M, Zhao L, Wang W, et al. Effects of dopants Ti and Al on microstructure, mechanical and tribological behaviors of ZnO/MoS2 coating deposited by magnetron co-sputtering. AIP Advances. 2019; 9(4). doi: 10.1063/1.5089905
8. Liu HQ, Yao CB, Jiang CH, et al. Preparation, modification and nonlinear optical properties of semiconducting MoS2 and MoS2/ZnO composite film. Optics & Laser Technology. 2021; 138: 106905. doi: 10.1016/j.optlastec.2020.106905
9. Friedman AL, Perkins FK, Hanbicki AT, et al. Dynamics of chemical vapor sensing with MoS2using 1T/2H phase contacts/channel. Nanoscale. 2016; 8(22): 11445-11453. doi: 10.1039/c6nr01979j
10. Yi L, Chang T. Loading direction dependent mechanical behavior of graphene under shear strain. Science China Physics, Mechanics and Astronomy. 2012; 55(6): 1083-1087. doi: 10.1007/s11433-012-4721-x
11. Feng S, Xu R. New Materials in Hydrothermal Synthesis. Accounts of Chemical Research. 2000; 34(3): 239-247. doi: 10.1021/ar0000105
12. Shi W, Song S, Zhang H. Hydrothermal synthetic strategies of inorganic semiconducting nanostructures. Chemical Society Reviews. 2013; 42(13): 5714. doi: 10.1039/c3cs60012b
13. Guan Z, Wang P, Li Q, et al. Remarkable enhancement in solar hydrogen generation from MoS 2 -RGO/ZnO composite photocatalyst by constructing a robust electron transport pathway. Chemical Engineering Journal. 2017; 327: 397-405. doi: 10.1016/j.cej.2017.06.125
14. Priyadharsan A, Shanavas S, Vasanthakumar V, et al. Synthesis and investigation on synergetic effect of rGO-ZnO decorated MoS2 microflowers with enhanced photocatalytic and antibacterial activity. Colloids and Surfaces A: Physicochemical and Engineering Aspects. 2018; 559: 43-53. doi: 10.1016/j.colsurfa.2018.09.034
15. Ugur N, Bilici Z, Ocakoglu K, et al. Synthesis and characterization of composite catalysts comprised of ZnO/MoS2/rGO for photocatalytic decolorization of BR 18 dye. Colloids and Surfaces A: Physicochemical and Engineering Aspects. 2021; 626: 126945. doi: 10.1016/j.colsurfa.2021.126945
16. Kumar S, Sharma V, Bhattacharyya K, et al. Synergetic effect of MoS2–RGO doping to enhance the photocatalytic performance of ZnO nanoparticles. New Journal of Chemistry. 2016; 40(6): 5185-5197. doi: 10.1039/c5nj03595c
17. Li J, Liu X, Pan L, et al. MoS2–reduced graphene oxide composites synthesized via a microwave-assisted method for visible-light photocatalytic degradation of methylene blue. RSC Advances. 2014; 4(19): 9647. doi: 10.1039/c3ra46956e
18. Wang M, Ioccozia J, Sun L, et al. Inorganic-modified semiconductor TiO_2 nanotube arrays for photocatalysis. Energy Environ Sci. 2014; 7(7): 2182-2202. doi: 10.1039/c4ee00147h
19. Cheng Z, Qi W, Pang CH, et al. Recent Advances in Transition Metal Nitride-Based Materials for Photocatalytic Applications. Advanced Functional Materials. 2021; 31(26). doi: 10.1002/adfm.202100553
20. Qiu J, Zhang X, Feng Y, et al. Modified metal-organic frameworks as photocatalysts. Applied Catalysis B: Environmental. 2018; 231: 317-342. doi: 10.1016/j.apcatb.2018.03.039
21. Ran J, Zhang J, Yu J, et al. Earth-abundant cocatalysts for semiconductor-based photocatalytic water splitting. Chem Soc Rev. 2014; 43(22): 7787-7812. doi: 10.1039/c3cs60425j
22. Labhane PK, Patle LB, Sonawane GH, et al. Fabrication of ternary Mn doped ZnO nanoparticles grafted on reduced graphene oxide (RGO) sheet as an efficient solar light driven photocatalyst. Chemical Physics Letters. 2018; 710: 70-77. doi: 10.1016/j.cplett.2018.08.066
23. Lu D, Wang H, Zhao X, et al. Highly Efficient Visible-Light-Induced Photoactivity of Z-Scheme g-C3N4/Ag/MoS2 Ternary Photocatalysts for Organic Pollutant Degradation and Production of Hydrogen. ACS Sustainable Chemistry & Engineering. 2017; 5(2): 1436-1445. doi: 10.1021/acssuschemeng.6b02010
24. Wang S, Ren C, Tian H, et al. MoS2/ZnO van der Waals heterostructure as a high-efficiency water splitting photocatalyst: a first-principles study. Physical Chemistry Chemical Physics. 2018; 20(19): 13394-13399. doi: 10.1039/c8cp00808f
25. Xiang Q, Yu J, Jaroniec M. Synergetic Effect of MoS_2 and Graphene as Cocatalysts for Enhanced Photocatalytic H_2

Production Activity of TiO_2 Nanoparticles. Journal of the American Chemical Society. 2012; 134(15): 6575-6578. doi: 10.1021/ja302846n

26. Chakrabarty S, Mukherjee A, Basu S. RGO-MoS_2 Supported $NiCo_2O_4$ Catalyst toward Solar Water Splitting and Dye Degradation. ACS Sustainable Chemistry & Engineering. 2018; 6(4): 5238-5247. doi: 10.1021/acssuschemeng.7b04757
27. Li Y, Xie W, Hu X, et al. Comparison of Dye Photodegradation and its Coupling with Light-to-Electricity Conversion over TiO_2 and ZnO. Langmuir. 2009; 26(1): 591-597. doi: 10.1021/la902117c
28. Wei Y, Huang Y, Wu J, et al. Synthesis of hierarchically structured ZnO spheres by facile methods and their photocatalytic deNO_x properties. Journal of Hazardous Materials. 2013; 248-249: 202-210. doi: 10.1016/j.jhazmat.2013.01.012
29. Moafi HF, Zanjanchi MA, Shojaie AF. Tungsten-doped ZnO nanocomposite: Synthesis, characterization, and highly active photocatalyst toward dye photodegradation. Materials Chemistry and Physics. 2013; 139(2-3): 856-864. doi: 10.1016/j.matchemphys.2013.02.044
30. Ebadi M, Teymourinia H, Amiri O, et al. Synthesis of CeO_2/Ag/Ho nanostructures in order to improve photo catalytic activity of CeO_2 under visible light. Journal of Materials Science: Materials in Electronics. 2018; 29(10): 8817-8821. doi: 10.1007/s10854-018-8899-1
31. Xie G, Zhang K, Guo B, et al. Graphene-Based Materials for Hydrogen Generation from Light-Driven Water Splitting. Advanced Materials. 2013; 25(28): 3820-3839. doi: 10.1002/adma.201301207
32. Zhang Y, Tang ZR, Fu X, et al. TiO_2−Graphene Nanocomposites for Gas-Phase Photocatalytic Degradation of Volatile Aromatic Pollutant: Is TiO_2−Graphene Truly Different from Other TiO_2−Carbon Composite Materials? ACS Nano. 2010; 4(12): 7303-7314. doi: 10.1021/nn1024219
33. Maity P, Mohammed OF, Katsiev K, et al. Study of the Bulk Charge Carrier Dynamics in Anatase and Rutile TiO_2 Single Crystals by Femtosecond Time-Resolved Spectroscopy. The Journal of Physical Chemistry C. 2018; 122(16): 8925-8932. doi: 10.1021/acs.jpcc.8b00256
34. Lu X, Chen A, Luo Y, et al. Conducting Interface in Oxide Homojunction: Understanding of Superior Properties in Black TiO_2. Nano Letters. 2016; 16(9): 5751-5755. doi: 10.1021/acs.nanolett.6b02454
35. Gomathisankar P, Hachisuka K, Katsumata H, et al. Photocatalytic hydrogen production with CuS/ZnO from aqueous Na_2S + Na_2SO_3 solution. International Journal of Hydrogen Energy. 2013; 38(21): 8625-8630. doi: 10.1016/j.ijhydene.2013.04.131
36. Kumar S, Sharma V, Bhattacharyya K, et al. N-doped ZnO–MoS_2 binary heterojunctions: the dual role of 2D MoS_2 in the enhancement of photostability and photocatalytic activity under visible light irradiation for tetracycline degradation. Materials Chemistry Frontiers. 2017; 1(6): 1093-1106. doi: 10.1039/c6qm00274a
37. Kumar S, Reddy NL, Kushwaha HS, et al. Efficient Electron Transfer across a ZnO–MoS_2–Reduced Graphene Oxide Heterojunction for Enhanced Sunlight-Driven Photocatalytic Hydrogen Evolution. ChemSusChem. 2017; 10(18): 3588-3603. doi: 10.1002/cssc.201701024
38. Ghasemipour P, Fattahi M, Rasekh B, et al. Developing the Ternary ZnO Doped MoS_2 Nanostructures Grafted on CNT and Reduced Graphene Oxide (RGO) for Photocatalytic Degradation of Aniline. Scientific Reports. 2020; 10(1). doi: 10.1038/s41598-020-61367-7
39. Haghighi N, Abdi Y, Haghighi F. Light-induced antifungal activity of TiO_2 nanoparticles/ZnO nanowires. Applied Surface Science. 2011; 257(23): 10096-10100. doi: 10.1016/j.apsusc.2011.06.145

Energy Storage and Conversion 2024, 2(2), 1136.
https://doi.org/10.59400/esc.v2i2.1136

Review

Chemical material as a hydrogen energy carrier: A review

Yunji Kim, Heena Yang*

Water Energy Research Center, Korea Water Resources Corporation, Daejeon 34045, Republic of Korea
*** Corresponding author:** Heena Yang, heena.yang@kwater.or.kr

CITATION

Kim Y, Yang H. Chemical material as a hydrogen energy carrier: A review. Energy Storage and Conversion. 2024; 2(2): 1136. https://doi.org/10.59400/esc.v2i2.1136

ARTICLE INFO

Received: 29 February 2024
Accepted: 17 April 2024
Available online: 23 May 2024

Abstract: In light of climate change imperatives, there is a critical need for technological advancements and research endeavors towards clean energy alternatives to replace conventional fossil fuels. Additionally, the development of high-capacity energy storage solutions for global transportability becomes paramount. Hydrogen emerges as a promising environmentally sustainable energy carrier, devoid of carbon dioxide emissions and possessing a high energy density per unit mass. Its versatile applicability spans various sectors, including industry, power generation, and transportation. However, the commercialization of hydrogen necessitates further technological innovations. Notably, high-pressure compression for hydrogen storage presents safety challenges and inherent limitations in storage capacity, resulting in about 30%–50% loss of hydrogen production. Consequently, substantial research endeavors are underway in the domain of material-based chemical hydrogen storage that causes reactions to occur at temperatures below 200 ℃. This approach enables the utilization of existing infrastructure, such as fossil fuels and natural gas, while offering comparatively elevated hydrogen storage capacities. This study aims to introduce recent investigations concerning the synthesis and decomposition mechanisms of chemical hydrogen storage materials, including methanol, ammonia, and Liquid Organic Hydrogen Carrier (LOHC).

Keywords: hydrogen storage; chemical hydride; catalysis; hydrogenation

1. Introduction

Conventional fossil fuels, while meeting global energy demand, generate carbon dioxide, a major contributor to global warming, making their limited resources and the quest for securing clean energy sources globally imperative [1–8]. Initially, research and industrial focus on environmentally friendly energy were primarily directed towards power production using renewable sources such as solar and wind energy. However, reliance on these sources can lead to unstable power production due to their susceptibility to environmental factors [9–18]. Furthermore, the storage of generated power is limited to short-term storage (~week) through Energy Storage Systems (ESS), necessitating alternative solutions for long-term (~season) and stable power supply. In this context, hydrogen has garnered attention as an environmentally friendly substance with a closed reaction cycle capable of producing water upon reaction, thereby facilitating the regeneration of hydrogen [19–28]. With significant chemical energy (142 MJ) and a high energy storage density per unit weight (three times that of gasoline), hydrogen serves not only as a fuel but also enables long-term storage (~year), making it viable for energy transportation. In view of the transportation sector, it is important to achieve sustainable goals by using hydrogen fuel. It also should consider the real data, which is collected from hydrogen commercial products, to evaluate direct and indirect effects [29]. However, hydrogen possesses a low volumetric storage density, posing a significant challenge in safely storing and

transporting large quantities, which is crucial for transitioning to a hydrogen-based society that efficiently utilizes renewable energy [30–39]. While hydrogen utilization technology for fuel, such as fuel cells, has reached a commercially viable stage with secured infrastructure, efficient large-scale hydrogen storage technology necessitates extensive research and development efforts for commercialization [40–45].

Various methods exist for hydrogen storage and transportation. Notably, storing gaseous hydrogen at high pressure (350~700 bar) in storage tanks and transporting it via tube trailers is a prominent approach, as is liquefying gaseous hydrogen (−253 °C) and storing it in dedicated storage tanks. These methods require specialized infrastructure due to the high energy density of hydrogen, and liquefaction, in particular, incurs significant energy consumption [46–59]. As alternatives, research is underway on physically adsorbing hydrogen onto porous materials such as Metal Organic Frameworks (MOFs) and carbon nanotubes for storage and transportation, as well as chemically binding hydrogen to metals to enable solid-state storage and desorption, as seen in metal hydrides. Furthermore, compounds formed by combining hydrogen with carbon, nitrogen, or boron atoms, such as methanol, ammonia, and Liquid Organic Hydrogen Carriers (LOHCs), offer a chemical hydrogen storage system with high storage density and ease of storage compared to molecular hydrogen storage. **Figure 1** illustrates these various chemical hydrogen carriers [60–81]. Utilizing such liquid compound-based hydrogen facilitates easy application due to its compatibility with existing fossil fuel or natural gas infrastructure, thus saving additional infrastructure construction costs and enhancing its commercial viability. The dehydrogenation reactions required to get hydrogen from chemical hydrogen carriers commonly employ catalysts such as Fe, Ni, Pt, and Ru to promote exothermic reactions. Therefore, the development of catalysts enabling higher hydrogen production rates and efficiency at lower temperatures, along with high-purity hydrogen extraction, is imperative [82–96]. The hydrogen produced requires refinement, with coupling to existing commercial hydrogen production methods such as Steam Methane Reforming (SMR) with separation and purification facilities allowing for cost savings in hydrogen production by separating carbon monoxide and carbon dioxide [97–111].

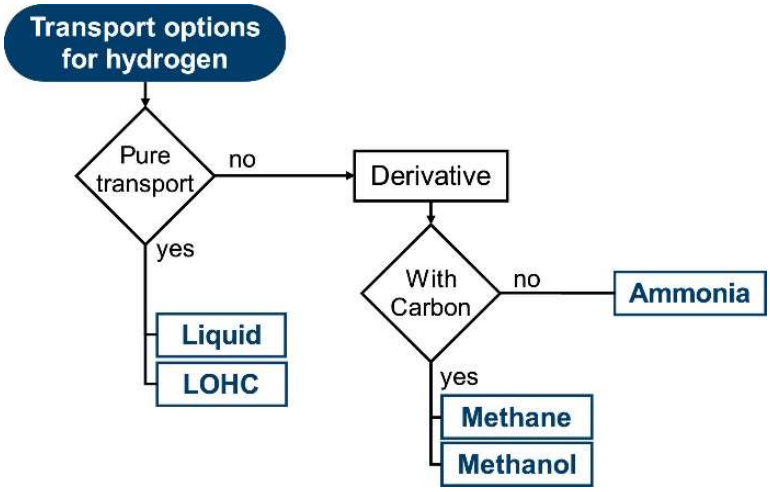

Figure 1. Considered intercontinental transport options for hydrogen as a renewable energy carrier [81].

This study aims to provide a comprehensive overview of the synthesis methods and technological advancements for the efficient extraction of hydrogen from commercially researched and viable chemical hydrogen carriers such as methanol, ammonia, and LOHCs. It includes the various catalyst studies with hydrogen conversion rates. Additionally, it seeks to offer an economic analysis of these chemical hydrogen carriers, comparing them to shed light on factors to consider during the transition from fossil fuels to hydrogen applications. By doing so, it will contribute to elucidating the future direction of the chemical industry, which previously held a dominant position in petrochemistry, considering elements such as chemical hydrogen carriers.

2. Chemical hydrogen carriers

2.1. Methanol

Methanol, a versatile raw material widely used in various industries such as hydrogen fuel (road, maritime, etc.), industrial fuel (boilers, etc.), and as a feedstock in the petrochemical industry (plastics, etc.), forms a large-scale market, producing approximately 65 million tons globally [21,23–24]. Methanol, being the simplest compound producible from natural gas and renewable energy sources, exhibits a high hydrogen storage density of 12 wt%. Utilizing methanol as hydrogen storage offers several advantages: 1) Methanol reforming can be conducted at much lower temperatures (150–450 °C) compared to natural gas reforming; 2) It can leverage the infrastructure of fossil fuels such as gasoline, diesel, and kerosene for various applications (transportation, fuel, power generation, etc.); and 3) It is relatively stable as a liquid and easy to store under normal environmental conditions [25–27]. Researchers are actively exploring the utilization of methanol as a fuel synthesized from biomass and carbon-containing sources, including carbon dioxide, with the aim of enhancing its economic viability. **Figure 2** shows the carbon cycle utilization of methanol [30,39,83–84]. The synthesis reactions of methanol are presented in **Table 1** [26].

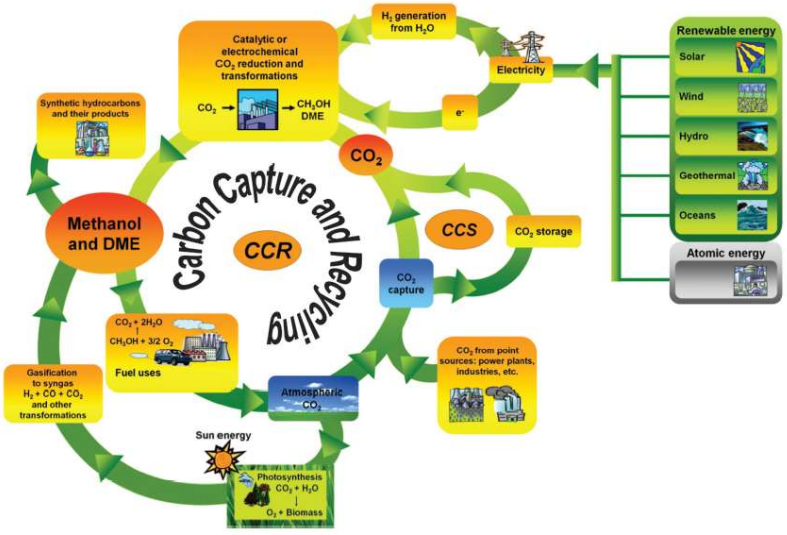

Figure 2. Anthropogenic carbon cycle within the Methanol Economy [25].

Table 1. Processes and Conditions for hydrogen production from Methanol [26].

Process	T(K)	Reaction	Advantage/Disadvantage
MSR (Methanol steam reforming)	423-623	$CH_3OH + H_2O \leftrightarrow CO_2 + 3H_2$	Low Temperature High Methanol conversion Low CO content /Steam preheating Water waste management
MD (Methanol decomposition)	373-723	$CH_3OH \leftrightarrow CO + 2H_2$	/High CO content
POM (Partial oxidation)	300-723	$CH_3OH + 0.5O_2 \leftrightarrow CO + 2H_2$	Reduction of heating cost /High CO content
ATRM (Autothermal reforming)	473-823	$CH_3OH + rO_2 + (1\text{-}2r)H_2O \leftrightarrow (3\text{-}2r)CO_2 + 2H_2$	Hydrogen-rich gas Reduction of heating cost /Need catalyst

Methanol can be synthesized by the reaction of carbon dioxide and hydrogen through endothermic reactions in Methanol Steam Reforming (MSR) processes to produce hydrogen. Among the introduced processes, MSR has the longest history and operates at relatively low temperatures (200–350 °C) without producing carbon monoxide. When carbon monoxide is present, it reacts with hydrogen to synthesize methanol, which is primarily employed in large-scale methanol production. Methanol Partial Oxidation (POM) methods, widely used in hydrogen production, offer the advantage of fast reaction rates and exothermic processes, enabling cost savings through heat application. However, POM entails complex oxidation, steam reforming, and decomposition reactions and tends to produce relatively impure hydrogen due to its high carbon monoxide content. A hybrid process combining MSR and POM, known as Autothermal Reforming (ATR), utilizes the heat generated in the exothermic POM reaction to drive the MSR reaction, simplifying the process. ATR offers advantages such as low energy requirements and rapid gas generation compared to other processes but needs optimized catalysts for obtaining appropriate products [84–91]. Catalysts used in the reforming reaction of methanol should possess excellent catalytic activity and stability to ensure large-scale hydrogen production and high conversion rates. Additionally, considering the generation of carbon monoxide during reforming, which can affect the purity of hydrogen, it is necessary to inhibit its formation by having high selectivity. Up to now, catalysts primarily based on Cu, Ni, and Pd have been utilized in methanol reforming reactions, and various research efforts are underway to enhance these catalyst properties. For instance, although $Cu/ZnO/Al_2O_3$, commonly used in commercial methanol synthesis, exhibits high activity, its stability decreases at high temperatures, leading to natural ignition, sintering, and deactivation. Consequently, various studies have been conducted to improve stability [94,95,104]. Cu-based catalysts typically involve a reaction between oxygen and hydrogen at two adsorption sites, as shown in **Figure 3** [89].

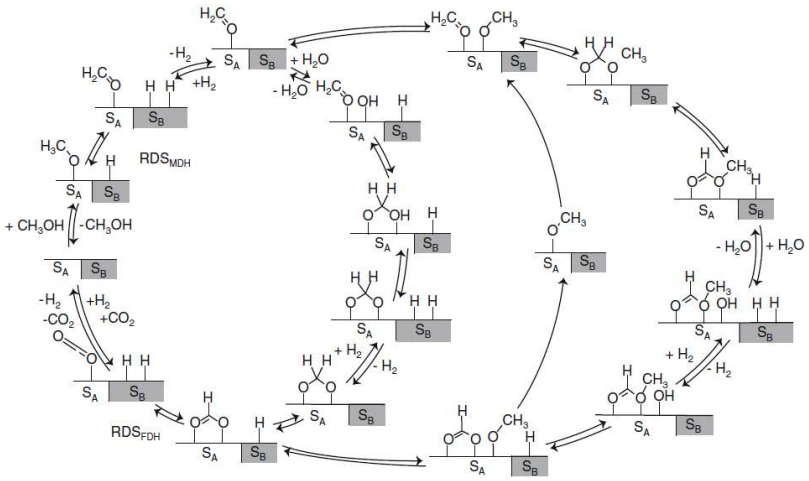

Figure 3. Catalysis cycle for MSR over Cu-based catalysts including two different kinds of reactive sites SA (adsorption and desorption of oxygenates) and SB (adsorption and desorption of hydrogen) [89].

Cu-based catalysts, commonly supported on materials such as Cu/ZnO or Cu/TiO_2 using Al-based supports, undergo research involving the addition of elements to improve methanol conversion rates and stability. Additives such as Mg and Ni enhance catalyst particle nanostructuring, dispersion, and activity. Notably, the addition of optimized Mg to Cu/ZnO/Al-5Mg catalysts has shown a reduction in particle size from 7.8 nm to 3.5 nm and an improvement in methanol conversion rates from 56% to 68% [96–98].

Similarly, Ni-based catalysts, predominantly supported on Al-based supports, exhibit enhanced catalytic performance with various additives. Using Ti oxide-based materials instead of Al-based supports in Ni catalysts revealed superior properties such as excellent oxidation-reduction characteristics, high concentrations of chemisorbed oxygen, and a hierarchical porous structure. Through simulations of methanol steam reforming reactions on Ti oxide-based catalysts using the Vienna Ab initio Simulation Package (VASP), $NiTiO_3$ catalysts were found to enhance the adsorption energy and activation of methanol molecules on the Ni-Ti-Ox catalyst surface (**Figure 4**), exhibiting methanol conversion rates (873 K) and H_2 selectivity of 99.9%. This demonstrates superior catalytic characteristics compared to $Ni\text{-}Al_2O_3$ catalysts mixed with Al-based materials, which exhibit methanol conversion rates of 77% and H_2 selectivity of 91.2% [97,99–102].

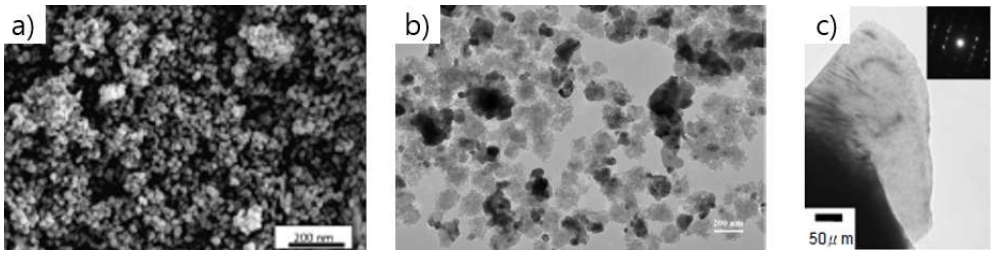

Figure 4. Scanning of particle size in the follow research: **(a)** Field emission scanning electron microscopy (FESEM) image; **(b)** Transmission electron microscopy (TEM) image; **(c)** Typical Dislocation free zone in fine particle [96–98].

Recent research in methanol reactions has witnessed active investigations into Pd-based catalysts, comparing the methanol reactions of Pd and PdZn catalysts using various supports. Comparisons of methanol production with Pd/TiO_2 and Pd/Al_2O_3 catalysts with and without Zn inclusion at constant pressure (20 bar) in the temperature range of 175~250 °C revealed increased methanol production and decreased methane selectivity when Zn was incorporated into the catalysts. This demonstrates the superior stability of PdZn alloys compared to other bimetallic alloys. Pd/Ga_2O_3 catalysts, regardless of the presence of Zn, exhibited high methanol selectivity when using Ga_2O_3 as a support material [95]. Methanol production using various Pd-based catalysts can be compared in **Figure 5**, and the various characteristics of catalysts used in methanol reactions are summarized in **Table 2**.

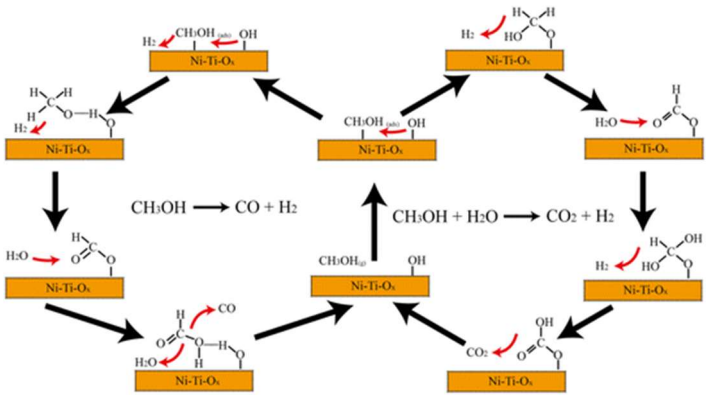

Figure 5. Reaction mechanism diagram of Ni–Ti–Ox catalyst [93].

Table 2. Comparison of catalytic performance of Methanol production [30–32,96–102].

Catalyst	T(K)	Electrochemical surface area (m^2/g)	Cycle(hour)	H_2 selectivity (%)	Conversion (%)
NiPd-C	298	14.5	2	N/A	N/A
NiPd-MSN	298	19.53	2	N/A	N/A
Pd-NiO_x-P/C	298	5.76	3	N/A	N/A
Pd/C	298	2.56	3	N/A	N/A
Pd-NiO_x/C	298	4	3	N/A	N/A
Pd/ZrO_2-TiO_2	523	N/A	5	66	22
MoC	573	N/A	12	N/A	30
$Cu/ZnO/Al_2O_3$	523	N/A	1	82.3	98.8
Ni/Al_2O_3	773	N/A	N/A	91.2	77
Ni-Cu/Al_2O_3	773	N/A	24	99.1	86.3
10La-10Ni/Al_2O_2	300	N/A	3	68	99
Cu-Ni/TiO_2	573	N/A	10	92.7	92.6
Cu/TiO_2	573	N/A	10	90	90.2
Pt/TiO_2	573	N/A	10	94	95.5
Ru/TiO_2	573	N/A	10	97.8	98.9

Furthermore, the cost of methanol production is heavily dependent not only on catalysts but also on the costs of hydrogen and carbon dioxide. Economic analysis conducted on the utilization of methanol produced from renewable sources (clean

methanol) as an energy carrier indicates that to ensure methanol production within the current market price range, hydrogen costs must be below 2.5 €/kg within ten years. Therefore, improvements in catalyst performance should be accompanied by reductions in raw material costs. The cost analysis of methanol is shown in **Figure 6** [81].

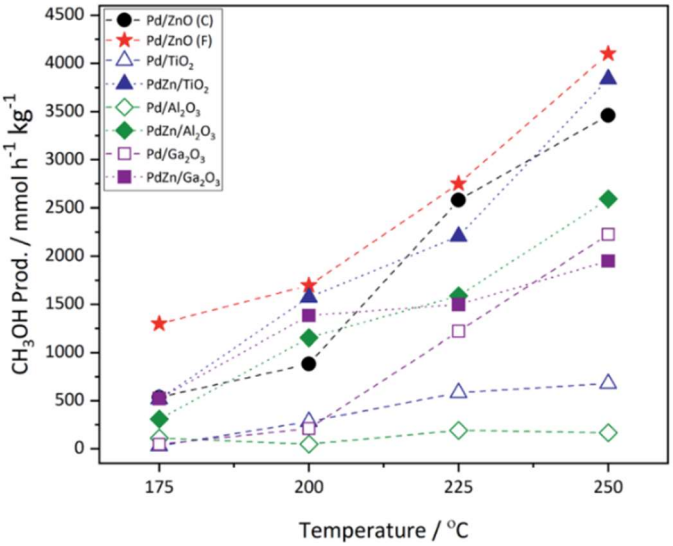

Figure 6. Methanol productivity as a function of CO_2 hydrogenation reaction temperature over Pd and PdZn supported catalyst [95].

2.2. Ammonia

Ammonia is one of the oldest and most widely produced compounds in the world, with sufficient infrastructure established for its production, transportation, and distribution. Currently, over 85% of the ammonia production in most plants (more than 200 million tons annually) is used as fertilizer, with the remainder primarily utilized in the chemical and processing industries. Ammonia (NH_3) is a stable binary hydride and the simplest hydride of nitrogen. From the perspective of hydrogen production, ammonia serves as an excellent hydrogen carrier, demonstrating a hydrogen storage capacity of 17.7 wt% at 20 °C and existing in a liquid state at around −30 °C, making it easy to store and transport. Consequently, there is active development of storage compounds and fuel cell technologies utilizing ammonia [103–122].

However, due to the substantial emission of carbon dioxide during the synthesis process and its inherent toxicity, technological development to address these issues is essential to utilizing ammonia as an environmentally friendly hydrogen energy carrier. The comparison of hydrogen storage capacities using ammonia is shown in **Figure 7** [104].

Currently, most of the ammonia is produced using the Haber-Bosch process, which utilizes catalysts based on Fe catalysts at high- temperatures (above 673 K) under high pressure (20–40 MPa). The synthesis and decomposition mechanisms of ammonia are shown in **Figure 8** [107].

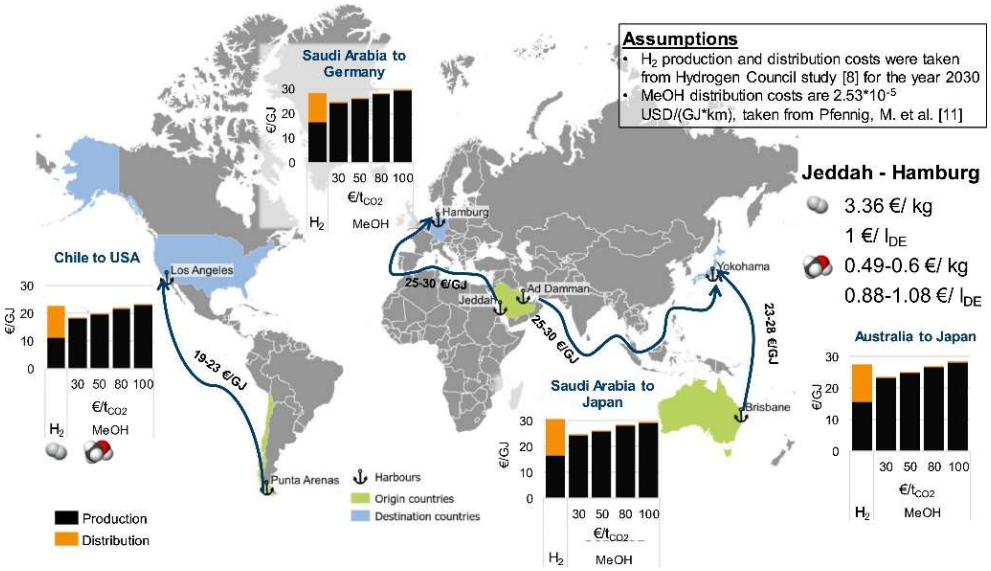

Figure 7. Hydrogen and methanol production and distribution costs for the four investigated origin/destination combinations [81].

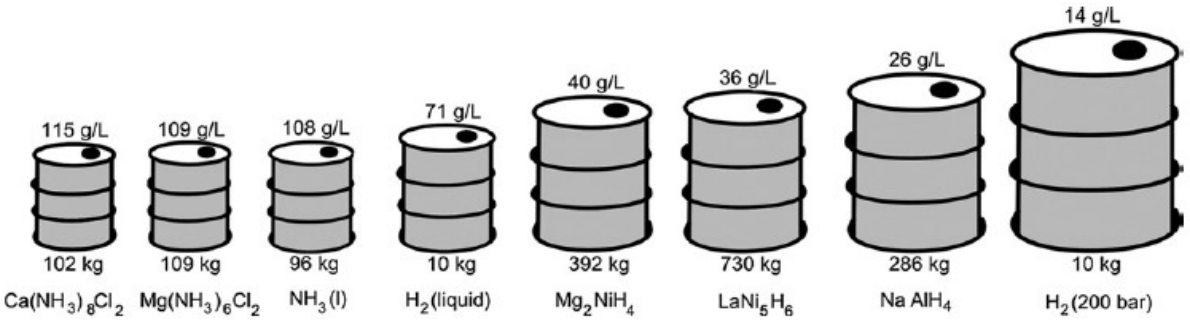

Figure 8. Mass and volume of 10 kg hydrogen stored reversibly by 8 different methods, based on the best obtained reversible densities without considering the space or weight of the container [104].

Ammonia synthesis is an exothermic reaction between nitrogen and hydrogen, requiring high temperatures and pressures to break the chemical bonds within nitrogen molecules. Due to the significant emission of carbon dioxide and the need to reduce energy consumption caused by the high temperatures and pressures required for ammonia synthesis, the development of new production processes is essential for using ammonia as an environmentally friendly hydrogen energy carrier. Research is actively underway to utilize catalysts to lower reaction temperatures and increase reaction rates to reduce energy consumption. Various ammonia synthesis processes are summarized in **Table 3** [106–109].

Table 3. Processes and Condition of Ammonia reaction based hydrogen Production [106–109].

Process	Condition	Reaction	Advantage/Disadvantage
Haber-Bosch method	573–773 K 200–350 atm	$N_2 + 3H_2 \leftrightarrow 2NH$	High conversion rate/High CO_2 content High temperature and pressure
Photocatalysis method	300–500 K 1 atm	$N_2 + 3H_2O \leftrightarrow 2NH_3 + 1.5O_2$	Low temperature and pressure/Need catalyst technology
Electrocatalysis method	773 K 1 atm	1) $3H_2 \leftrightarrow 6H^+ + 6e^-$ 2) $N_2 + 6H^+ + 6e^- \leftrightarrow 2N_2H$ 3) $N_2 + 3H_2 \leftrightarrow 2NH_3$	Low energy consumption/Low efficiency Low production rate of ammonia

Ammonia catalysts typically use carbon-based supports and employ a variety of materials such as Pt, Rh, Co, Cs, Fe, and Ru as catalysts. Researches have been conducted on various carbon-supported catalysts, including carbon nanotubes, graphene, and carbonaceous materials doped with boron or nitrogen. Studies have shown that when using supported catalysts, a uniform dispersion of catalytic particles can be achieved, leading to improved catalyst activity and durability. Indeed, when boron-doped carbon materials were used as catalysts for synthesizing ammonia, a decrease in activation energy was observed, as depicted in **Figure 9** [108].

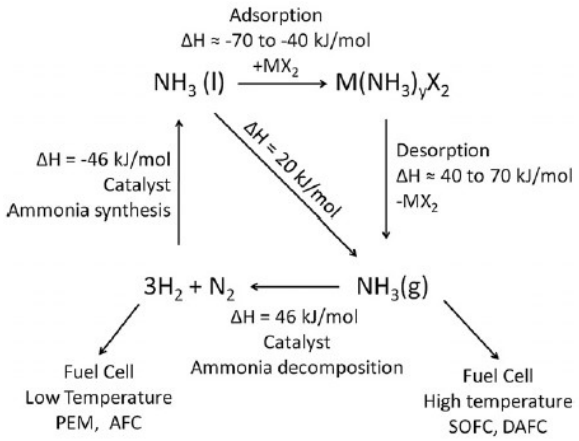

Figure 9. The life-cycle of hydrogen stored as ammonia in metal ammines, $M(NH_3)_yX_2$ [107].

Research on nanostructuring previously used Fe-based catalysts has demonstrated improvements in efficiency and long-term stability during operation. Moreover, introducing Cs into Fe catalysts has been shown to increase the rate of ammonia production, as depicted in **Figure 10** [110].

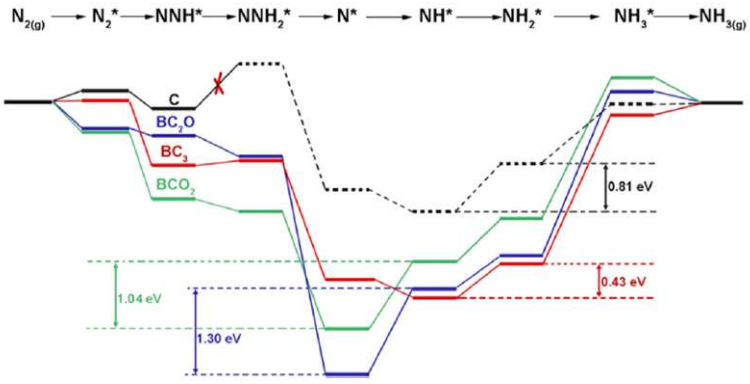

Figure 10. Free-energy diagrams of Boron-doped carbon samples for electrochemical Nirogen Reduction Reaction (NRR) [108].

In addition to carbon-based supports, research on catalysts using various supports is also underway. One such study aimed to enhance stability using a catalyst supported on MgO for Cs/Ru alloy, comparing the catalytic activity over 680 h of operation. It was observed that while the catalyst exhibited consistent activity at an initial temperature of 325 °C for 150 h, the activity decreased at higher temperatures, maintaining only 42% of its initial activity after 680 h. Therefore, the development of

long-term active catalysts for ammonia production as energy carriers is crucial. Structural changes in the catalyst over time are shown in **Figure 11** [111].

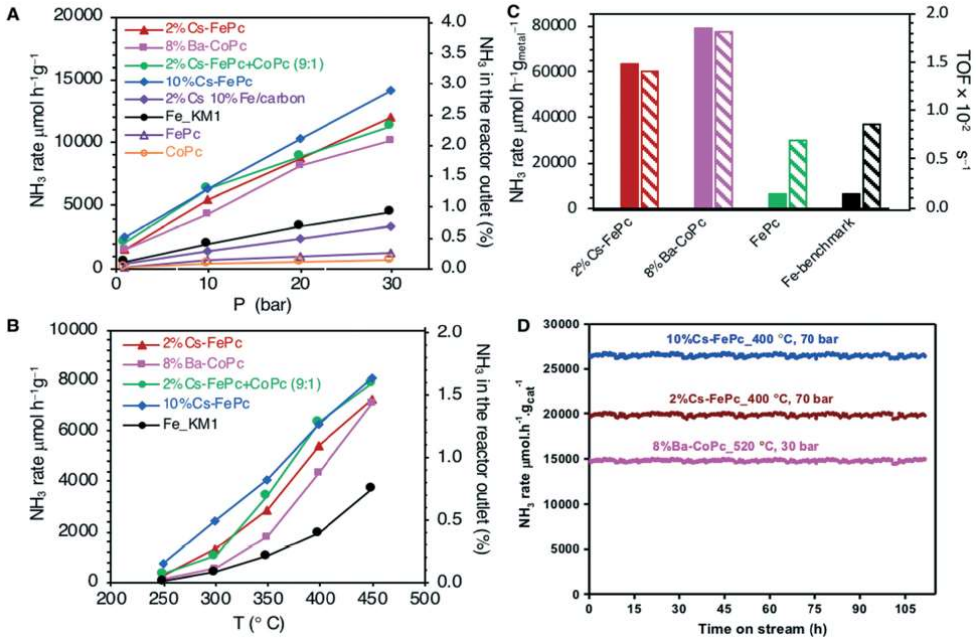

Figure 11. Structural changes in the catalyst over time for the ammonia synthesis reaction. **(A)** Pressure effect at 400 °C; **(B)** Temperature effect at 1 MPa; **(C)** Specific at 400 °C and 3 MPa; **(D)** Time dependence of the catalytic activities for stability testing in the range of 400–520 °C and 3–7 MPa [110].

Research has also been conducted on Ni-based catalysts, such as $Ni_2Mg_3Al_2$-HT, which demonstrated the highest NH_3 conversion rate and H_2 productivity at 500 °C. The ammonia conversion rate is shown in **Figure 12**. The structural characteristics of the catalyst significantly influence its activity, with parameters such as particle size, dispersion, crystalline structure, surface area, acidity, and thermal stability playing important roles. Optimization of structural characteristics enhances catalyst activity; for example, smaller particle size, higher dispersion, and acidity lead to increased catalytic activity, while higher thermal stability extends catalyst lifespan [112].

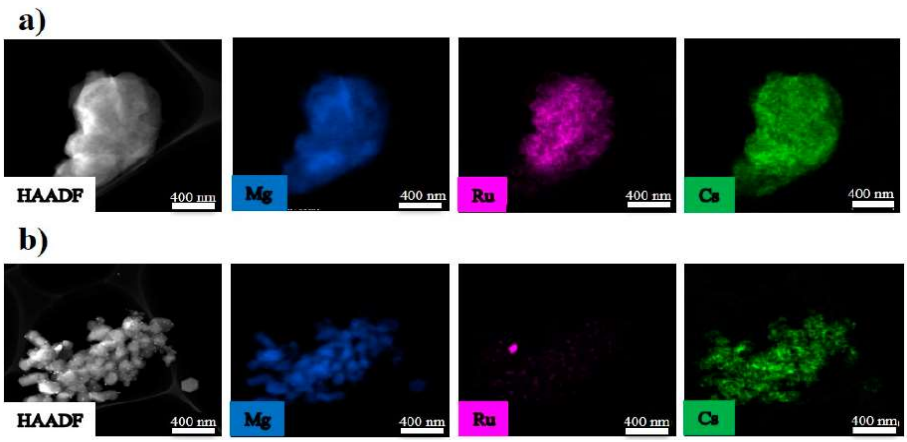

Figure 12. HAADF-STEM images with elemental mapping for Mg, Ru, and Cs: **(a)** as-synthesized catalyst; **(b)** after a time on stream of 680 h [111].

Research focusing on the durability of catalysts has proposed the use of pellet-shaped catalysts instead of powdered forms. By synthesizing highly durable Ru/La-Al_2O_3 pellet catalysts and designing catalyst reactors accordingly, a high catalyst activity and stability of 83.6% for reforming efficiency were achieved (**Figure 13**). It was confirmed that there was almost no CO_2 emission during the reaction process, introducing an environmentally friendly ammonia synthesis process [113].

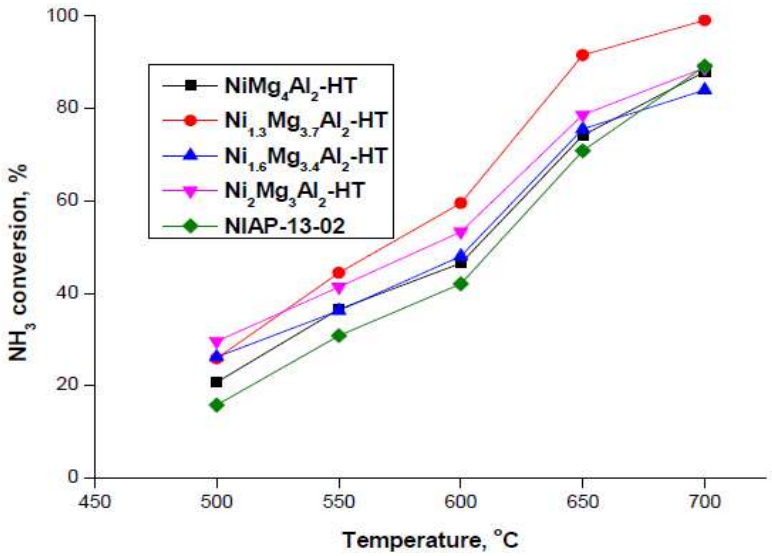

Figure 13. The influence of the reaction temperature on NH_3 conversion over $Ni_xMg_yAl_2$-HT catalysts [112].

Such reactors are capable of reforming processes for systems ranging from 10 kW to 10 MW for ammonia, showing significant potential for reducing CO_2 emissions. Ultimately, an investigation and analysis of the technical and economic feasibility of ammonia reforming for hydrogen production have been reported, showing the possibility of obtaining hydrogen at relatively similar prices to conventional production pathways (fossil fuels), as shown in **Figure 14** [112]. Various catalysts for ammonia synthesis are summarized in **Table 4** [114–123].

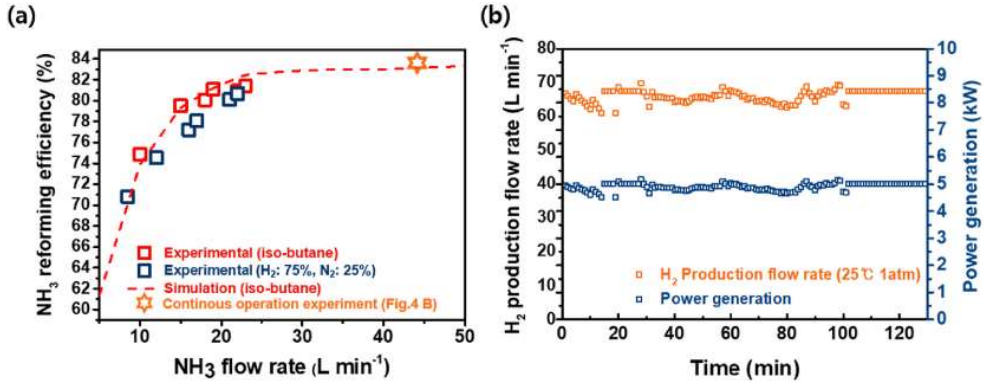

Figure 14. (a) NH_3 reformer efficiency over NH_3 flowrate using iso-butane and a product mixed gas of the system (H_2: 75%, N_2: 25%) as heat sources; **(b)** H_2 production flow and power generation (fuel cell equivalent) of the operated system continuously over 2 h [113].

Table 4. Comparison of catalytic performance of reported Ammonia catalysts [114–123].

Catalyst	T(K)	Electrochemical Surface Area (m^2/g)	Cycle(hour)	Conversion (%)	H_2 production rate(ml/min)
PtCO	473–573	74.48	30	N/A	N/A
Pt/C	823–973	74.7	30	N/A	N/A
Ir/C	353	85	24	N/A	N/A
Rh/C	353	67	24	N/A	N/A
Pt-NiO/C	298	7.2	500	N/A	N/A
$NiMg_4Al_2$-HT	773	N/A	5	20.7	16.6
$Ni_2Mg_3Al_2$-HT	773	N/A	5	29.6	23.8
$Ni_{0.6}Mg_{0.3}Al_{0.6}O_n$	773	N/A	5	42	14.1
Ru-Cs/MIL	673	N/A	10	98	25
Co/CNT	723	N/A	2	30	0.02
Cs_2O/Ru/Pr_6O_{11}	623	N/A	75	45	10
Cs-Ru/graphene	723	N/A	4	85.8	N/A
Fe/CNT	873	N/A	4	51.3	N/A
$CoFe_5$/CNT	873	N/A	17	24	36
Ru/CNT	573	N/A	2	95.69	50

2.3. Liquid organic hydrogen carrier

In recent research and development fields, there has been attention drawn to the technology of synthesizing and storing hydrogen in the form of liquid organic molecules due to its relatively low cost and compatibility with existing fuel transportation infrastructure. Among various liquid compound-based hydrogen storage technologies, liquid organic compounds containing C-C double bonds have been extensively researched for their ability to store and transport large amounts of hydrogen at ambient pressure. These liquid organic compound-based hydrogen carriers are referred to as Liquid Organic Hydrogen Carriers (LOHC) [124]. LOHCs have several advantages: 1) They possess a high hydrogen storage capacity of approximately 7 wt%; 2) hydrogenation/dehydrogenation reactions occur reversibly under certain conditions; and 3) they are similar to gasoline and can utilize existing fossil fuel storage and transportation infrastructure without significant initial investment costs [123–127]. LOHCs allow for the repeated binding and release of hydrogen through chemical reactions without performance degradation. Therefore, optimization studies for LOHC-based hydrogen storage and transportation systems are actively conducted worldwide, and demonstration projects are underway to integrate LOHC systems with existing hydrogen infrastructure. However, continuous research and development efforts are needed due to the relatively low hydrogen density and availability compared to other hydrogen storage compounds (such as methanol and ammonia) [124,128–135]. Various LOHCs based on substances including benzene and toluene have been researched, and their characteristics are summarized in **Table 5** [126].

Table 5. Typical examples of potential LOHCs and their physicochemical properties [136].

LOHC System	H_2 Capacity (wt.%)	Enthalpy (kJ/mol)	Melting Point (K)		Boiling Point (K)		Flash Point (K)	
			H_2-Rich	H_2-Lean	H_2-Rich	H_2-Lean	H_2-Rich	H_2-Lean
Methylcyclohexane → Toluene 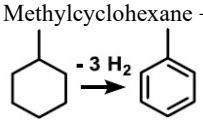	6.2	68.3	147	178	378	384	270	279
Decalin → Naphthalene 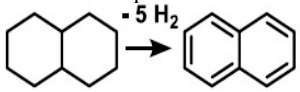	7.3	63.9	236	352	462	491	330	353
Perhydro-dibenzyl toluene → dibenzyl toluene Perhydro-benzyl 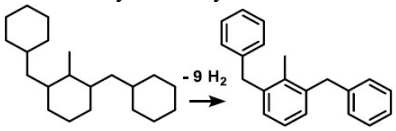	6.2	65.4	N/A	239	N/A	671	N/A	463
toluene → benzyl toluene 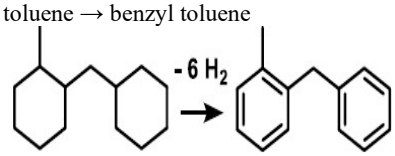	6.2	63.5	N/A	243	443	553	N/A	N/A
Dodecahydro-N-ethyl carbazole → N-ethyl carbazole 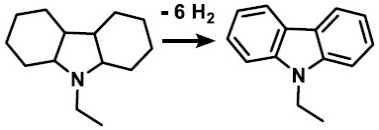	5.8	50.6	188	343	N/A	439	N/A	459
1-methylperhydro indole → 1-methy indole 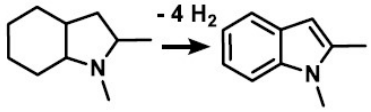	5.8	51.9	N/A	368	453	511	333	383
2-methylperhydro indole → 2-methy indole 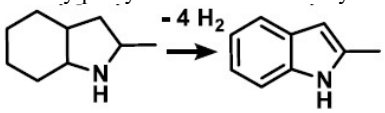	5.8	N/A	N/A	333	451	545	331	414
1,2-perhydrodimethyl indole → 1,2 dimethyl indole	5.23	N/A	<258	328	>533.5	533.5	>503	>503
Perhydro-phenazine → phenazine 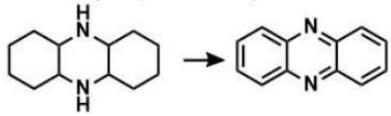	7.2	N/A	N/A	447-450	N/A	630.2	N/A	433.3
Perhydro-2-(n-methylbenzyl pyridine) → 2-(n-methylbenzyl pyridine) 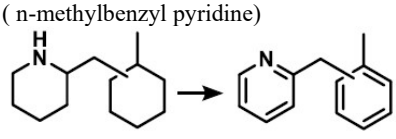	6.15	67.3	253.7	222.9	566	564	N/A	N/A

Various catalysts are being researched to enhance the hydrogen density of LOHCs and facilitate hydrogen adsorption-desorption reversible reactions. Metal-based catalysts such as Pt, Ru, Pd, and Ni are primarily used, and typically, inorganic

oxides such as Ti and Si are used as supports. Studies using Pt catalysts supported by γ-Al_2O_3 and TiO_2 have been conducted, revealing that γ-Al_2O_3 enhances the dispersion of highly nanosized Pt catalyst particles. Additionally, sulfurization improves hydrogen desorption reactions, with desorption rates of 97% and 87% reported for γ-Al_2O_3 and TiO_2 as support materials, respectively. Because the addition of sulfur seems to enhance the catalyst activity, leading to an extension of the fast dehydrogenation period. The structure and hydrogen desorption of these materials are shown in **Figures 15** and **16** [137].

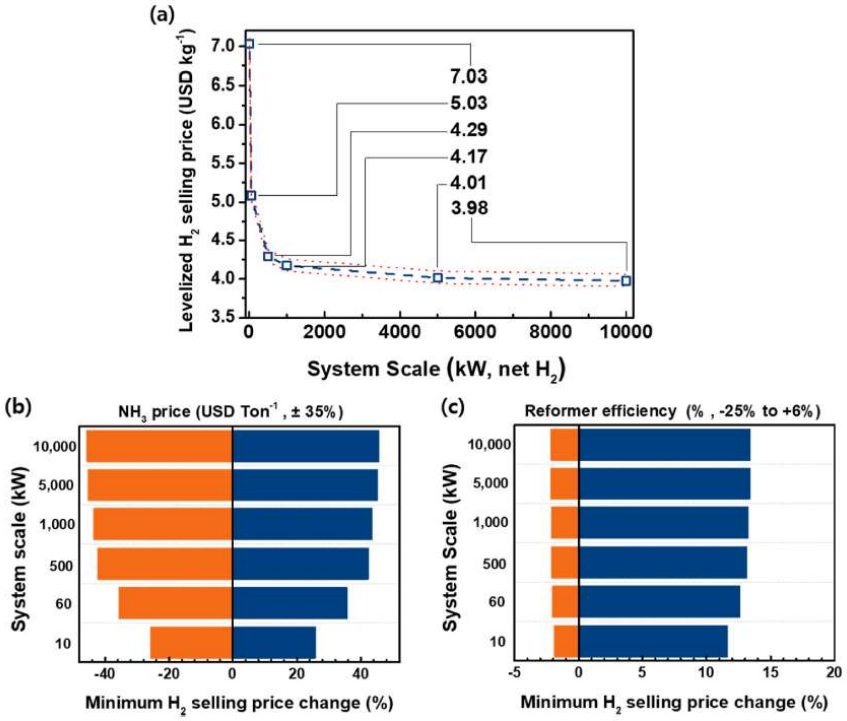

Figure 15. (a) The scale-up effect on minimum hydrogen selling price (MHSP). The error bars represent the average values of sensitivity parameter. Sensitivity analysis for 10 kW to 10 MW systems for parameters; **(b)** ammonia bulk price; and **(c)** reformer efficiency variation around a given data point [113].

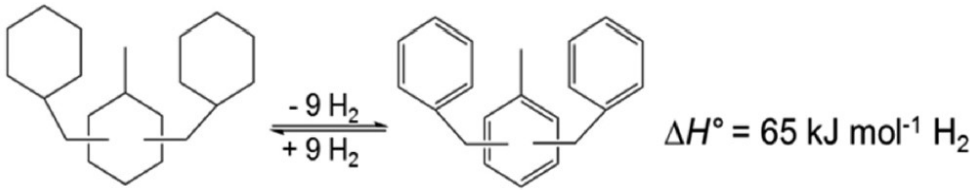

Figure 16. Reversible Dehydrogenation and Hydrogenation Scheme of the Perhydro Dibenzyltoluene/Dibenzyltoluene LOHC System [137].

Research on Pd catalysts supported by Al_2O_3 supports, specifically on Pd/a-Al_2O_3, investigated the coking of the catalyst due to hydrogen adsorption-desorption reactions with Methylcyclohexane (MCH)-based LOHCs. Under varying Ar flow conditions, two sizes of catalysts (6 nm and 15 nm) were compared, showing that smaller Pd nano-particles (6 nm) decomposed after generating the Pd6C phase and carbon deposition due to carbon separation, while larger Pd nano-particles (15 nm in diameter) coexisted

with two Pd carbide phases, Pd6C and PdxC, upon exposure to MCH, followed by carbonaceous precipitation and carbide decomposition (**Figure 17**). Consequently, it indicates that catalysts may exist in various carbide forms with different carbon contents under LOHC dehydrogenation conditions, and structural changes in catalyst nanoparticles are highly reversible. Other types and characteristics of LOHCs and catalysts are summarized in **Table 6** [124,131–132,135–136,138–146].

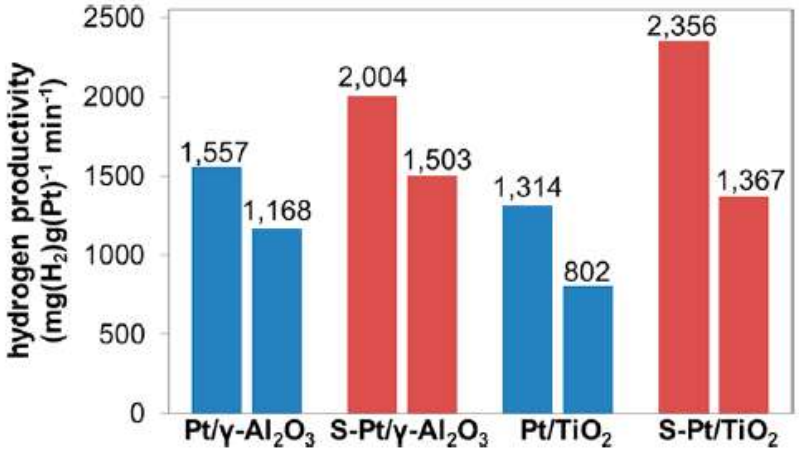

Figure 17. Hydrogen productivities normalized to metal dispersion (left column of each catalyst) in comparison to total Pt amount (right column of each catalyst) of the four catalysts [137].

Table 6. Comparison of catalytic performance of reported LOHC catalysts [124,131–132,135–136,138–146].

LOHCs	T (K)	Capacity (wt%)	Enthalpy (kJ/molH_2)	Conversion (%)	Catalysts	Yield (%)
N-ethylcarbazole	543	5.8	50.6	90	Ru Ru/TiO_2 Ni Pd/SiO_2-$TiO(OH)_2$	85 95 86.2 98.72
MCH-Toluene	593	6.2	68.3	95	Pd-Pt/SiO_2 Pd/SiO_2 Pt	91.4 85.4 90.8
Naphthalene	553	7.3	63.9	99	Pt Pd	97.6 73.15
Dibenzyl toluene	583	6.2	65.4	97	Ni/AlSiO Pt/Al_2O_3	85 92
Benzene	453–593	5	686	N/A	Pd-Pt/ SiO_2 Pd/SiO_2	90.8 84.1

Additionally, a comparative analysis of the technology and economic prospects of hydrogenation systems using high-density storage technologies and liquid organic hydrogen carriers (primarily ammonia or methanol) for large-scale hydrogen storage was conducted. Through analysis of the main system components of each technology, it was found that the cost of conventional liquid hydrogen storage is more than twice that of gaseous storage methods and more than four times that of storage methods using LOHCs. Although ammonia and methanol are considered suitable for large-scale hydrogen transportation as they can utilize existing fossil fuel infrastructure, they have the drawback of consuming energy and capital for synthesis and decomposition

compared to LOHCs. The comparison of energy consumption and equipment costs for storage is shown in **Figure 18** [134].

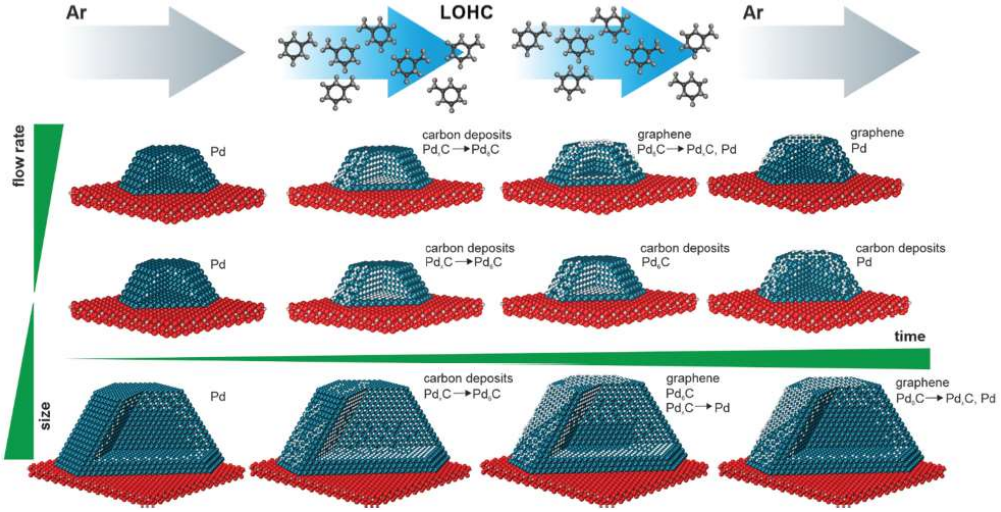

Figure 18. Schematic representation of the structural changes in the model $Pd/Al_2O_3(0001)$ catalysts as a function of the flow rate of the reactant, size of supported Pd nanoparticles, and time of the catalyst on stream at 500 K [133].

LOHCs appear to be an economically producible technology for large-scale fixed hydrogen storage, but they must overcome the challenge of lower hydrogen storage density compared to other hydrogen carriers in **Figure 19**. The hydrogen storage densities of each material are compared in **Figure 20**. There is an urgent need for high-efficiency catalyst development, enhancement of durability for reversible reactions, and the development of synthesis processes from small to large-scale production for LOHCs.

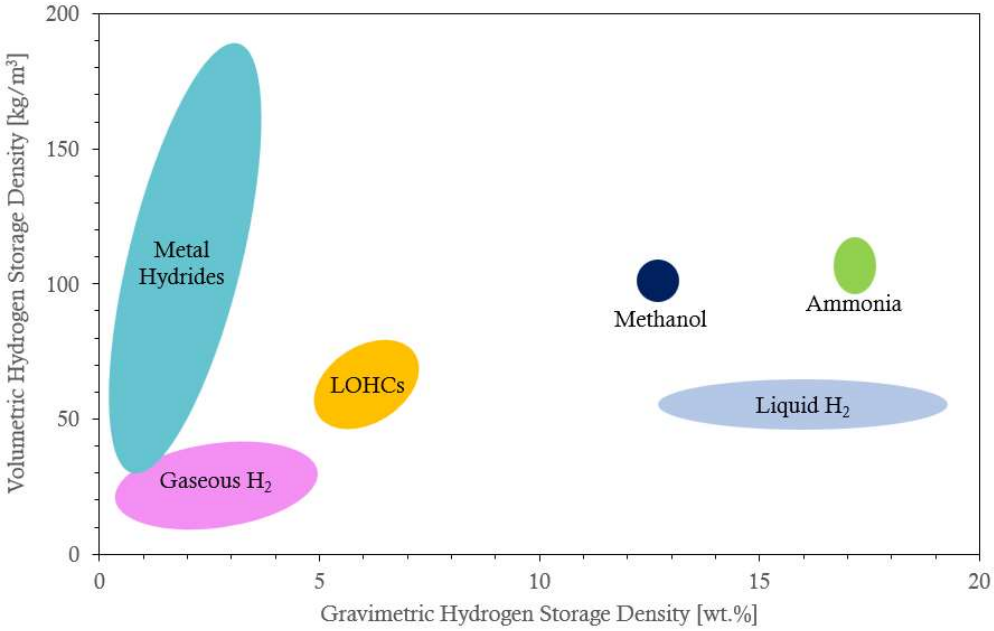

Figure 19. Hydrogen storage technologies and their energy densities [134].

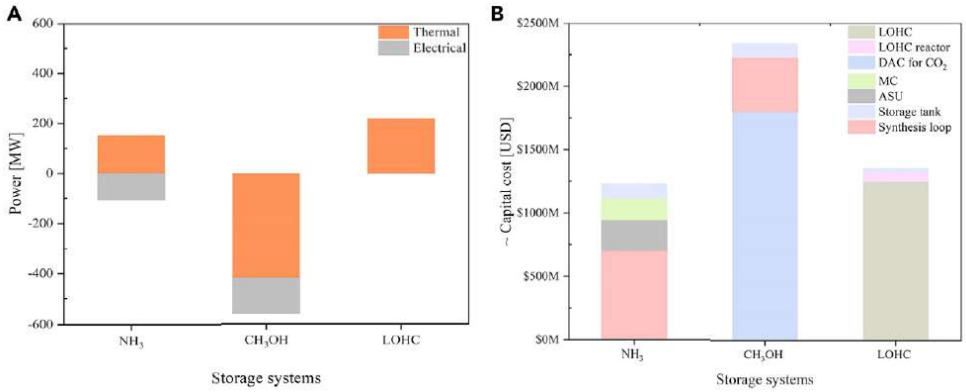

Figure 20. Estimation of power and capital cost for NH_3, CH_3OH, and LOHC hydrogenation plants [134].

3. Conclusions

The global shift from conventional fossil fuels to hydrogen as a clean energy alternative is gaining momentum, driven by growing environmental awareness and the imperative to reduce greenhouse gas emissions. However, the widespread adoption of hydrogen as a primary energy source faces significant challenges, particularly in the realm of storage and transportation infrastructure. Despite substantial research efforts directed towards developing viable storage solutions, such as porous carbon-based materials, metal-organic frameworks (MOFs), zeolites, and chemical hydrogen carriers, the scalability and efficiency of these options remain limited due to factors like low hydrogen capacity, high costs, and the lack of appropriate infrastructure.

As we strive to harness hydrogen's potential as a clean energy carrier, it becomes increasingly evident that technological innovation is essential to overcome these obstacles. Key considerations for hydrogen storage materials include their ability to maintain a liquid state during hydrogenation and dehydrogenation processes, operate at temperatures below 200 ℃ to minimize energy consumption, and ensure safety and environmental sustainability throughout their lifecycle. Chemical hydrogen carriers present a particularly promising avenue, offering lower energy losses, compatibility with existing infrastructure, and simpler handling compared to conventional storage methods. However, realizing their full potential hinges on advancing various technologies, including production, separation, catalyst development, and recovery, as well as refining dehydrogenation processes.

In essence, achieving a sustainable hydrogen economy requires a multifaceted approach that extends beyond mere technological advancements. It necessitates strategic collaborations between governments, industries, and research institutions to drive innovation, streamline regulatory frameworks, and invest in critical infrastructure. By continuously pushing the boundaries of scientific knowledge and engineering expertise, we can optimize catalysts and reaction systems, enabling the reversible, stable, and economically viable utilization of chemical hydrogen carriers for storage and transportation purposes. This holistic approach not only addresses the energy-intensive compression or liquefaction processes but also minimizes hydrogen loss, paving the way for a cleaner, greener future powered by hydrogen.

Funding: This research was funded by Korea Water Resources Corporation, grant

number G220691.

Conflict of interest: The authors declare no conflict of interest.

References

1. Bellosta von Colbe J, Ares JR, Barale J, et al. Application of hydrides in hydrogen storage and compression: Achievements, outlook and perspectives. International Journal of Hydrogen Energy. 2019; 44(15): 7780-7808. doi: 10.1016/j.ijhydene.2019.01.104
2. Bui M, Adjiman CS, Bardow A, et al. Carbon capture and storage (CCS): the way forward. Energy & Environmental Science. 2018; 11(5): 1062-1176. doi: 10.1039/c7ee02342a
3. Pérez-Fortes M, Schöneberger JC, Boulamanti A, et al. Methanol synthesis using captured CO_2 as raw material: Techno-economic and environmental assessment. Applied Energy. 2016; 161: 718-732. doi: 10.1016/j.apenergy.2015.07.067
4. Klankermayer J, Wesselbaum S, Beydoun K, et al. Selective Catalytic Synthesis Using the Combination of Carbon Dioxide and Hydrogen: Catalytic Chess at the Interface of Energy and Chemistry. Angewandte Chemie International Edition. 2016; 55(26): 7296-7343. doi: 10.1002/anie.201507458
5. Grinberg D, Elishav O, Bardow A, et al. Nitrogen-Based Fuels: A Power-to-Fuel-to-Power Analysis. Angewandte Chemie International Edition. 2016; 55(31): 8798-8805. doi: 10.1002/anie.201510618
6. Sang R, Wei Z, Hu Y, et al. Methyl formate as a hydrogen energy carrier. Nature Catalysis. 2023; 6(6): 543-550. doi: 10.1038/s41929-023-00959-8
7. Pfromm PH. Towards sustainable agriculture: Fossil-free ammonia. Journal of Renewable and Sustainable Energy. 2017; 9(3). doi: 10.1063/1.4985090
8. Philibert C. Producing ammonia and fertilizers: New opportunities from renewables. Available online: https://cdi.mecon.gob.ar/bases/docelec/az3521.pdf (accessed on 2 January 2024).
9. Hellman A, Honkala K, Dahl S, et al. Ammonia Synthesis: State of the Bellwether Reaction. In: Reedijk J, Poeppelmeier K (editors). Comprehensive Inorganic Chemistry II (Second Edition): From Elements to Applications. Elsevier; 2013. pp. 459-474. doi: 10.1016/b978-0-08-097774-4.00725-7
10. Tunå P, Hulteberg C, Ahlgren S. Techno-economic assessment of nonfossil ammonia production. Environmental Progress & Sustainable Energy. 2013; 33(4): 1290-1297. doi: 10.1002/ep.11886
11. Noelker K, Ruether J. Low energy consumption ammonia production: baseline energy consumption, Options for energy optimization. Available online: https://ucpcdn.thyssenkrupp.com/_legacy/UCPthyssenkruppBAIS/assets.files/download_1/ammonia_2/low_energy_consumption_ammonia_production_2011_paper.pdf (accessed on 2 January 2024).
12. Cheddie D. Ammonia as a Hydrogen Source for Fuel Cells: A Review. In: Minic D (editor). Hydrogen Energy - Challenges and Perspectives. IntechOpen; 2012. doi: 10.5772/47759
13. Mukherjee S, Devaguptapu SV, Sviripa A, et al. Low-temperature ammonia decomposition catalysts for hydrogen generation. Applied Catalysis B: Environmental. 2018; 226: 162-181. doi: 10.1016/j.apcatb.2017.12.039
14. Giddey S, Badwal SPS, Munnings C, et al. Ammonia as a Renewable Energy Transportation Media. ACS Sustainable Chemistry & Engineering. 2017; 5(11): 10231-10239. doi: 10.1021/acssuschemeng.7b02219
15. Thomas G, Parks G. Potential Roles of Ammonia in a Hydrogen Economy: A Study of Issues Related to the Use Ammonia for On-Board Vehicular Hydrogen Storage. US Department of Energy; 2006.
16. David WIF, Makepeace JW, Callear SK, et al. Hydrogen Production from Ammonia Using Sodium Amide. Journal of the American Chemical Society. 2014; 136(38): 13082-13085. doi: 10.1021/ja5042836
17. Makepeace JW, Hunter HMA, Wood TJ, et al. Ammonia decomposition catalysis using lithium–calcium imide. Faraday Discussions. 2016; 188: 525-544. doi: 10.1039/c5fd00179j
18. Gianotti E, Taillades-Jacquin M, Rozière J, et al. High-Purity Hydrogen Generation via Dehydrogenation of Organic Carriers: A Review on the Catalytic Process. ACS Catalysis. 2018; 8(5): 4660-4680. doi: 10.1021/acscatal.7b04278
19. Felderhoff M, Weidenthaler C, von Helmolt R, et al. Hydrogen storage: the remaining scientific and technological challenges. Physical Chemistry Chemical Physics. 2007; 9(21): 2643. doi: 10.1039/b701563c
20. Nielsen TK, Besenbacher F, Jensen TR. Nanoconfined hydrides for energy storage. Nanoscale. 2011; 3(5): 2086. doi: 10.1039/c0nr00725k

21. Rihko-Struckmann LK, Peschel A, Hanke-Rauschenbach R, et al. Assessment of Methanol Synthesis Utilizing Exhaust CO_2 for Chemical Storage of Electrical Energy. Industrial & Engineering Chemistry Research. 2010; 49(21): 11073-11078. doi: 10.1021/ie100508w
22. Dowson G, Styring P. Conversion of Carbon Dioxide to Oxygenated Organics. In: Styring P, Quadrelli EA, Armstrong K (editors). Carbon Dioxide Utilisation: Closing the Carbon Cycle. Elsevier; 2015. pp. 141-159. doi: 10.1016/b978-0-444-62746-9.00009-8
23. Pontzen F, Liebner W, Gronemann V, et al. CO_2-based methanol and DME – Efficient technologies for industrial scale production. Catalysis Today. 2011; 171(1): 242-250. doi: 10.1016/j.cattod.2011.04.049
24. Palo DR, Dagle RA, Holladay JD. Methanol Steam Reforming for Hydrogen Production. ChemInform. 2007; 38(51). doi: 10.1002/chin.200751266
25. Goeppert A, Czaun M, Jones JP, et al. Recycling of carbon dioxide to methanol and derived products – closing the loop. Chemical Society Reviews. 2014; 43(23): 7995-8048. doi: 10.1039/c4cs00122b
26. Kappis K, Papavasiliou J, Avgouropoulos G. Methanol Reforming Processes for Fuel Cell Applications. Energies. 2021; 14(24): 8442. doi: 10.3390/en14248442
27. Andersson J, Krüger A, Grönkvist S. Methanol as a carrier of hydrogen and carbon in fossil-free production of direct reduced iron. Energy Conversion and Management: X. 2020; 7: 100051. doi: 10.1016/j.ecmx.2020.100051
28. Chatterjee S, Parsapur RK, Huang KW. Limitations of Ammonia as a Hydrogen Energy Carrier for the Transportation Sector. ACS Energy Letters. 2021; 6(12): 4390-4394. doi: 10.1021/acsenergylett.1c02189
29. Bilgili F, Magazzino C. The nexus between the transportation sector and sustainable development goals: Theoretical and practical implications. Frontiers in Environmental Science. 2022; 10. doi: 10.3389/fenvs.2022.1055537
30. Zhai L, Liu S, Xiang Z. Ammonia as a carbon-free hydrogen carrier for fuel cells: a perspective. Industrial Chemistry & Materials. 2023; 1(3): 332-342. doi: 10.1039/d3im00036b
31. Ma Y, Guan G, Phanthong P, et al. Steam reforming of methanol for hydrogen production over nanostructured wire-like molybdenum carbide catalyst. International Journal of Hydrogen Energy. 2014; 39(33): 18803-18811. doi: 10.1016/j.ijhydene.2014.09.062
32. Hou K, Hughes R. The kinetics of methane steam reforming over a Ni/α-Al_2O catalyst. Chemical Engineering Journal. 2001; 82(1-3): 311-328. doi: 10.1016/S1385-8947(00)00367-3
33. Jones SD, Hagelin-Weaver HE. Steam reforming of methanol over CeO_2- and ZrO_2-promoted Cu-ZnO catalysts supported on nanoparticle Al_2O_3. Applied Catalysis B: Environmental. 2009; 90(1-2): 195-204. doi: 10.1016/j.apcatb.2009.03.013
34. Smith C, Torrente-Murciano L. Guidance for targeted development of ammonia synthesis catalysts from a holistic process approach. Chem Catalysis. 2021; 1(6): 1163-1172. doi: 10.1016/j.checat.2021.09.015
35. Chang B, Li L, Shi D, et al. Metal-free boron carbonitride with tunable boron Lewis acid sites for enhanced nitrogen electroreduction to ammonia. Applied Catalysis B: Environmental. 2021; 283: 119622. doi: 10.1016/j.apcatb.2020.119622
36. Xie T. Performance analysis of ammonia decomposition endothermic membrane reactor heated by trough solar collector. Energy Reports. 2922; 8: 526-538.
37. Lim DK, Plymill AB, Paik H, et al. Solid Acid Electrochemical Cell for the Production of Hydrogen from Ammonia. Joule. 2020; 4(11): 2338-2347. doi: 10.1016/j.joule.2020.10.006
38. García A, Marín P, Ordóñez S. Hydrogenation of liquid organic hydrogen carriers: Process scale-up, economic analysis and optimization. International Journal of Hydrogen Energy. 2024; 52: 1113-1123. doi: 10.1016/j.ijhydene.2023.06.273
39. Andersson J, Grönkvist S. Large-scale storage of hydrogen. International Journal of Hydrogen Energy. 2019; 44(23): 11901-11919. doi: 10.1016/j.ijhydene.2019.03.063
40. Soloveichik G. Metal borohydrides as hydrogen storage materials. Material Matters. 2007; 2(11).
41. Liu J, Sun L, Yang J, et al. Ti–Mn hydrogen storage alloys: from properties to applications. RSC Advances. 2022; 12(55): 35744-35755. doi: 10.1039/d2ra07301c
42. Sahlberg M, Karlsson D, Zlotea C, et al. Superior hydrogen storage in high entropy alloys. Scientific Reports. 2016; 6(1). doi: 10.1038/srep36770
43. Schneemann A, White JL, Kang S, et al. Nanostructured Metal Hydrides for Hydrogen Storage. Chemical Reviews. 2018; 118(22): 10775-10839. doi: 10.1021/acs.chemrev.8b00313
44. Larpruenrudee P, Bennett NS, Gu Y, et al. Design optimization of a magnesium-based metal hydride hydrogen energy storage system. Scientific Reports. 2022; 12(1). doi: 10.1038/s41598-022-17120-3

45. Tarasov B, Arbuzov A, Mozhzhukhin S, et al. Metal Hydride Hydrogen Storage (Compression) Units Operating at Near-Atmospheric Pressure of the Feed H_2. Inorganics. 2023; 11(7): 290. doi: 10.3390/inorganics11070290
46. Kondo R, T. Hiroyuki T. Magnesium-Based Materials for Hydrogen Storage: Microstructural Properties. In: Gupta M (editor). Magnesium - The Wonder Element for Engineering/Biomedical Applications. IntechOpen; 2020. doi: 10.5772/intechopen.88679
47. Rabkin E, Skripnyuk V, Estrin Y. Ultrafine-Grained Magnesium Alloys for Hydrogen Storage Obtained by Severe Plastic Deformation. Frontiers in Materials. 2019; 6. doi: 10.3389/fmats.2019.00240
48. Yin F, Chang Y, Si T, et al. Structural and kinetic adjustments of Zr-based high-entropy alloys with Laves phases by substitution of Mg element. Energy Advances. 2023; 2(9): 1409-1418. doi: 10.1039/d3ya00243h
49. Li Z, Liu S, Pu Y, et al. Single-crystal ZrCo nanoparticle for advanced hydrogen and H-isotope storage. Nature Communications. 2023; 14(1): 7966. doi: 10.1038/s41467-023-43828-5
50. Lee YJ, Ha J, Choi SJ, et al. Decreasing Hydrogen Content within Zirconium Using Au and Pd Nanoparticles as Sacrificial Agents under Pressurized Water at High Temperature. Materials. 2023; 16(18): 6164. doi: 10.3390/ma16186164
51. Kamble A, Sharma P, Huot J. Effect of the Addition of 4 wt% Zr to BCC Solid Solution $Ti_{52}V_{12}Cr_{36}$ at Melting/Milling on Hydrogen Sorption Properties. Frontiers in Materials. 2022; 8. doi: 10.3389/fmats.2021.821126
52. Song J, Wang J, Hu X, et al. Activation and Disproportionation of Zr_2Fe Alloy as Hydrogen Storage Material. Molecules. 2019; 24(8): 1542. doi: 10.3390/molecules24081542
53. Hu WK, Gao XP, Kiros Y, et al. Zr-Based AB_2-Type Hydrogen Storage Alloys as Dual Catalysts of Gas-Diffusion Electrodes in an Alkaline Fuel Cell. The Journal of Physical Chemistry B. 2004; 108(26): 8756-8758. doi: 10.1021/jp0486548
54. Liang L, Wang F, Rong M, et al. Recent Advances on Preparation Method of Ti-Based Hydrogen Storage Alloy. Journal of Materials Science and Chemical Engineering. 2020; 8(12): 18-38. doi: 10.4236/msce.2020.812003
55. Loh SM, Grant DM, Walker GS, et al. Substitutional effect of Ti-based AB2 hydrogen storage alloys: A density functional theory study. International Journal of Hydrogen Energy. 2023; 48(35): 13227-13235. doi: 10.1016/j.ijhydene.2022.12.083
56. Jangir M, Jain IP, Mirabile Gattia D. Effect of Ti-Based Additives on the Hydrogen Storage Properties of MgH_2: A Review. Hydrogen. 2023; 4(3): 523-541. doi: 10.3390/hydrogen4030034
57. Zhou C, Zhang J, Bowman RC, et al. Roles of Ti-Based Catalysts on Magnesium Hydride and Its Hydrogen Storage Properties. Inorganics. 2021; 9(5): 36. doi: 10.3390/inorganics9050036
58. Zholdayakova S, Gemma R, Uchida HH, et al. Mechanical Composition Control for Ti-Based Hydrogen Storage Alloys. e-Journal of Surface Science and Nanotechnology. 2018; 16(0): 298-301. doi: 10.1380/ejssnt.2018.298
59. Liu J, Xu J, Sleiman S, et al. Microstructure and hydrogen storage properties of Ti–V–Cr based BCC-type high entropy alloys. International Journal of Hydrogen Energy. 2021; 46(56): 28709-28718. doi: 10.1016/j.ijhydene.2021.06.137
60. Munekata Y, Washio K, Suda T, et al. Role of Annealing for Improving Hydrogen Storage Properties of Ti-Cr-V Alloy. MRS Proceedings. 2006; 971. doi: 10.1557/proc-0971-z07-21
61. Bellon Monsalve D, Ulate-Kolitsky E, Martínez-Amariz AD, et al. Effect of Zr_3Fe addition on hydrogen storage behaviour of Ti_2CrV alloys. Heliyon. 2023; 9(12): e22537. doi: 10.1016/j.heliyon.2023.e22537
62. Bouzidi A, Laversenne L, Nassif V, et al. Hydrogen Storage Properties of a New Ti-V-Cr-Zr-Nb High Entropy Alloy. Hydrogen. 2022; 3(2): 270-284. doi: 10.3390/hydrogen3020016
63. Yu X, Wu Z, Xia B, et al. Hydrogen storage in Ti–V-based body-centered-cubic phase alloys. Journal of Materials Research. 2003; 18(11): 2533-2536. doi: 10.1557/jmr.2003.0352
64. Mohammed Abdul J, Hearth Chown L, Kolawole Odusote J, et al. Hydrogen Storage Characteristics and Corrosion Behavior of $Ti_{24}V_{40}Cr_{34}Fe_2$ Alloy. Batteries. 2017; 3(4): 19. doi: 10.3390/batteries3020019
65. Li B, He L, Li J, et al. Ti-V-C-Based Alloy with a FCC Lattice Structure for Hydrogen Storage. Molecules. 2019; 24(3): 552. doi: 10.3390/molecules24030552
66. Yadav TP, Kumar A, Verma SK, et al. High-Entropy Alloys for Solid Hydrogen Storage: Potentials and Prospects. Transactions of the Indian National Academy of Engineering. 2022; 7(1): 147-156. doi: 10.1007/s41403-021-00316-w
67. Orłowski PA, Grochala W. Effect of Vanadium Catalysts on Hydrogen Evolution from $NaBH_4$. Solids. 2022; 3(2): 295-310. doi: 10.3390/solids3020021
68. Niaz S, Manzoor T, Pandith AH. Hydrogen storage: Materials, methods and perspectives. Renewable and Sustainable Energy Reviews. 2015; 50: 457-469. doi: 10.1016/j.rser.2015.05.011

69. Yadav M, Xu Q. Liquid-phase chemical hydrogen storage materials. Energy & Environmental Science. 2012; 5(12): 9698. doi: 10.1039/c2ee22937d
70. Kaur M, Pal K. Review on hydrogen storage materials and methods from an electrochemical viewpoint. Journal of Energy Storage. 2019; 23: 234-249. doi: 10.1016/j.est.2019.03.020
71. Ren J, Musyoka NM, Langmi HW, et al. Current research trends and perspectives on materials-based hydrogen storage solutions: A critical review. International Journal of Hydrogen Energy. 2017; 42(1): 289-311. doi: 10.1016/j.ijhydene.2016.11.195
72. Kumar S, Jain A, Ichikawa T, et al. Development of vanadium based hydrogen storage material: A review. Renewable and Sustainable Energy Reviews. 2017; 72: 791-800. doi: 10.1016/j.rser.2017.01.063
73. Marques F, Balcerzak M, Winkelmann F, et al. Review and outlook on high-entropy alloys for hydrogen storage. Energy & Environmental Science. 2021; 14(10): 5191-5227. doi: 10.1039/d1ee01543e
74. Rolo I, Costa VAF, Brito FP. Hydrogen-Based Energy Systems: Current Technology Development Status, Opportunities and Challenges. Energies. 2023; 17(1): 180. doi: 10.3390/en17010180
75. Badea IC, Șerban BA, Anasiei I, et al. The Energy Storage Technology Revolution to Achieve Climate Neutrality. Energies. 2023; 17(1): 140. doi: 10.3390/en17010140
76. Grigorova E, Markov P, Tsyntsarski B, et al. Hydrogen Storage Properties of Ball Milled MgH_2 with Additives- Ni, V and Activated Carbons Obtained from Different By-Products. Materials. 2023; 16(20): 6823. doi: 10.3390/ma16206823
77. Ahad M, Bhuiyan M, Sakib A, et al. An Overview of Challenges for the Future of Hydrogen. Materials. 2023; 16(20): 6680. doi: 10.3390/ma16206680
78. Habib AKMA, Sakib AN, Mona ZT, et al. Hydrogen-Assisted Aging Applied to Storage and Sealing Materials: A Comprehensive Review. Materials. 2023; 16(20): 6689. doi: 10.3390/ma16206689
79. Román-Sedano AM, Campillo B, Villalobos JC, et al. Hydrogen Diffusion in Nickel Superalloys: Electrochemical Permeation Study and Computational AI Predictive Modeling. Materials. 2023; 16(20): 6622. doi: 10.3390/ma16206622
80. Paskevicius M, Jepsen LH, Schouwink P, et al. Metal borohydrides and derivatives – synthesis, structure and properties. Chemical Society Reviews. 2017; 46(5): 1565-1634. doi: 10.1039/c6cs00705h
81. Schorn F, Breuer JL, Samsun RC, et al. Methanol as a renewable energy carrier: An assessment of production and transportation costs for selected global locations. Advances in Applied Energy. 2021; 3: 100050. doi: 10.1016/j.adapen.2021.100050
82. Baxter J, Bian Z, Chen G, et al. Nanoscale design to enable the revolution in renewable energy. Energy & Environmental Science. 2009; 2(6): 559. doi: 10.1039/b821698c
83. Gondal IA. Offshore renewable energy resources and their potential in a green hydrogen supply chain through power-to-gas. Sustainable Energy & Fuels. 2019; 3(6): 1468-1489. doi: 10.1039/c8se00544c
84. Sartbaeva A, Kuznetsov VL, Wells SA, et al. Hydrogen nexus in a sustainable energy future. Energy & Environmental Science. 2008; 1(1): 79. doi: 10.1039/b810104n
85. Mazloomi K, Gomes C. Hydrogen as an energy carrier: Prospects and challenges. Renewable and Sustainable Energy Reviews. 2012; 16(5): 3024-3033. doi: 10.1016/j.rser.2012.02.028
86. Züttel A, Remhof A, Borgschulte A, et al. Hydrogen: the future energy carrier. Philosophical Transactions of the Royal Society A: Mathematical, Physical and Engineering Sciences. 2010; 368(1923): 3329-3342. doi: 10.1098/rsta.2010.0113
87. Eppinger J, Huang K. Formic acid as a hydrogen energy carrier. ACS Energy Letters. 2017; 2(1): 188-195. doi: 10.1021/acsenergylett.6b00574
88. Lai Q, Sun Y, Wang T, et al. How to Design Hydrogen Storage Materials? Fundamentals, Synthesis, and Storage Tanks. Advanced Sustainable Systems. 2019; 3(9). doi: 10.1002/adsu.201900043
89. Behrens M, Marc A. Methanol steam reforming. In: Guczi L, Erdôhelyi A (editors). Catalysis for Alternative Energy Generation. Springer; 2012. pp. 175-235. doi:10.1007/978-1-4614-0344-9_5
90. Özcan O, Ayşe N. Thermodynamic analysis of methanol steam reforming to produce hydrogen for HT-PEMFC: an optimization study. International Journal of Hydrogen Energy. 2019; 44(27): 14117-14126. doi: 10.1016/j.ijhydene.2018.12.211
91. Richards N, Needels J, Erickson P. Autothermal-reformation enhancement using a stratified-catalyst technique. International Journal of Hydrogen Energy. 2017; 42(41): 25914-25923. doi: 10.1016/j.ijhydene.2017.08.050
92. Ahmed AA, Al Labadidi M, Hamada AT, et al. Design and Utilization of a Direct Methanol Fuel Cell. Membranes. 2022;

12(12): 1266. doi: 10.3390/membranes12121266
93. Cheng Z, Zhou W, Lan G, et al. High-performance Cu/ZnO/Al_2O_3 catalysts for methanol steam reforming with enhanced Cu-ZnO synergy effect via magnesium assisted strategy. Journal of Energy Chemistry. 2021; 63: 550-557. doi: 10.1016/j.jechem.2021.08.025
94. Jin Q, Meng X, Wu P, et al. Methanol steam reforming for hydrogen production over $NiTiO_3$ nanocatalyst with hierarchical porous structure. RSC Advances. 2023; 13(24): 16342-16351. doi: 10.1039/d3ra02891g
95. Lawes N, Gow IE, Smith LR, et al. Methanol synthesis from CO_2 and H_2 using supported Pd alloy catalysts. Faraday Discussions. 2023; 242: 193-211. doi: 10.1039/d2fd00119e
96. Mansor M, Timmiati SN, Wong WY, et al. NiPd Supported on Mesostructured Silica Nanoparticle as Efficient Anode Electrocatalyst for Methanol Electrooxidation in Alkaline Media. Catalysts. 2020; 10(11): 1235. doi: 10.3390/catal10111235
97. Kang Y, Wang W, Pu Y, et al. An effective Pd-NiO_x-P composite catalyst for glycerol electrooxidation: Co-existed phosphorus and nickel oxide to enhance performance of Pd. Chemical Engineering Journal. 2017; 308: 419-427. doi: 10.1016/j.cej.2016.09.087
98. De Rogatis L, Montini T, Cognigni A, et al. Methane partial oxidation on NiCu-based catalysts. Catalysis Today. 2009; 145(1-2): 176-185. doi: 10.1016/j.cattod.2008.04.019
99. Lu J, Li X, He S, et al. Hydrogen production via methanol steam reforming over Ni-based catalysts: Influences of Lanthanum (La) addition and supports. International Journal of Hydrogen Energy. 2017; 42(6): 3647-3657. doi: 10.1016/j.ijhydene.2016.08.165
100. Pérez-Hernández R, Avendaño AD, Rubio E, et al. Hydrogen Production by Methanol Steam Reforming Over Pd/ZrO_2–TiO_2 Catalysts. Topics in Catalysis. 2011; 54(8-9): 572-578. doi: 10.1007/s11244-011-9622-0
101. Abraham BG, Bhaskaran R, Chetty R. Electrodeposited Bimetallic (PtPd, PtRu, PtSn) Catalysts on Titanium Support for Methanol Oxidation in Direct Methanol Fuel Cells. Journal of The Electrochemical Society. 2020; 167(2): 024512. doi: 10.1149/1945-7111/ab6a7d
102. Tahay P, Khani Y, Jabari M, et al. Highly porous monolith/TiO_2 supported Cu, Cu-Ni, Ru, and Pt catalysts in methanol steam reforming process for H_2 generation. Applied Catalysis A: General. 2018; 554: 44-53. doi: 10.1016/j.apcata.2018.01.022
103. Wang T, Zhao Y, Setzler BP, et al. A high-performance 75 W direct ammonia fuel cell stack. Cell Reports Physical Science. 2022; 3(4): 100829. doi: 10.1016/j.xcrp.2022.100829
104. Pawelczyk E, Łukasik N, Wysocka I, et al. Recent Progress on Hydrogen Storage and Production Using Chemical Hydrogen Carriers. Energies. 2022; 15(14): 4964. doi: 10.3390/en15144964
105. Oh S, Oh MJ, Hong J, et al. A comprehensive investigation of direct ammonia-fueled thin-film solid-oxide fuel cells: Performance, limitation, and prospects. iScience. 2022; 25(9): 105009. doi: 10.1016/j.isci.2022.105009
106. Hasan MH, Mahlia TMI, Mofijur M, et al. A Comprehensive Review on the Recent Development of Ammonia as a Renewable Energy Carrier. Energies. 2021; 14(13): 3732. doi: 10.3390/en14133732
107. Klerke A, Christensen CH, Nørskov JK, et al. Ammonia for hydrogen storage: challenges and opportunities. Journal of Materials Chemistry. 2008; 18(20): 2304. doi: 10.1039/b720020j
108. Lu H, Fengshou Y, Raveendran S. Carbon-Based Catalysts for Selective Electrochemical Nitrogen-to-Ammonia Conversion. ACS Sustainable Chemistry & Engineering. 2021, 9(23): 7687-7703. Doi: doi.org/10.1021/acssuschemeng.1c00575
109. Jang JH, Park SY, Youn DH, et al. Recent Advances in Electrocatalysts for Ammonia Oxidation Reaction. Catalysts. 2023; 13(5): 803. doi: 10.3390/catal13050803
110. Morlanés N, Almaksoud W, Rai RK, et al. Development of catalysts for ammonia synthesis based on metal phthalocyanine materials. Catalysis Science & Technology. 2020; 10(3): 844-852. doi: 10.1039/c9cy02326g
111. Javaid R, Nanba T. Stability of Cs/Ru/MgO Catalyst for Ammonia Synthesis as a Hydrogen and Energy Carrier. Energies. 2022; 15(10): 3506. doi: 10.3390/en15103506
112. Fedorova ZA, Borisov VA, Pakharukova VP, et al. Layered Double Hydroxide-Derived Ni-Mg-Al Catalysts for Ammonia Decomposition Process: Synthesis and Characterization. Catalysts. 2023; 13(4): 678. doi: 10.3390/catal13040678
113. Cha J, Park Y, Brigljević B, et al. An efficient process for sustainable and scalable hydrogen production from green ammonia. Renewable and Sustainable Energy Reviews. 2021; 152: 111562. doi: 10.1016/j.rser.2021.111562
114. Anaya-Castro F de J, Beltrán-Gastélum M, Morales Soto O, et al. Ultra-Low Pt Loading in PtCo Catalysts for the Hydrogen Oxidation Reaction: What Role Do Co Nanoparticles Play? Nanomaterials. 2021; 11(11): 3156. doi: 10.3390/nano11113156

115. Li ZF, Wang Y, Botte GG. Revisiting the electrochemical oxidation of ammonia on carbon-supported metal nanoparticle catalysts. Electrochimica Acta. 2017; 228: 351-360. doi: 10.1016/j.electacta.2017.01.020
116. Kang Y, Wang W, Li J, et al. A Highly Efficient Pt-NiO/C Electrocatalyst for Ammonia Electro-Oxidation. Journal of The Electrochemical Society. 2017; 164(9): F958-F965. doi: 10.1149/2.1051709jes
117. Li J, Wang W, Chen W, et al. Sub-nm ruthenium cluster as an efficient and robust catalyst for decomposition and synthesis of ammonia: Break the "size shackles." Nano Research. 2018; 11(9): 4774-4785. doi: 10.1007/s12274-018-2062-4
118. Zhang H, Alhamed YA, Al-Zahrani A, et al. Tuning catalytic performances of cobalt catalysts for clean hydrogen generation via variation of the type of carbon support and catalyst post-treatment temperature. International Journal of Hydrogen Energy. 2014; 39(31): 17573-17582. doi: 10.1016/j.ijhydene.2014.07.183
119. Nagaoka K, Eboshi T, Abe N, et al. Influence of basic dopants on the activity of Ru/Pr_6O_{11} for hydrogen production by ammonia decomposition. International Journal of Hydrogen Energy. 2014; 39(35): 20731-20735. doi: 10.1016/j.ijhydene.2014.07.142
120. Li G, Nagasawa H, Kanezashi M, et al. Graphene nanosheets supporting Ru nanoparticles with controlled nanoarchitectures form a high-performance catalyst for CO_x-free hydrogen production from ammonia. Journal of Materials Chemistry A. 2014; 2(24): 9185-9192. doi: 10.1039/c4ta01193g
121. Duan X, Qian G, Zhou X, et al. Tuning the size and shape of Fe nanoparticles on carbon nanofibers for catalytic ammonia decomposition. Applied Catalysis B: Environmental. 2011; 101(3-4): 189-196. doi: 10.1016/j.apcatb.2010.09.017
122. Zhang J, Müller JO, Zheng W, et al. Individual Fe−Co Alloy Nanoparticles on Carbon Nanotubes: Structural and Catalytic Properties. Nano Letters. 2008; 8(9): 2738-2743. doi: 10.1021/nl8011984
123. Yin SF, Zhang QH, Xu BQ, et al. Investigation on the catalysis of CO_x-free hydrogen generation from ammonia. Journal of Catalysis. 2004; 224(2): 384-396. doi: 10.1016/j.jcat.2004.03.008
124. Eblagon KM, Rentsch D, Friedrichs O, et al. Hydrogenation of 9-ethylcarbazole as a prototype of a liquid hydrogen carrier. International Journal of Hydrogen Energy. 2010; 35(20): 11609-11621. doi: 10.1016/j.ijhydene.2010.03.068
125. Bourane A, Elanany M, Pham TV, et al. An overview of organic liquid phase hydrogen carriers. International Journal of Hydrogen Energy. 2016; 41(48): 23075-23091. doi: 10.1016/j.ijhydene.2016.07.167
126. Pujadó P, Moser M. Catalytic reforming: Handbook of petroleum processing. Dordrecht. Springer Netherlands; 2006. pp. 217-237. doi: 10.1007/1-4020-2820-2_5
127. Crabtree RH. Nitrogen-Containing Liquid Organic Hydrogen Carriers: Progress and Prospects. ACS Sustainable Chemistry & Engineering. 2017; 5(6): 4491-4498. doi: 10.1021/acssuschemeng.7b00983
128. Brückner N, Obesser K, Bösmann A, et al. Evaluation of Industrially Applied Heat-Transfer Fluids as Liquid Organic Hydrogen Carrier Systems. ChemSusChem. 2013; 7(1): 229-235. doi: 10.1002/cssc.201300426
129. Preuster P, Papp C, Wasserscheid P. Liquid Organic Hydrogen Carriers (LOHCs): Toward a Hydrogen-free Hydrogen Economy. Accounts of Chemical Research. 2016; 50(1): 74-85. doi: 10.1021/acs.accounts.6b00474
130. Rüde T, Bösmann A, Preuster P, et al. Resilience of Liquid Organic Hydrogen Carrier Based Energy-Storage Systems. Energy Technology. 2017; 6(3): 529-539. doi: 10.1002/ente.201700446
131. Acharya D, Ng D, Xie Z. Recent Advances in Catalysts and Membranes for MCH Dehydrogenation: A Mini Review. Membranes. 2021; 11(12): 955. doi: 10.3390/membranes11120955
132. Le TH, Tran N, Lee HJ. Development of Liquid Organic Hydrogen Carriers for Hydrogen Storage and Transport. International Journal of Molecular Sciences. 2024; 25(2): 1359. doi: 10.3390/ijms25021359
133. Schuster R, Bertram M, Runge H, et al. Metastability of palladium carbide nanoparticles during hydrogen release from liquid organic hydrogen carriers. Physical Chemistry Chemical Physics. 2021; 23(2): 1371-1380. doi: 10.1039/d0cp05606e
134. Abdin Z, Tang C, Liu Y, et al. Large-scale stationary hydrogen storage via liquid organic hydrogen carriers. iScience. 2021; 24(9): 102966. doi: 10.1016/j.isci.2021.102966
135. Sun F, An Y, Lei L, et al. Identification of the starting reaction position in the hydrogenation of (N-ethyl)carbazole over Raney-Ni. Journal of Energy Chemistry. 2015; 24(2): 219-224. doi: 10.1016/S2095-4956(15)60304-7
136. Rao P, Yoon M. Potential Liquid-Organic Hydrogen Carrier (LOHC) Systems: A Review on Recent Progress. Energies. 2020; 13(22): 6040. doi: 10.3390/en13226040
137. Chen X, Gierlich CH, Schötz S, et al. Hydrogen Production Based on Liquid Organic Hydrogen Carriers through Sulfur Doped Platinum Catalysts Supported on TiO_2. ACS Sustainable Chemistry & Engineering. 2021; 9(19): 6561-6573. doi: 10.1021/acssuschemeng.0c09048

138. Niermann M, Beckendorff A, Kaltschmitt M, et al. Liquid Organic Hydrogen Carrier (LOHC) – Assessment based on chemical and economic properties. International Journal of Hydrogen Energy. 2019; 44(13): 6631-6654. doi: 10.1016/j.ijhydene.2019.01.199
139. Niermann M, Drünert S, Kaltschmitt M, et al. Liquid organic hydrogen carriers (LOHCs) – techno-economic analysis of LOHCs in a defined process chain. Energy & Environmental Science. 2019; 12(1): 290-307. doi: 10.1039/c8ee02700e
140. Tang C, Feng Z, Bai X. In situ preparation of Pd nanoparticles on N-doped graphitized carbon derived from ZIF-67 by nitrogen glow-discharge plasma for the catalytic dehydrogenation of dodecahydro-N-ethylcarbazole. Fuel. 2021; 302: 121186. doi: 10.1016/j.fuel.2021.121186
141. Yang J, Fan Y, Li ZL, et al. Bimetallic Pd-M (M = Pt, Ni, Cu, Co) nanoparticles catalysts with strong electrostatic metal-support interaction for hydrogenation of toluene and benzene. Molecular Catalysis. 2020; 492: 110992. doi: 10.1016/j.mcat.2020.110992
142. Yang Y, Lin X, Tang J, et al. Supported mesoporous Pt catalysts with excellent performance for toluene hydrogenation under low reaction pressure. Molecular Catalysis. 2022; 524: 112341. doi: 10.1016/j.mcat.2022.112341
143. Zhu L, Shan S, Petkov V, et al. Ruthenium–nickel–nickel hydroxide nanoparticles for room temperature catalytic hydrogenation. Journal of Materials Chemistry A. 2017; 5(17): 7869-7875. doi: 10.1039/c7ta01437f
144. Zhang M, Song Q, He Z, et al. Tuning the mesopore-acid-metal balance in Pd/HY for efficient deep hydrogenation saturation of naphthalene. International Journal of Hydrogen Energy. 2022; 47(48): 20881-20893. doi: 10.1016/j.ijhydene.2022.04.191
145. Ding Y, Dong Y, Zhang H, et al. A highly adaptable Ni catalyst for Liquid Organic Hydrogen Carriers hydrogenation. International Journal of Hydrogen Energy. 2021; 46(53): 27026-27036. doi: 10.1016/j.ijhydene.2021.05.196
146. Jorschick H, Preuster P, Dürr S, et al. Hydrogen storage using a hot pressure swing reactor. Energy & Environmental Science. 2017; 10(7): 1652-1659. doi: 10.1039/c7ee00476a

Academic Publishing Pte. Ltd.

Add: 73 Upper Paya Lebar Road #07-02B-01 Centro Bianco Singapore 534818

Tel: +65 83184869

E-mail: editorial_office@acad-pub.com

Web: http://ojs.acad-pub.com/